Proton conduction via large-scale atomistic simulations

Freie Universität Berlin

Christoph Wehmeyer

Berlin 2013

Erstgutachter/Betreuer

Prof. Dr. Daniel Sebastiani
MLU Halle-Wittenberg
Institut für Physikalische Chemie
Von-Dankelmann-Platz 4
D-06120 Halle (Saale)

Zweitgutachter

Prof. Dr. Piet Brouwer
FU Berlin
Institut für Theoretische Physik
Arnimallee 14
D-14195 Berlin

Tag der Disputation: 30.08.2013

Die hier vorgestellten Arbeiten wurden in der Arbeitsgruppe von Daniel Sebastiani am *Institut für Theoretische Physik* an der Freien Universität Berlin angefertigt.

Hiermit versichere ich, die vorliegende Arbeit selbst und ohne weitere Hilfsmittel, außer den angegebenen, angefertigt zu haben.

Berlin, den _____

Table of contents

1 Introduction

Chemical physics is an interdisciplinary field in which physicists study chemical systems and reactions, i.e, atoms, molecules, and their interactions. Like in other disciplines of physics, theory and experiment are closely linked: theoretical physicists derive mathematical models to explain experimentally observed phenomena and to predict new properties and mechanisms; vice versa, experimentalists use theoretical models to interpret their results and inspire further experiments to put these models to the test. But even though this cooperation between theory and experminent is very successful for small chemical systems, e.g., the theoretical modeling of pair-wise interactions and spectroscopy experiments with atomistic resolution, the situation is more complicated for realistic systems which come easily in the order of 10^2–10^6 atoms. From the theoretical point of view, the understanding of pair-wise interactions does not automatically enable the prediction of interaction phenomena of many-body systems, and even deceptively simple molecular assemblies like two water molecules are already too complex for an analytical treatment. Experimentalists, on the other hand, often measure phenomenological effects and statistical averages instead of the atomistic picture; hence, the actually studied mechanisms are not directly observable and theoretical models are needed to interpret the results.

At this point, computational methods can act as a bridge between theory and experiment. In particular, many chemical systems that are too large and too complicated for analytical treatment can still be simulated on the basis of the theoretical model of the pair-wise interactions; thus, theoretical predictions for experimentally accessible observables can be computed in numerical experiments on the computer. The theoretical level of the modeling itself ranges from point particles with semiempirical force laws to an atomistic picture with a quantum mechanical description of the electronic structure. This ansatz has the additional feature of a high resolution (depending on the theoretical level of the modeling) and the studied mechanisms can actually be visualized.

The computational ansatz in chemical physics, however, replaces one problem with another: even though it is now possible to compute theorectical predictions for large and complex chemical systems, the appropriate simulation of such systems is, not surpringsingly, quite difficult for various reasons. While simple interaction models are easy to implement and computationally cheap, they in general have very limited applicability and predicitive quality. Chemically realistic processes, e.g., reactions with breaking and forming of covalent bonds, require a sophisticated approach on the basis of quantum mechanics, which usually comes with a high computational cost; and even then, various approximations are necessary in the derivation of the modeling. Thus, the accurate simulation of realistic chemical processes is still far from being a routine problem, despite decades of development of algorithms and computational infrastucture.

A case in point is the simulation of proton conduction processes in fuel cell membranes which is the main topic of the present thesis. Such membrane materials are usually large-scale systems with a great deal of disorder, and the calculation of statistically converged observables also requires large time scales. The proton transfer events, i.e., the breaking and formation of covalent bonds, are central to any proton conduction mechanism and require a high level of theory in the modeling of the interatomic interaction.

However, such large-scale simulations also require large-scale methods whose development constitute a more theoretical part of my thesis.

In the scope of my work, which I present here in cumulative* form, I addressed in particular the following issues: the connection between structural properties and spectroscopic parameters in hydrogen bonded networks (Section 3.1); the development of a method to increase the accuracy of hybrid quantum-classical calculations which increases the applicability of spectroscopic calculations for large scale systems (Section 3.2); the development of a swarm intelligence-based stochastic scheme for the optimization of the geometry of atomic/molecular clusters (Section 3.3); and application of computational electronic structure methods to unravel the proton conduction mechanism in the dense hydrogen bond network in a promising fuel cell membrane material (Section 3.4).

This thesis is organized as follows: in Section 2, I will continue the introduction to my work by describing the fundamental framework of computational chemical physics, and I will sketch the applied methods. Section 3 introduces the individual projects that I addressed in my work and proceeds with a review of the acquired results. Finally, I conclude my findings in Section 4 of this document.

---

*The involved articles are listed in full in Appendix B.

2 Theoretical framework

2.1 Computational chemical physics

The computational approach in chemical physics aims at the simulation of chemical systems, processes, and reactions on the computer, i.e., performing numerical experiments based on theoretical models. Thus, it acts as a conceptual bridge between theory and experiment where an exact analytical treatment of the studied system is not possible anymore. Note that, in chemical physics, this is already the case for systems as simple as a single water (or even a hydrogen) molecule.

In this chapter, I will outline the basic framework of computational chemical physics. I will describe how we can

- represent atoms/molecules on the computer (Section 2.2),

- model the interactions between atoms and molecules (Sections 2.3 and 2.4), and

- simulate dynamical processes based on the model of the atomic/molecular interaction (Section 2.5).

2.2 An atomic/molecular representation on the computer

To adequately model a chemical system on the computer, we need a representation that includes all relevant degrees of freedom. In general, this means that an atom is represented as a point particle at the spatial position $\mathbf{r}$ and, likewise, a set of N atoms is represented by a set of their spatial vectors $\{\mathbf{r}_1, \ldots, \mathbf{r}_N\}$. Note that, in some cases, the atom representation can carry additional properties, e.g., an electric charge or a spin. In other cases, a large structure of atoms can be approximated as a single object, e.g., as a sphere or an ellipsoid.

For now, we assume that an atom or a molecule is given by its position $\mathbf{r}$ and that they are subject to an interaction potential V that depends on their relative positions. Thus, the spatial arrangement of N atoms/molecules can be characterized via a potential energy expression

$$E_{\text{pot}} = V(\mathbf{r}_1, \ldots, \mathbf{r}_N). \tag{1}$$

With this, we can compute forces between the individual atoms/molecules via the derivative of the potential energy with respect to the specific atom/molecule:

$$\mathbf{F}_i = -\frac{\partial}{\partial \mathbf{r}_i} V(\mathbf{r}_1, \ldots, \mathbf{r}_N). \tag{2}$$

Quite often, the interaction is given by a pair potential; in this case, the potential energy of a system of N atoms/molecules is simply the sum of all pairs:

$$V(\mathbf{r}_1, \ldots, \mathbf{r}_N) = \sum_{i=1}^{N-1} \sum_{j=i+1}^{N} V_{\text{pair}}(\mathbf{r}_i, \mathbf{r}_j). \tag{3}$$

11

Likewise, there also are potentials with a three-body-term. This is the case when the potential depends not only on the distances between the particles, but also on their spatial arrangment, e.g., in many crystalline materials.

2.3 Modeling inter- and intramolecular interactions

2.3.1 Early semiempiric expressions

In contemporary physics, we understand that the nature of all inter- and intramolecular interaction is essentially electrostatic, or, as the theorem[1] of Hellman and Feynman states: the forces between atoms/molecules can be computed from the electronic ground state density $n(\mathbf{r})$ on the basis of classical electrostatics. But before the development of quantum mechanics, scholars described the various types of experimantally observed interaction phenomena with semiempirical expressions. A case in point is the state equation of van der Waals (1873),

$$\left(P + \frac{a}{V^2}\right)(V - b) = RT,$$

(4)

that describes the behavior of gases and liquids, or the interaction potential proposed by Mie (1903),

$$V(r) = -\frac{A}{r^n} + \frac{B}{r^m},$$

(5)

which, for the first time, combined attraction and repulsion in a single interaction expression.[2] A special case of Mie's potential* is known as the Lennard-Jones potential[3] (see Figure 1):

$$V(r) = 4\epsilon\left(\frac{\sigma^{12}}{r^{12}} - \frac{\sigma^6}{r^6}\right).$$

(6)

The parameters ϵ and σ are the depth of the potential well and the zero-crossing of the potential. The Lennard-Jones (LJ) potential is, despite its simple expression, a good approximation for the interaction of unpolar atoms and molecules, and it finds further application in more elaborated interaction models to account for dispersion forces.

For the description of intramolecular interactions, in particular for diatomic molecules, Morse (1929) proposed the following potential:

$$V(r) = D_r e^{\varphi(1 - r/r_{\mathrm{eq}})}\left(e^{\varphi(1 - r/r_{\mathrm{eq}})} - 2\right),$$

(7)

with potential well depth D_r, atomic equilibrium distance r_{eq}, and a dimensionless range parameter φ, which relates to the width of the potential well. Note that the Morse potential (see Figure 1) has the interesting feature that it allows for the anaylytical solution of the Schrödinger equation. It also leads to a better description of vibrational states than the quantum mechanical harmonic oscillator.[4]

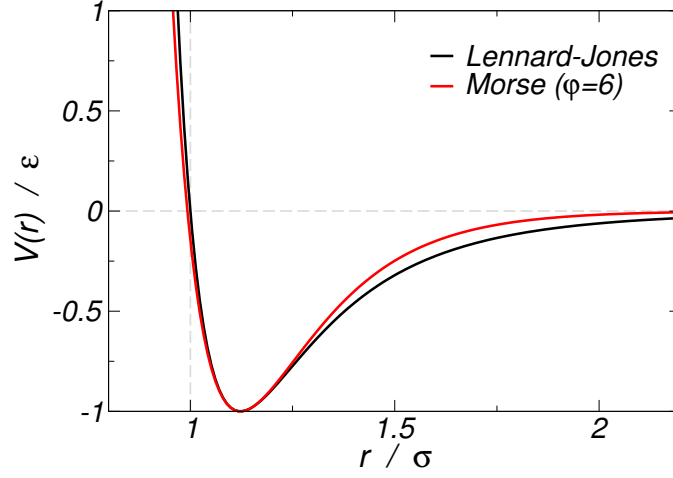*with the choice $n = 6$ and $m = 12$

Figure 1: Examples of semiempiric distance-based pair potentials: the Lennard-Jones potential (black) and the Morse potential (red, with $D_r = \epsilon$, $r_{\text{eq}} = \sqrt[6]{2}\sigma$, and $\varphi = 6$).

2.3.2 Classical force fields

The modeling of more realistic systems, like water molecules, also requires more complicated models for the interaction that account for internal structure and polarization. A case in point is the TIPnP potential.[5–7] This model treats a water molecule as a collection of $n = 3$, 4, or 5 point charges with a rigid geometry. This intermolecular interaction potential is defined as a mixture of Coulomb and van der Waals type; in particular, the potential energy of two water molecules A and B is given by

$$V_{\text{inter}}(A, B) = \frac{1}{4\pi\epsilon_0} \sum_{i}^{\text{on A}} \sum_{j}^{\text{on B}} \frac{q_i q_j}{r_{ij}} + 4\epsilon \left(\frac{\sigma^{12}}{r_{OO}^{12}} - \frac{\sigma^6}{r_{OO}^6} \right), \tag{8}$$

where q_i and q_j are point charges at distances r_{ij} (Coulomb interaction) and r_{OO} is the separation of the oxygen atoms (van der Waals interaction).

The next step towards an even more realistic model is to include, besides the internal structure, also internal degrees of freedom, i.e., a variable molecular geometry; therefore, the interaction potential needs additional (intramolecular) terms for the "self-energy" of the molecules. A prominent example for this is, again for the case of water, the flexible TIP4P potential:[8]

$$V(A, B) = V_{\text{inter}}(A, B) + V_{\text{intra}}(A) + V_{\text{intra}}(B). \tag{9}$$

The intermolecular potential is given by Equation (8); the intramolecular potential uses a quartic expansion of the Morse potential to account for the O–H bond stretching (r_{OH}) and a harmonic potential for the H–O–H angle (θ_{HOH}):

$$V_{\text{intra}}\left(r_{\text{OH}}^{(1)}, r_{\text{OH}}^{(2)}, \theta_{\text{HOH}}\right) = V_{\text{OH}}\left(r_{\text{OH}}^{(1)}\right) + V_{\text{OH}}\left(r_{\text{OH}}^{(2)}\right) + \left(\theta_{\text{HOH}} - \theta_{\text{eq}}\right)^2 \tag{10}$$

$$V_{\text{OH}}(r) = D_r\left(\alpha_r^2\left(r - r_{\text{eq}}\right)^2 - \alpha_r^3\left(r - r_{\text{eq}}\right)^3 + \frac{7}{12}\alpha_r^4\left(r - r_{\text{eq}}\right)^4\right), \tag{11}$$

where r_{eq} and θ_{eq} are the equilibrium O–H bond length and H–O–H angle.

The interaction potentials described by the Equations (5)–(11) are generally referred to as "force fields"[*] and, over the years, many scholars have proposed similar expressions for more complex molecular structures than water. Some widely used examples of such force fields are CHARMM[9,10] (1983), OPLS[11] (1988), and AMBER[12,13] (1995); each one has its merits for specific systems (the molecular setup) and physical properties (e.g., vibrational modes). In practice, it depends on the experience of the researcher to chose the appropriate force field for a specific simulation. Note that, in general, a force field not only defines a mathematical expression for the inter- and intramolecular interaction, but also provides a catalogue of numerical parameters for different types of molecules; this includes point charges, bond stretching, angles, dihedrals, and van der Waals interactions.

Force fields are a computationally cheap and quite accurate tool. They find wide application for the simulation of large and complex supramolecular assemblies, e.g., proteines in solution. However, by construction they have the disadvantage that the chemical bonding is fixed from the start, i.e., the user has to provide the chemical bonding pattern between the simulated atoms. This means that the force field cannot be used to determine the actual bonding pattern or to simulate the breaking and formation of covalent bonds.

2.3.3 Electronic structure calculations

The particular challenge of determining the covalent bonding between atoms is such that it involes the quantum mechanical nature of electrons: the interaction between atoms and molecules has its origin in the electronic structure of the atoms[†] which requires the solution of the (stationary, non-relativistic) Schrödinger equation for the electronic degrees of freedom,

$$\hat{H}_{\text{elec}}|\Psi\rangle = E|\Psi\rangle, \tag{12}$$

with the (electronic) Hamiltonian in atomic units,[14]

$$\hat{H}_{\text{elec}} = -\sum_i \frac{1}{2}\nabla_i^2 - \sum_{i,A} \frac{Z_A}{|\mathbf{r}_i - \mathbf{R}_A|} + \frac{1}{2}\sum_{i,j\neq i} \frac{1}{|\mathbf{r}_i - \mathbf{r}_j|}, \tag{13}$$

which includes the kinetic energy of the electrons, the Coulomb attraction between electrons ($\mathbf{r}_i$) and nuclei (at positions $\mathbf{R}_A$ and with charges Z_A), and the Coulomb repulsion

---

[*]They are also called *classical* force fields, because they model the intra-/intermolecular interaction on the level of classical physics.

[†]See the Hellman-Feynman-theorem at the beginning of this section.

between the electrons. In short, the electronic Hamiltonian can be expressed as a summation over single-particle Hamiltonians $\hat{h}_i$ and the electronic interactions,

$$\hat{H}_{\text{elec}} = \sum_i \left(\hat{h}_i + \frac{1}{2} \sum_{j \neq i} r_{ij}^{-1} \right), \tag{14}$$

with $r_{ij} = \left| \mathbf{r}_{ij} \right| = \left| \mathbf{r}_i - \mathbf{r}_j \right|$. Note that expressions (12)–(14) are correct only within the limit of the Born-Oppenheimer approximation, [15,16] i.e., the Hamiltonian, the wave functions, and the electronic energy depend parametrically on the positions of the nuclei, and the coupling between the motion of the nuclei and the electronic states is completely ignored. Unfortunately, an analytic solution of the eigenvalue problem (12) has only been found for the very simple case of a single hydrogen (or hydrogen-like) atom; in more complicated systems the electronic correlation also obstructs the numerical solution and further approximations are necessary.

There are many established methods in the field of theoretical physics and chemistry to perform such *ab initio* (or first-principles) electronic structure calculations, i.e., solving the electronic Schrödinger equation with sole usage of fundamental constants, and a full discussion of these methods is beyond the scope of this thesis. However, as a rough guide and because the basic ideas are still applied in modern methods, I will outline the historic development of electronic structure calculations. The method of choice for this thesis, density functional theory (DFT), will be addressed in Section 2.4 in more detail. The remainder of the present section will follow closely the review article by Jones & Gunnarsson[17] (1989) and the book of Szabo & Ostlund[18] (1996).

The basic approach to determine the ground state electronic structure is based on the Rayleigh-Ritz principle:[19] the electronic energy E is expressed as a functional of the electronic wave function $|\Psi\rangle$ and obeys the inequality

$$E[\Psi] = \frac{\langle \Psi | \hat{H}_{\text{elec}} | \Psi \rangle}{\langle \Psi | \Psi \rangle} \geq E[\Psi_0] = E_0. \tag{15}$$

The ground state energy E_0 and the corresponding ground state electronic wave function $|\Psi_0\rangle$ can be determined by variational minimization with, for practical reasons, a fixed functional form of $|\Psi\rangle$. One of the first attempts dates back to 1928, when Hartree[14] proposed to treat the full electronic wave function as a product of uncorrelated single-electron wave functions $|\psi_i\rangle$, the Hartree product:

$$|\Psi\rangle = |\psi_1\rangle |\psi_2\rangle |\psi_3\rangle \ldots \tag{16}$$

Substituting the Hartree product into Equation (15) and assuming orthonormality of the single-electron wave functions, which are also called spin orbitals, yields

$$E[\psi_1, \psi_2, \ldots] = \sum_i \left(\langle \psi_i | \hat{h}_i | \psi_i \rangle + \frac{1}{2} \sum_{j \neq i} \langle \psi_i | \langle \psi_j | r_{ij}^{-1} | \psi_j \rangle | \psi_i \rangle \right). \tag{17}$$

Now, we take the functional derivative with respect to $\langle \psi_m |$ under the constraint of normalized spin orbitals, i.e.,

$$\frac{\delta}{\delta \langle \psi_m |} \left(E\left[\psi_1, \psi_2, \dots\right] + \sum_i \mathscr{E}_i \left(1 - \langle \psi_i | \psi_i \rangle\right) \right) = 0, \tag{18}$$

which leads to a single-particle Schrödinger equation,

$$\left(\hat{h}_m + \sum_{j \neq m} \langle \psi_j | r_{mj}^{-1} | \psi_j \rangle \right) |\psi_m\rangle = \mathscr{E}_m |\psi_m\rangle. \tag{19}$$

This equation contains an averaged Coulomb interaction instead of the explicit electron-electron repulsion; $\mathscr{E}_m$ denotes the eigenvalue of the mth spin orbital. It is not trivial to assign a specific physical meaning to the spin orbital energies $\mathscr{E}_m$ in terms of classical analogies as has been extensively discussed in the literature; for a given system, however, the highest energy eigenvalue among the occupied spin orbitals is a good approximation for the ionization energy.[20]

Note that the Hamiltonian in Equation (19) depends on the single-electron wave functions $|\psi_{j \neq m}\rangle$ which, in turn, are to be determined by solving this eigenvalue problem. Therefore, Hartree proposed an iterative solution:

1. Start with an initial guess for $|\psi_1\rangle |\psi_2\rangle \dots$.

2. Compute the Hartree operators from the actual guess for $|\psi_1\rangle |\psi_2\rangle \dots$.

3. Solve the eigenvalue problem for $|\tilde{\psi}_1\rangle |\tilde{\psi}_2\rangle \dots$.

4. Repeat steps 2 and 3 until the eigenfunctions are self-consistent[*] with the actual guess, i.e., $|\tilde{\psi}_i\rangle \approx |\psi_i\rangle$, $i = 1, 2, \dots$

Shortly after Hartree proposed his approximation and the SCF method, Fock (1930) changed the approach such that Fermi statistics is satisfied by expressing the full wave function $|\Psi\rangle$ as a Slater determinant:[21]

$$|\Psi\rangle = \frac{1}{\sqrt{N!}} \begin{vmatrix} \psi_1(\mathbf{1}) & \cdots & \psi_N(\mathbf{1}) \\ \vdots & \ddots & \vdots \\ \psi_1(\mathbf{N}) & \cdots & \psi_N(\mathbf{N}) \end{vmatrix}. \tag{20}$$

The notation $\psi_i(\mathbf{j})$ marks that the spin orbital $|\psi_i\rangle$ is occupied by the jth electron; N is the number of electrons. This functional form ensures that $|\Psi\rangle$ is antisymmetric. In this case, application of the variational principle yields a similar single-particle Schrödinger equation,

$$\hat{f} |\psi_m\rangle = \mathscr{E}_m |\psi_m\rangle, \tag{21}$$

the famous Hartree-Fock[22,23] (HF) equation. The Fock operator $\hat{f}$, which depends like the Hartree operator[†] on the spin orbitals $|\psi_j\rangle$, is given by

---

[*]Because of the self-consistency condition in the last step, the name "self-consistent field" (SCF) method was coined for this iterative solution, which is still applied in modern electronic structure methods.

[†]In contast to Hartree's formulation in Equation (19), which requires a specific operator for each spin orbital, the Hartree-Fock approach allows for a single operator that depends on all spin orbitals simultaneously.

$$\hat{f} = \hat{h} + \sum_j \left(\hat{\mathscr{J}}_j - \hat{\mathscr{K}}_j \right). \tag{22}$$

The Hartree-Fock operator $\hat{f}$ includes the single-particle Hamiltonian $\hat{h}$, the Coulomb operator which we already know from Hartree's approach,

$$\hat{\mathscr{J}}_j = \langle \psi_j | r_{mj}^{-1} | \psi_j \rangle, \tag{23}$$

and a new term, the exchange operator:

$$\hat{\mathscr{K}}_j = |\psi_j\rangle \langle \psi_j | r_{mj}^{-1}. \tag{24}$$

The origin of the exchange operator lies in the indistinguishability of the electrons, and, in a Slater determinant, every electron can occupy every spin orbital. The characteristics of the exchange operator can be seen by its action on a spin orbital,

$$\hat{\mathscr{K}}_j |\psi_m\rangle = \left(\langle \psi_j | r_{mj}^{-1} | \psi_m \rangle \right) |\psi_j\rangle, \tag{25}$$

where $\hat{\mathscr{K}}_j$ exchanges the electrons from spin orbitals $|\psi_m\rangle$ and $|\psi_j\rangle$.

This general formulation of the Hartree and Hartree-Fock equations was the foundation of electronic structure calculations with the spin orbital as central variable.

2.3.4 A remark on spin treatment

In principle, we can write a spin orbital as a product of a spatial orbital and a spin function,

$$|\psi_i\rangle = |\chi_i\rangle |\sigma_i\rangle, \tag{26}$$

where the spin is either $|\sigma_i\rangle = |+\rangle$ or $|\sigma_i\rangle = |-\rangle$; we assume that these spin functions are orthonormal, i.e.,

$$\langle +|+\rangle = \langle -|-\rangle = 1 \tag{27}$$

and

$$\langle +|-\rangle = \langle -|+\rangle = 0. \tag{28}$$

With this, we can reformulate the Hartree and Hartree-Fock equations to obey specific restrictions for the spin arrangement; for example, if we assume in a HF calculation that each spatial orbital is occupied by exactly two electrons,

$$|\psi_{2i-1}\rangle = |\chi_i\rangle |+\rangle \tag{29}$$
$$|\psi_{2i}\rangle = |\chi_i\rangle |-\rangle, \tag{30}$$

and integrate over the spin degrees of freedom, we find the "restricted closed shell" formulation* of the Hartree-Fock operator,

---

*The corresponding "unrestricted open shell" formulation is extensively discussed in the literature.[18]

$$\hat{f} = \hat{h} + \sum_j \left(2\hat{\mathscr{J}}_j - \hat{\mathscr{K}}_j, \right) \tag{31}$$

which acts on the spatial orbitals:

$$\hat{f} \left| \chi_m \right\rangle = \mathscr{E}_m \left| \chi_m \right\rangle. \tag{32}$$

2.3.5 The numerical approach to electronic structure

Two decades after the Hartree-Fock approach, Roothaan & Hall (1951) proposed a further modification which enabled the efficient numerical treatment of the Hartree-Fock method:[24,25] while the initial HF method determined the functional form of the orbitals $\left| \chi_m \right\rangle$ analytically, Roothaan and Hall expanded the spatial orbital functions in a given set of basis functions $\left| \phi_\mu \right\rangle$:

$$\left| \chi_i \right\rangle = \sum_j C_{\mu m} \left| \phi_j \right\rangle, \tag{33}$$

with (complex) expansion coefficients $C_{\mu m}$. This expansion, substituted into Equation (32), yields

$$\sum_\mu C_{\mu m} \hat{f} \left| \phi_\mu \right\rangle = \mathscr{E}_m \sum_\mu C_{\mu m} \left| \phi_\mu \right\rangle. \tag{34}$$

From there, we multiply with $\left\langle \phi_\nu \right|$ from the left side,

$$\sum_\mu C_{\mu m} \left\langle \phi_\nu \right| \hat{f} \left| \phi_\mu \right\rangle = \mathscr{E}_m \sum_\mu C_{\mu m} \left\langle \phi_\nu \middle| \phi_\mu \right\rangle, \tag{35}$$

and identify $F_{\nu\mu} = \left\langle \phi_\nu \right| \hat{f} \left| \phi_\mu \right\rangle$ and $S_{\nu\mu} = \left\langle \phi_\nu \middle| \phi_\mu \right\rangle$ as matrix elements of the Fock operator and an overlap* matrix. Thus, the Hartree-Fock method can be formulated as a single matrix equation,

$$FC = SCE, \tag{36}$$

where F is the matrix of the Fock operator, S is the overlap between the individual basis functions, and E is a diagonal matrix of the orbital energies ($\mathscr{E}_1, \mathscr{E}_2, \ldots$). The unkown expansion coefficients in matrix C can now be obtained using numerical methods from linear algebra.

2.4 Density functional theory

The density functional approach[†] is conceptually very different from the previously described Hartree and Hartree-Fock methods. The idea to base a method on the electronic density instead of the wave function dates back to Thomas (1927) and Fermi (1928). However, the important breakthrough came with the Hohenberg-Kohn[27] theorems[‡] in

---

*In general, the basis functions $\left| \phi_1 \right\rangle, \left| \phi_2 \right\rangle, \ldots$ are not orthogonal.

†The outline in this section will follow the review of Jones & Gunnarsson[17] and the book of Martin.[26]

‡Here, I will follow the more general formulation from Percus[28] (1978) and Levy[29] (1979).

18

1964. Assume that the energy of a collection of N electrons can be written as a functional F of the electronic density $n(\mathbf{r})$:

$$F[n] = \min_{\Psi \to n} \langle \Psi | (\hat{T} + \hat{U}) | \Psi \rangle. \tag{37}$$

The operator $\hat{T}$ and $\hat{U}$ denote the kinetic energy and the electon-electron interaction; the minimization is performed over all wave functions $|\Psi\rangle$ that lead to the density n. Note that this formulation is indepentend of the actual system, i.e., it does not include any external potential or nucluei.[17] With this, the two theorems of DFT read:

$$E[n] = F[n] + \int \mathrm{d}^3 r \, V_{\text{ext}}(\mathbf{r}) \, n(\mathbf{r}) \geq E_0 \tag{38}$$

$$E[n_0] = F[n_0] + \int \mathrm{d}^3 r \, V_{\text{ext}}(\mathbf{r}) \, n_0(\mathbf{r}) = E_0, \tag{39}$$

where $E[n]$ is the total electronic energy and $V_{\text{ext}}(\mathbf{r})$ denotes an arbitrary external potential, for example due to the presence of the atomic nuclei. The ground state energy and the corresponding ground state density are given by E_0 and n_0.

2.4.1 Kohn-Sham equations

The ansatz of Kohn and Sham (1965) replaces the problem to minimize the Hohenberg-Kohn energy for a many-body system by the auxiliary problem for independent electrons.[30] In particular, the Kohn-Sham (KS) ansatz proposed a new expression for the energy,

$$E_{\text{KS}}[n] = T_0[n] + E_{\text{xc}}[n] + E_{\text{H}}[n] + \int \mathrm{d}^3 r \, V_{\text{ext}}(\mathbf{r}) \, n(\mathbf{r}), \tag{40}$$

that decouples the kinetic energy contribution of the independent electrons ($T_0[n]$) from the electrostatic part, and allows the approximation of correlation and exchange (E_{xc}) as a functional of the density.

Contemporary, we have a wide choice of different exchange and correlation (XC) functionals at hand, and each functional has its specific merits and weak points. The quest for better and more general XC functionals is a field of intense research. For my work, I have used the exchange[31] and correlation[32] functional by Becke, Lee, Yang, and Parr (BLYP).

In the Kohn-Sham ansatz, the electronic density is given as a sum of single-particle spin orbitals:

$$n(\mathbf{r}) = \sum_i \langle \psi_i | \mathbf{r} \rangle \langle \mathbf{r} | \psi_i \rangle = \sum_i |\psi_i(\mathbf{r})|^2 \tag{41}$$

The so-called Hartree energy,

$$E_{\text{H}}[n] = \frac{1}{2} \int \mathrm{d}^3 r \int \mathrm{d}^3 \tilde{r} \, \frac{n(\mathbf{r}) \, n(\tilde{\mathbf{r}})}{|\mathbf{r} - \tilde{\mathbf{r}}|}, \tag{42}$$

gives the electronic contribution to the Coulomb energy.

We apply the Rayleigh-Ritz principle to minimize the Kohn-Sham energy given by Equation (40):

$$\frac{\delta E_{KS}[n]}{\delta \psi_k^*(\mathbf{r})} = \frac{\delta T_0[n]}{\delta \psi_k^*(\mathbf{r})} + \left(\frac{\delta E_{xc}}{\delta n(\mathbf{r})} + \frac{1}{2} \int d^3\tilde{r} \, \frac{n(\tilde{\mathbf{r}})}{|\mathbf{r} - \tilde{\mathbf{r}}|} + V_{ext}(\mathbf{r}) \right) \frac{\delta n(\mathbf{r})}{\delta \psi_k^*(\mathbf{r})} \overset{!}{=} 0. \tag{43}$$

Under the constraint that the spin orbitals are orthonormal, we find the single-particle Kohn-Sham equation,

$$\left(-\frac{1}{2} \nabla^2 + V_{KS}(\mathbf{r}) \right) \psi_k(\mathbf{r}) = \mathscr{E}_k \psi_k(\mathbf{r}), \tag{44}$$

with the Kohn-Sham potential

$$V_{KS}(\mathbf{r}) = \frac{\delta E_{xc}}{\delta n} + \frac{1}{2} \int d^3\tilde{r} \, \frac{n(\tilde{\mathbf{r}})}{|\mathbf{r} - \tilde{\mathbf{r}}|} + V_{ext}(\mathbf{r}). \tag{45}$$

Like wave function-based electronic structure methods, the explicit treatment of the electron spin in a restricted closed shell picture allows to reformulate the Kohn-Sham equation in a spatial form,

$$\left(-\frac{1}{2} \nabla^2 + V_{KS}(\mathbf{r}) \right) \chi_k(\mathbf{r}) = \mathscr{E}_k \chi_k(\mathbf{r}), \tag{46}$$

with the spatial Kohn-Sham oribtals $\chi_k(\mathbf{r})$. Note that this notation requires a slightly modified expression of the electronic density:

$$n(\mathbf{r}) = \sum_i f_i \langle \chi_i | \mathbf{r} \rangle \langle \mathbf{r} | \chi_i \rangle = \sum_i f_i \left| \chi_i(\mathbf{r}) \right|^2. \tag{47}$$

The new parameter f_i that appears in Equation (47) corresponds to the actual occupation of the ith spatial orbital.[*] If we expand the Kohn-Sham orbitals and the density in an appropriate basis, the Kohn-Sham equation can be cast into matrix form,

$$\mathbf{KC} = \mathbf{SCE}, \tag{48}$$

where $\mathbf{K}$ denotes the matrix of the Kohn-Sham Hamiltonian; the other matrices are, like in the Hartree-Fock approach, the overlap matrix $\mathbf{S}$, the diagonal matrix of the orbital energies $\mathbf{E}$, and the matrix of the to-be-determined expansion coefficients $\mathbf{C}$.

2.4.2 Effective core potentials

Effective core potentials (ECPs) are an important tool to increase the efficiency of electronic structure methods. The idea is to replace the Coulomb potential of the atomic nuclei with an effective ionic potential such that the shielding effect of the core electrons on the valence electrons is included in the ECP. Hence, the tightly bound core electrons can be ignored in electronic structure calculations which significantly reduces the computational cost. Furthermore, ECPs are much smoother in the core region than the exact Coulomb potential which allows to use a smaller basis set.

---

[*]Similar to the HF method, it is also possible to derive an unrestricted open shell expression for the electron spin. In this case, the electronic density $n(\mathbf{r})$ is split up into two spin densities $n^\uparrow(\mathbf{r}), n^\downarrow(\mathbf{r})$.

Even though it seems a very drastic move to remove the core electrons from the electronic structure, the usage of ECPs is quite easily justifiable: the chemical properties of an atom are mostly determined by its valence electrons. The tightly bound core electrons act effectivly as a shield between the core charge and the valence electrons, and the orbital structure of the core electrons remains unchanged in most chemical reactions.

ECPs come in various forms and shapes of which I want to highlight especially the norm-conserving[33] analytical variant by Goedecker, Teter, and Hutter[34,35] (GTH). The GTH potential consists of a local part,

$$V_{\text{loc}}(\mathbf{r}) = -\frac{Z_{\text{ion}}}{r} \text{erf}\left(\frac{r}{\sqrt{2}r_{\text{loc}}}\right) + \exp\left(-\frac{r^2}{2r_{\text{loc}}^2}\right) \times \sum_{i=1}^{4} C_i \left(\frac{r}{r_{\text{loc}}}\right)^{2(i-1)}, \tag{49}$$

and several non-local contributions (angular momentum channels),

$$V_\ell(\mathbf{r}, \tilde{\mathbf{r}}) = \sum_{i=1}^{3}\sum_{j=1}^{3}\sum_{m=-\ell}^{\ell} Y_{\ell,m}(\mathbf{r}/r)\, p_i^\ell(r)\, h_{i,j}^\ell\, p_j^\ell(\tilde{r})\, Y_{\ell,m}^*(\tilde{\mathbf{r}}/\tilde{r}). \tag{50}$$

In the local part, r_{loc} and the C_i are numerical parameters, i.e., for the range of the local potential and polynomial coefficients; Z_{ion} denotes the valence charge of the nucleus. The non-local contributions are based on spherical harmonics $Y_{\ell,m}$ and projector functions:

$$p_i^\ell(r) = \frac{\sqrt{2}\, r^{\ell+2(i-1)} \exp\left(-\frac{r^2}{2r_\ell^2}\right)}{r_\ell^{\ell+(4i-1)/2} \sqrt{\Gamma\left(\ell + \frac{4i-1}{2}\right)}}. \tag{51}$$

The motivation of this form is to shift the overlap of the wave function with certain hydrogen-like atomic orbitals (given by the projectors and spherical harmonics) in energy to penalize the core electron states during the energy minimization; the actual shift is given by the parameter $h_{i,j}^\ell$ in Equation (50).

2.4.3 The GPW approach

Considering the expansion of orbitals in a specific basis, plane waves are the natural choice for systems with a periodic potential:

$$\phi_\mu(\mathbf{r}) = \frac{1}{\sqrt{\Omega}} \exp\left(i\mathbf{G}_\mu^T \mathbf{r}\right) \quad \text{or} \quad |\phi_\mu\rangle = |\mathbf{G}_\mu\rangle, \tag{52}$$

here with the volume of the periodic cell Ω and the reciprocal lattice vector $\mathbf{G}_\mu$.

Plane waves form a complete basis and enable the derivation of an efficient numerical form of the Kohn-Sham equation. According to the Bloch theorem, the (spatial) Kohn-Sham orbitals χ_j of a periodic system can be written as a product of a periodic function u_j and a plane wave:

$$\chi_j(\mathbf{r}, \mathbf{k}) = u_j(\mathbf{r}, \mathbf{k}) \exp\left(i\mathbf{k}^T \mathbf{r}\right). \tag{53}$$

Here, $\mathbf{k}$ is the wave vector. We expand u_j in a basis of plane waves and find:

$$\chi_j(\mathbf{r},\mathbf{k}) = \frac{1}{\sqrt{\Omega}} \sum_\mu C_{j,\mu}(\mathbf{k}) \exp\left(i\left(\mathbf{G}_\mu + \mathbf{k}\right)^T \mathbf{r}\right) = \sum_\mu C_{j,\mu}(\mathbf{k}) \phi_\mu(\mathbf{r},\mathbf{k}), \tag{54}$$

with the expansion coefficients $C_{j,\mu}(\mathbf{k})$. In the bra-ket notation, Equation (54) reads:

$$\left|\chi_j(\mathbf{k})\right\rangle = \sum_\mu C_{j,\mu}(\mathbf{k}) \left|\mathbf{G}_\mu + \mathbf{k}\right\rangle. \tag{55}$$

To derive the matrix expression of the Kohn-Sham equation in the plane wave basis, we apply the Kohn-Sham operator on a spatial orbital and multiply with $\langle \mathbf{G}_\nu + \mathbf{k}|$:

$$\left\langle \mathbf{G}_\nu + \mathbf{k}\right|\hat{H}_{\mathrm{KS}}\left|\chi_j(\mathbf{k})\right\rangle = \mathscr{E}_j \left\langle \mathbf{G}_\nu + \mathbf{k}\middle|\chi_j(\mathbf{k})\right\rangle. \tag{56}$$

This expression expands to

$$\sum_\mu C_{j,\mu}(\mathbf{k}) \left(-\frac{1}{2}\left\langle \mathbf{G}_\nu + \mathbf{k}\middle|\nabla^2\middle|\mathbf{G}_\mu + \mathbf{k}\right\rangle + \left\langle \mathbf{G}_\nu + \mathbf{k}\middle|\hat{V}_{\mathrm{KS}}\middle|\mathbf{G}_\mu + \mathbf{k}\right\rangle\right) = \mathscr{E}_j C_{j,\nu}(\mathbf{k}). \tag{57}$$

The kinetic energy term is easily evaluated:

$$-\frac{1}{2}\left\langle \mathbf{G}_\nu + \mathbf{k}\middle|\nabla^2\middle|\mathbf{G}_\mu + \mathbf{k}\right\rangle = \frac{1}{2}\left|\mathbf{G}_\mu + \mathbf{k}\right|^2 \left\langle \mathbf{G}_\nu + \mathbf{k}\middle|\mathbf{G}_\mu + \mathbf{k}\right\rangle = \frac{1}{2}\left|\mathbf{G}_\mu + \mathbf{k}\right|^2 \delta_{\nu,\mu}. \tag{58}$$

Matters complicate for the Kohn-Sham potential. However, if we expand this potential in a Fourier series,

$$V_{\mathrm{KS}}(\mathbf{r}) = \sum_\eta \tilde{V}_{\mathrm{KS}}\left(\mathbf{G}_\eta\right) \exp\left(-i\mathbf{G}_\eta^T \mathbf{r}\right), \tag{59}$$

where $\tilde{V}_{\mathrm{KS}}$ denotes the Fourier transform of the Kohn-Sham potential, we find:

$$\left\langle \mathbf{G}_\nu + \mathbf{k}\right|V_{\mathrm{KS}}\left|\mathbf{G}_\mu + \mathbf{k}\right\rangle = \sum_\eta \tilde{V}_{\mathrm{KS}}\left(\mathbf{G}_\eta\right)\left\langle \mathbf{G}_\nu + \mathbf{G}_\eta\middle|\mathbf{G}_\mu\right\rangle = \tilde{V}_{\mathrm{KS}}\left(\mathbf{G}_\mu - \mathbf{G}_\nu\right). \tag{60}$$

We substitute Equations (58) and (60) in Equation (57) and find the Kohn-Sham matrix equation in Fourier space:

$$\boldsymbol{KC} = \boldsymbol{CE}, \tag{61}$$

with the Kohn-Sham matrix

$$\boldsymbol{K}_{\nu,\mu} = \frac{1}{2}\left|\mathbf{G}_\mu + \mathbf{k}\right|^2 \delta_{\nu,\mu} + \tilde{V}_{\mathrm{KS}}\left(\mathbf{G}_\mu - \mathbf{G}_\nu\right). \tag{62}$$

Note that the plane wave basis is by construction infinite and must be truncated for practical use; this is usually done via an energetic cutoff:

$$\frac{1}{2}\left|\mathbf{k} + \mathbf{G}_\mu\right|^2 \leq E_{\mathrm{cut}}. \tag{63}$$

While it is very efficient to solve the Kohn-Sham equation in Fourier space, the calculation of the density in Fourier space scales quadratically with the (usually very large) number of basis functions and becomes very expensive for large systems. To solve this problem, we can make use of grids: if the Bloch states can be mapped on a grid

in real space, the calculation of the density follows by a simple squaring and summation over the individual grid points. Thus, with the help of Fast Fourier Transform (FFT) algorithms, the Kohn-Sham equation is solved in Fourier space, while the density is evaluated in real space.

The second basis set that I want to introduce in this section are (Gaussian type) localized atom-centered orbitals:

$$\phi_\mu(\mathbf{r}) = \exp\left(-\zeta_\mu \left|\mathbf{r} - \mathbf{R}_\mu\right|^2\right) Y_{\ell_\mu, m_\mu}(\mathbf{r}/r), \tag{64}$$

where ζ_μ is a numerical range parameter, $\mathbf{R}_\mu$ denotes the (to the index μ corresponding) atomic position, and $Y_{\ell, m}$ is a spherical harmonic. In contrast to plane waves, atom-centered orbitals offer a very intuitive interpretation of the electronic structure. The parameters of this basis must be chosen for the specific molecular environment which results in loss of generality. In pratice, we employ libraries with parameters for individual elements and different levels of flexibility, i.e., the number of Gaussians in each angular momentum channel and additional angular momentum channels which allow for polarization effects.

The most important feature of the Gaussian-based atomic-centered orbital basis is that all matrix elements of the Kohn-Sham operator can be evaluated analytically; this is mostly because of the mathematical feature that the product of two Gaussians conserves the Gaussian shape:

$$\exp\left(-\zeta_1 \left|\mathbf{r} - \mathbf{R}_1\right|^2\right) * \exp\left(-\zeta_2 \left|\mathbf{r} - \mathbf{R}_2\right|^2\right) = A_{1,2} \exp\left(-\zeta_{1,2} \left|\mathbf{r} - \mathbf{R}_{1,2}\right|^2\right) \tag{65}$$

with

$$\zeta_{1,2} = \zeta_1 + \zeta_2, \tag{66}$$

$$\mathbf{R}_{1,2} = \zeta_{1,2}^{-1}\left(\zeta_1 \mathbf{R}_1 + \zeta_2 \mathbf{R}_2\right), \tag{67}$$

and

$$A_{1,2} = \exp\left(-\zeta_1 \zeta_2 \zeta_{1,2}^{-1} \left|\mathbf{R}_1 - \mathbf{R}_2\right|^2\right). \tag{68}$$

Note that Gaussian functions themself might differ greatly from atomic orbitals; contracted gaussians (also called Slater type orbitals) are a modification of the original basis ansatz that retains all the advantages of Gaussian functions: instead of using a single Gaussian as radial function, we can use a linear combination of Gaussians with constant coefficients. Such a linear combination can easily be constructed in a way that it mimics the shape of an actual atomic orbital.

The atom-centered ansatz, however, has the downside that the dependence of the basis functions on the atomic positions gives rise to artificial forces (Pulay forces) upon displacement of the atoms if the basis set is not complete; plane waves are independent of the atomic positions and, thus, prevent this effect.

Modern electronic structure codes like CP2K[36–39] often employ a mixture of both basis schemes. The Gaussian Plane Wave[40] (GPW) ansatz uses two representations of the electronic density: an atom-centered representation,

$$n_{\mathrm{AC}}(\mathbf{r}) = \sum_{\mu,\nu} \boldsymbol{P}_{\mu,\nu} \phi_\mu(\mathbf{r}) \phi_\nu(\mathbf{r}), \tag{69}$$

that is expanded in a basis of contracted Gaussians ϕ_μ, $\boldsymbol{P}$ denotes the density matrix (expansion coefficients), and a second representation,

$$n_{\mathrm{PW}}(\mathbf{r}) = \frac{1}{\Omega} \sum_{\mathbf{G}} \tilde{n}(\mathbf{G}) \exp\left(i\mathbf{G}^T \mathbf{r}\right), \tag{70}$$

that uses an auxiliary basis of plane waves; the coefficients $\tilde{n}(\mathbf{G})$ are such that

$$n_{\mathrm{PW}}(\mathbf{r}) = n_{\mathrm{AC}}(\mathbf{r}). \tag{71}$$

The efficient conversion from one density representation into the other is achieved via FFT algorithms.

The GPW approach allows to use the efficient analytical expressions of Gaussians for thecalculation of the kinetic energy of the electrons and their interaction with the nuclei (via ECPs), and it employs the plane wave representation to calculate the Hartree and exchange-correlation energies.

2.5 Molecular dynamics

In the previous sections, I have described how a chemical system can be represented on the computer (Section 2.2) and how the interactions between the atoms and molecules can be modeled on various levels of theory (Sections 2.3–2.4). Here, I will introduce the concept of molecular dynamics (MD) which allows to simulate the dynamics of atomic/molecular systems.[*]

2.5.1 Statistical mechanics

The systems that we study in chemical physics usually are too large and complex for an analytical treatment, even though the pair-wise interaction is often quite well-understood. The framework of statistical mechanics offers tools to determine static and dynamic properties of such complex systems, and the concept of state functions is used to describe the macroscopic behavior based on the system's microstates. A case in point with great importance in the field of chemistry is the entropy $S(N, V, E)$ which describes the number of microstates (positions and momenta of the individual particles) that correspond to a macroscopic state (with N particles, volume V and energy E).

Particularly useful is the differential expression of the entropy,

$$dS = \left(\frac{\partial S}{\partial E}\right)_{N,V} dE + \left(\frac{\partial S}{\partial V}\right)_{N,E} dV + \left(\frac{\partial S}{\partial N}\right)_{V,E} dN, \tag{72}$$

as it relates properties like temperature (T), pressure (p), and chemical potential (μ) to the energy, the volume, and the particle number of the system via the partial derivatives:

---

[*]Section 2.5 will closely follow Mark Tuckerman's book on statistical mechanics,[41] in particular chapters 2–4.

$$\left(\frac{\partial S}{\partial E}\right)_{N,V} \quad = \quad \frac{1}{T} \tag{73}$$

$$\left(\frac{\partial S}{\partial V}\right)_{N,E} \quad = \quad \frac{p}{T} \tag{74}$$

$$\left(\frac{\partial S}{\partial N}\right)_{V,E} \quad = \quad -\frac{\mu}{T}. \tag{75}$$

The entropy itself is linked to the number of microstates within a given energy hypersurface,

$$S(N,V,E) = k_{\mathrm{B}} \ln\left(\Gamma\left(N,V,E\right)\right), \tag{76}$$

which, in the Hamilton formalism, is given by the phase space volume

$$\Gamma(N,V,E) = \mathcal{N} \int \mathrm{d}^{6N}x \, \delta\left(\mathcal{H}(\mathbf{x}) - E\right). \tag{77}$$

The phase space vector $\mathbf{x} = (\mathbf{r}_1, \mathbf{p}_1, \ldots, \mathbf{r}_N, \mathbf{p}_N)$ denotes the $6N$ degrees of freedom (spatial and momentum) of a system of N particles, $\mathcal{N}$ is a normalization factor, and $\mathcal{H}$ is the Hamiltonian of the system; the δ-distribution restricts the integral to the hypersurface with constant energy E.[*] The factor k_{B} in Equation (76) is Boltzmann's constant.

In a statistical sense, any observable Ω can now be computed as an averaged value over the (normalized) phase space volume,

$$\langle\Omega\rangle = \frac{\int \mathrm{d}^{6N}x \, \Omega(\mathbf{x}) \, \delta(\mathcal{H}(\mathbf{x}) - E)}{\int \mathrm{d}^{6N}x \, \delta(\mathcal{H}(\mathbf{x}) - E)}, \tag{78}$$

i.e., as an ensemble average over all microstates $\mathbf{x}$ within the hypersurface.

2.5.2 Integration of Hamilton's equations of motion

In the general case, the integrals in Equations (77) and (78) cannot be evaluated analytically and one has to resort to approximations or a numerical treatment. The first step towards the latter is to find an alternative to the ensemble averge: according to the Ergodicity hypothesis, we can replace the evaluation of the phase space integral by a sufficiently long time integral:

$$\langle\Omega\rangle = \frac{\int \mathrm{d}^{6N}x \, \Omega(\mathbf{x}) \, \delta(\mathcal{H}(\mathbf{x}) - E)}{\int \mathrm{d}^{6N}x \, \delta(\mathcal{H}(\mathbf{x}) - E)} = \lim_{\tau \to \infty} \frac{1}{\tau} \int_0^\tau \mathrm{d}t \, \Omega\left(\mathbf{x}(t)\right). \tag{79}$$

Note that, in the microcanonical ensemble, the trajectory $\mathbf{x}(t)$ is restricted to its initial hypersurface. The time evolution of the phase space vector $\mathbf{x}(t)$ is given by the Hamilton formalism:

---

[*]In the microcanonical ensemble, the system is isolated and cannot exchange energy or particles with its environment.

$$\dot{r}_i \;=\; \frac{\partial \mathcal{H}}{\partial p_i}, \tag{80}$$

$$\dot{p}_i \;=\; -\frac{\partial \mathcal{H}}{\partial r_i}. \tag{81}$$

Furthermore, we switch from continuous time t to a discrete representation,

$$t \to t_k = t_0 + k\Delta_{\rm t}, \tag{82}$$

with discrete time steps of length $\Delta_{\rm t}$, $k = 0, 1, \ldots$, and an arbitrary time offset t_0. The statistical average of an obervable Ω can then be computed over $N_{\rm T}$ discrete time steps,

$$\langle \Omega \rangle \approx \frac{1}{N_{\rm T}} \sum_{k=1}^{N_{\rm T}} \Omega(\mathbf{x}(t_k)), \tag{83}$$

using a suitable integration scheme to propagate the phase space vector $\mathbf{x}(t)$ appropriately.

2.5.3 Velocity Verlet algorithm

To evaluate Equation (83) for a specific observable, we need a numerical integration scheme to propagate the phase space vector $\mathbf{x}(t)$ from a given initial state $\mathbf{x}(0)$. For this aim, we model the dynamics (of particle i) via finite differences in time and do a Taylor expansion to the quadratic order:

$$\mathbf{r}_i(t + \Delta_{\rm t}) = \sum_{n=0}^{\infty} \frac{\Delta_{\rm t}^n}{n!} \frac{\partial^n}{\partial t^n} \mathbf{r}_i(t) \approx \mathbf{r}_i(t) + \Delta_{\rm t}\dot{\mathbf{r}}_i(t) + \frac{\Delta_{\rm t}^2}{2}\ddot{\mathbf{r}}_i(t). \tag{84}$$

We identify the first time derivative as a velocity ($\mathbf{v}_i = \dot{\mathbf{r}}_i$); the second derivative relates to an acceleration ($\mathbf{a}_i = \ddot{\mathbf{r}}_i$) and in combination with Newton's second law to a force ($\mathbf{a}_i = \mathbf{F}_i / m_i$). With this, we find:

$$\mathbf{r}_i(t + \Delta_{\rm t}) \approx \mathbf{r}_i(t) + \Delta_{\rm t}\mathbf{v}_i(t) + \frac{\Delta_{\rm t}^2}{2m_i}\mathbf{F}_i(t). \tag{85}$$

In the same way, we can derive the time-inverted expression:

$$\mathbf{r}_i(t - \Delta_{\rm t}) \approx \mathbf{r}_i(t) - \Delta_{\rm t}\mathbf{v}_i(t) + \frac{\Delta_{\rm t}^2}{2m_i}\mathbf{F}_i(t). \tag{86}$$

By adding Equations (85) and (86) and solving for $\mathbf{r}_i(t + \Delta_{\rm t})$, we find the famous Verlet algorithm,[42]

$$\mathbf{r}_i(t + \Delta_{\rm t}) \approx 2\mathbf{r}_i(t) - \mathbf{r}_i(t - \Delta_{\rm t}) + \frac{\Delta_{\rm t}^2}{m_i}\mathbf{F}_i(t), \tag{87}$$

which allows for the numerical integration of the equations of motion (EOMs).

Note that this integration scheme is independent from the velocities of the particles. It is still possible to compute the missing velocities from the spatial trajectory via a simple finite differences expression,

$$\mathbf{v}_i(t) \approx \frac{\mathbf{r}_i(t + \Delta_t) - \mathbf{r}_i(t - \Delta_t)}{2\Delta_t}. \tag{88}$$

Yet, the velocity independence of the Verlet algorithm comes with the huge drawback that the Hamiltonian is not conserved by this integration scheme. This means that a trajectory $\tilde{\mathbf{x}}(t)$ which is determined by the Verlet integrator diverges from the true trajectory $\mathbf{x}(t)$.

To include the velocities again in our integration scheme, we make a time shift ($t \to t + \Delta_t$) in Equation (86) and substitute for $\mathbf{r}_i(t)$ in Equation (85):

$$\mathbf{r}_i(t + \Delta_t) \approx \mathbf{r}_i(t + \Delta_t) - \Delta_t \mathbf{v}_i(t + \Delta_t) + \frac{\Delta_t^2}{2m_i}\mathbf{F}_i(t + \Delta_t) + \Delta_t \mathbf{v}_i(t) + \frac{\Delta_t^2}{2m_i}\mathbf{F}_i(t). \tag{89}$$

Now, we eliminate the spatial dependency and solve for $\mathbf{v}_i(t + \Delta_t)$:

$$\mathbf{v}_i(t + \Delta_t) \approx \mathbf{v}_i(t) + \frac{\Delta_t}{2m_i}\left(\mathbf{F}_i(t + \Delta_t) + \mathbf{F}_i(t)\right). \tag{90}$$

The combination from Equations (85) and (90), known as the Velocity Verlet[43] algorithm, is a case in point for simplectic integrators. The Velocity Verlet (VV) algorithm does not conserve the Hamiltonian $\mathcal{H}(\mathbf{x})$ itself; however, it can be shown that a simplectic integrator conserves a "shadow Hamiltonian" $\tilde{\mathcal{H}}(\mathbf{x}, \Delta_t)$ which converges towards the exact Hamiltonian as the time step approaches zero:

$$\mathcal{H}(\mathbf{x}) = \lim_{\Delta_t \to 0} \tilde{\mathcal{H}}(\mathbf{x}, \Delta_t). \tag{91}$$

As a consequence, the trajectory $\tilde{\mathbf{x}}(t)$ determined by a simplectic integrator is always bound to the exact trajectory $\mathbf{x}(t)$ as long as the time step is sufficiently small.

2.5.4 Canonical ensemble

The Velocity Verlet algorithm enables to integrate the equations of motion for a molecular system in the microcanonical ensemble, i.e. with constant values for the number of particles, the volume, and the energy. A realistic experiment, however, is rarely performed completely isolated. A more appropriate description would need to allow for a coupling of the simulated system with its environment, e.g., with a heat bath.

In the canonical ensemble, the system is in thermal contact with its environment and can exchange energy; hence, a simulation in the canonical ensemble must be performed for constant temperature rather than constant energy. Considering the statistical description, we have to use a different state function to describe the macroscopic states in the canonical ensemble than in the microcanonical ensemble. For this aim, we take the differential expression of the microcanonical energy,

$$dE = T\,dS - p\,dV + \mu\,dN, \tag{92}$$

and perform a Legendre transformation to exchange the entropy for the temperature as state variable:

$$F(N, V, T) = E(N, V, S(N, V, T)) - TS(N, V, T). \tag{93}$$

This state function is called Helmholtz free energy; its change relates to the performed work when a system changes its state along a reversible path. The differential form of the Helmholtz free energy is:

$$dF = \mu \, dN - p \, dV - S \, dT. \tag{94}$$

The Helmholtz free energy can be related to the distribution of microstates via

$$F(N, V, T) = -k_B T \ln (Z(N, V, T)), \tag{95}$$

where k_B denotes Boltzmann's constant and $Z(N, V, T)$ is the (canonical) partition function:

$$Z(N, V, T) = \sum_j \exp\left(-\frac{E(\mathbf{x}_j)}{k_B T}\right). \tag{96}$$

Here, $\mathbf{x}_j$ denotes a microstate and $E_j = E(\mathbf{x}_j)$ is its energy. The exponential term is called a Boltzmann factor and relates to the statistical probability of the microstate $\mathbf{x}_j$ when the system is at thermal equilibrium with a heat bath at temperatur T. Hence, the partition function Z is the sum of all possible microstates which are weighted by their Boltzmann factors.

In an actual molecular dynamics simulation, we use thermostat algorithms to enforce a constant temperature. The velocity-rescaling approach is a very straightforward ansatz that uses the rescaling of the particle velocities by a factor α_{VR} at each MD step. This factor is chosen such that the average kinetic energy per degree of freedom yields the desired temperature. Unfortunately, this simple approach does not sample the canonical distribution correctly, as realistic systems show energy fluctuations due to the thermal coupling.

Several elaborate thermostats have been proposed to account for these energy fluctuations; among them are the stochastic Andersen thermostat,[44] the velocity-rescaling-based Berendsen thermostat,[45] and Nosé-Hoover chains.[46,47]

An interesting ansatz by Bussi, Donadio, and Parrinello seizes upon the Berendsen thermostat. Their "canonical sampling through velocity rescaling" (CSVR) algorithm follows the idea to rescale the atomic velocites with a factor α_{VR}; this factor, however, is taken from an auxiliary continuous stochastic dynamics in such a way that the canonical distribution is sampled correctly.[48]

2.5.5 A remark on *ab initio* molecular dynamics

The term molecular dynamics (MD) relates to the numerical integration of the equations of motion of a system of interacting bodies* in general. Many researchers, however, understand MD simulations as strictly classical simulations, i.e., the interaction is modeled on the classical level.† To avoid confusion, I will follow the notion that the term classical

---

*This is not restricted to atoms and molecules; the MD technique is also applied outside of chemical physics, e.g. in the simulation of celestial bodies in astrophysics.

†See Sections 2.3.2 and 2.3.3 for the classical and the first-principles (quantum mechanical) approach to model atomic/molecular interactions.

MD relates to an MD simulation using force fields; hence, *ab initio* (or first-principles) MD denotes that the inter-/intramolecular interaction is based on electronic structure theory, and the forces are calculated from the electronic ground state density according to the Hellmann-Feynman-theorem.

The classical and quantum mechanical approaches differ greatly in the computational effort and scalability. With force fields, it is easily possible to simulate systems on the order of 10^5 particles on the nano second time scale. Electronic structure calculations on the level of density functional theory scale well for much smaller systems in the range of 10–1000 atoms. The ground state electronic structure depends parametrically on the atomic positions; hence, the electronic ground state has to be determined in each *ab initio* MD step. This renders molecular dynamics simulations from first-principles very expensive and such simulations are usually performed over the range of 10–100 ps.

3 Review of the content of this thesis

The simulation of large and complex molecular systems is a very challenging task, especially under realistic conditions. The particular topic addressed in my work is proton conduction in fuel cell membranes. The computational modeling of this transport phenomenon is still far from being a routine problem, despite the fast development of computational infrastructure.

The phenomenon of ion conduction in condensed matter in general consists of a multitude of facets. In this thesis, I address several aspects of this problem which cover large-scale electronic structure calculations and the development of large-scale methods. In particular, this work focuses on four relevant subprojects:

1. Hydrogen bonds represent one of the most common driving forces behind the formation of supramolecular structures and they determine structural as well as dynamical properties of numerous functional materials. I discuss how *ab initio* spectroscopy calculations help to understand structural motifs of hydrogen bond networks in condensed phases, and I emphasize in particular the importance of the dynamical properties of hydrogen bond networks for proton transport. [Publication P1]

2. Hybrid quantum-classical (QM/MM) calculations combine the ability of classical methods to treat large molecular systems with the advantage of quantum methods to model chemical processes within smaller fragments of the system. Here, I have developed an approach to increase the accuracy of QM/MM calculations with a particular emphasis on spectroscopic parameters; this approach aims at extending the applicability of first-principles spectroscopy calculations to large-scale systems. [P2,P3]

3. Molecular structure prediction by means of numerical calculations is one of the evergreen problems but also one of the most difficult challenges in chemical physics. Specifically the determination of the global minimum structure is a field of intense research. For this aim, I have developed a stochastic, swarm intelligence-based optimization algorithm to the problem of global geometry optimization. [P4]

4. On the application level, I have performed large-scale atomistic simulations with electronic structure methods to elucidate the proton conduction mechanism of an organic compound that is a promising material for proton exchange membranes for fuel cells. This study specifically targets the direct motion of individual protons in the dynamically fluctuating hydrogen bond network topology. [P5]

3.1 Structure-property-relationships: spectroscopic fingerprints of hydrogen bond networks

When we consider the interaction between atoms and molecules, we observe different types of bonding and forces: there are, among others, covalent and ionic bonds, hydrophobic effects, and van der Waals forces. We know from the Hellman-Feynman theorem[1] that all these interactions are different manifestations of the same basic interaction

which is in its essence of electrostatic nature. Yet, it is useful to regard all these manifestations individually in the description of molecular structure and dynamics as they act on very specific ranges, energy scales, and life times.
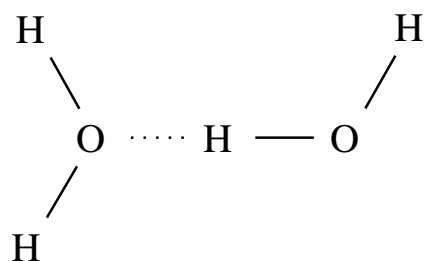
One of the most common fundamental driving forces behind the formation of supramolecular structure are hydrogen bonds, i.e., the attraction between polar molecules or polar regions of a single molecule (see Figure 2). Hydrogen bonds, for example, play an important role in the stabilization of secondary structure patterns in proteins.

Figure 2: Sketch of a hydrogen bond (dotted line) between two water molecules.

Molecular structure is one of the most basic observables in numerical calculations. The potential energy surface (PES) that such a calculation is based on exhibits in general many local minima at which the system is effectively void of atomic forces; hence, the PES is locally quadratic close to equilibrium geometries which results in a strong effect of small perturbative forces.

Spectroscopic observables on the other hand often exhibit a different behaviour close to equilibrium geometries, and even small strutural variations can lead to considerable changes in the computed (or experimentally observed) spectra. Thus, it is often much more helpful to characterize molecular structure based on spectroscopic observables than on the corresponding potential energy.

Unfortunately, the energetics of hydrogen bonding and other comparably weak interactions like van der Waals forces are not very well described by density functional theory (DFT) methods. In case of liquid water, for example, DFT-based constant pressure molecular dynamics simulations have a tendency to overstructure the liquid and yield a density that is considerably below the experimental one; this, however, can be corrected on the semiempirical level.[49]

With appropriate care, the first-principles calculation of spectroscopic observables can be used to characterize local packing motifs in condensed phases; bulk nuclear magnetic resonance (NMR) chemical shifts, for example, describe the change in an NMR resonance of a molecule due to crystallization and, hence, can be used to identify accurately individual spectroscopic signatures of packing effects.[50]

Matters complicate for systems without a homogeneous morphology, e.g., polymers which include loops and density variations, and a DFT-based approach cannot take into account the full structural complexity. Still, the microscopic picture can be modeled accurately on local length scales. A case in point is poly-viny-phosphonic acid (PVPA) which is a promising material for application in proton conducting fuel cell membranes, see Figure 3 (left). PVPA is a polymer that has been functionalized with phosphonic acids, and a strong hydrogen bond network connects the individual acidic groups and intercalating water molecules.

In regard to proton conduction, we also have to consider the dynamical properties of the hydrogen bond network in PVPA.* The intrinsic time scales of the hydrogen bonds

---

*An earlier first-principles molecular dynamics study revealed that the proton conduction mechanism is a combined Grotthuss and vesicle mechanism, and the hydrogen bonds are the primary transfer paths
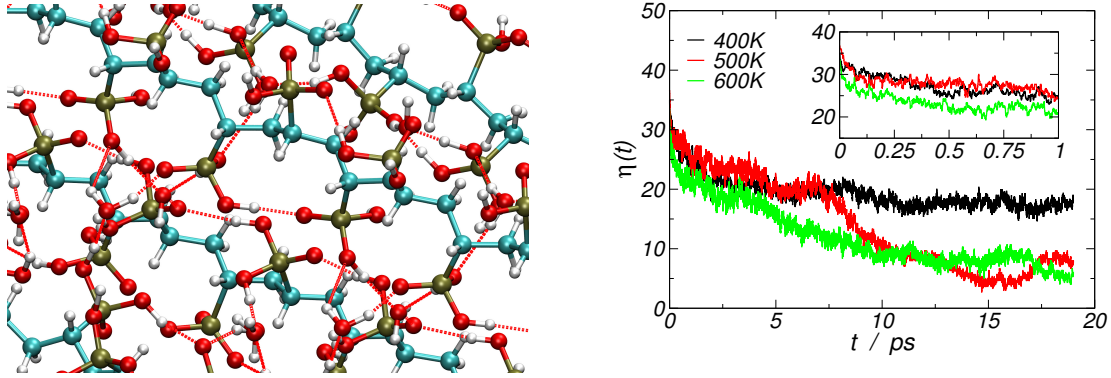
Figure 3: The local hydrogen bond network of poly-vinyl-phosphonic acid (PVPA) involves intra- and intermolecular bonds between the phosphonic acids and intercalated water molecules[51] (left); the hydrogen bond autocorrelation function η characterizes the evolution of the local hydrogen bond network of PVPA (right).

can be characterized via a hydrogen bond network correlation function $\eta_{hbn}(t)$ that gives the average number of hydrogen bonds of the network at an arbitrary time t_0 which still exist at a time $t + t_0$. This correlation function is defined as

$$\eta_{hbn}(t) = \left\langle \sum_{k=1}^{N_H} \tilde{\delta}_{H_k^{hbn}(t_0+t), H_k^{hbn}(t_0)} \right\rangle_{t_0}, \tag{97}$$

where H_k^{hbn} gives the bonding partners of the kth hydrogen at time t_0 (respective $t + t_0$); hence, $\tilde{\delta}$ equals 1 if the partners are identical at both times and 0 if they differ. Figure 3 (right) shows this hydrogen bond correlation function at different temperatures. While there is no qualitative difference with the range 400–600 K, we observe a faster decay at higher temperatures; in all cases, the correlation function reaches a plateau after roughly 10–20 ps which illustrates the special character of the hydrogen bond network as imposed by the polymer's superstructure.

3.2 Improvement of hybrid quantum-classical (QM/MM) methods

When it comes to electronc structure calculations, DFT is a very powerful and widely used tool. It is fairly accurate and scales well up to roughly 10^3 atoms. This, however, straitens its applicability to biomolecular systems which often consist of $10^4 - 10^6$ atoms; at this scale, force field molecular dynamics simulations have to be used. However, there are difficulties to simulate chemical reactions that involve breaking and formation of covalent bonds on the level of classical force fields.

Hybrid quantum-classical (QM/MM) methods offer a way to combine the advantages from both, classical and quantum mechanical methods. In the quantum-classical framework,[52] the molecular system is repartitioned into a QM fragment that is mode-

---

for protons between the acidic groups and intercalating water molecules.

led at the quantum mechanical level, and that is embedded in the usually much larger remainder of the system which is treated on the classsical level (the MM fragment).
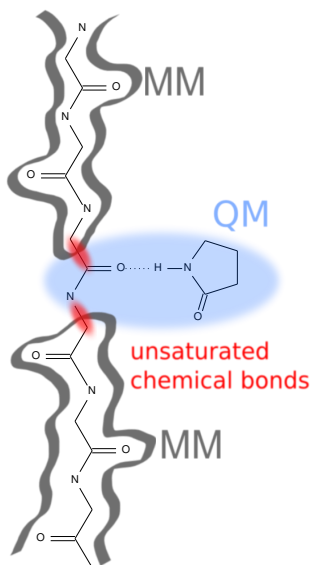

Figure 4: QM/MM repartitioning scheme.

In some cases, however, a covalent bond might cross the quantum-classical boundary and is broken as a consequence of the repartitioning; this situation is sketched in Figure 4. Within the QM region, this results in a dangling bond with an unpaired electron which has to be saturated somehow.

To solve the saturation problem at the bond cleavage site, several conceptually different methods have been established. Among the most common approaches are usage of hydrogen[53] or flourine[54] link atoms, frozen atomic orbitals,[55,56] generalized hybrid orbitals,[57–59] quantum capping potentials,[60–63] and designed heptavalent capping potentials.[64]

The method that I have used in my work is conceptually close to the hydrogen link atom approach[53] and is based on an earlier project.[65–67] In particular, this method uses analytical effective core potentials[34,35] (ECPs) to saturate the dangling bonds at the quantum-classical boundary in such a way, that the electronic structure in the QM region is as close as possible to a full quantum reference.

A "penalty" functional $\mathscr{P}$ is used to characterize the quality of such a capping potential V_{cap}: this functional measures how good the capping potential reproduces the original electronic density (from the full quantum reference) and the forces on the nuclei $\mathbf{F}_i$:

$$\mathscr{P}\left[V_{\text{cap}}\right] = \omega_n \Delta n_0 + \omega_F \Delta F \tag{98}$$

$$\Delta n_0 = \int_\Omega \mathrm{d}^3 r \left(n_0^{(\text{ref})}(\mathbf{r}) - n_0^{(\text{cap})}(\mathbf{r})\right)^2 \tag{99}$$

$$\Delta F = \sum_k \left|\mathbf{F}_k^{(\text{ref})} - \mathbf{F}_k^{(\text{cap})}\right|^2 \tag{100}$$

The scalars ω_n and ω_F in Equation (98) are weighting factors for the density and force contribution to the total penalty. In Equation (99), the integration area Ω is usually chosen as spheres around the atoms within the QM region and explicit exclusion of spheres around the link atoms. The force penalty in Equation (100) is important to enforce chemical stability of the capping bonds.

With this penalty functional, we are able to quantify the repartitioning error for a given capping potential, and variational minimization of this penalty with respect to V_{cap} leads to a capping potential with optimal saturation capability.

The corrugated shape of the penalty functional's hypersurface, however, complicates the minimization process: numerous local minima prevent a straight forward minimization path and a global optimization approach is needed to prevent local minima

trapping. To tackle this particluar problem, I have chosen a stochastic, gradient-free optimization algorithm from the field of swarm intelligence[68–70] and implemented a modified version into the DFT program package CPMD.[71]
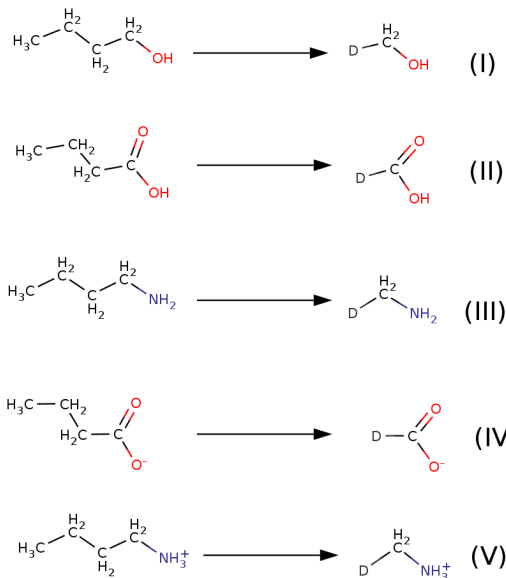

Figure 5: QM/MM repartitioning for several polar and charged biomolecular groups.

In a first study [P2], I could show that this capping potential optimization approach leads to a better repartitioning error than the common hydrogen link atom approach, especially when we consider the calculation of spectroscopic parameters, e.g., NMR chemical shifts which are very sensitive to the electronic structure.

In a second study [P3], we examined the influence of particular charged or polar groups (Figure 5 shows all the addressed polar and charged groups and the corresponding repartitioning) in the close proximity of the cleavage site; such situations appear quite frequently in the simulation of biomolecular systems, e.g., photoreceptor proteins.[72–78] The results showed that the optimization of capping potentials for specific cleavage situations (the proximity of specific charged/polar groups) is favorable over a generalized capping potential.

3.3 Development of a stochastic geometry optimizer

In the methodological improvement in the aforementioned project (section 3.2), the optimization of capping potentials for QM/MM calculations, I have employed a stochastic optimization algorithm from the field of swarm intelligence. This algorithm, known as the Artficial Bee Colony[68–70] (ABC) algorithm, mimicks the foraging behaviour of honey bees and had, at that time, already been recognized in enigneering[79–82] and computer science.[83–86] In physics and chemistry, however, this approach was virtually unkown.

The successful application of the ABC algorithm to the optimization of capping potentials has led us to transfer this algorithm to other global optimization problems in computational chemical physics: the optimization of molecular geometry (see Figure 6).

Finding the optmial conformation of a molecule or a supramolecular assembly is, despite the conceptual simplicity, a highly non-trivial task and far from being a routine problem. Based on the type of intra-/intermolecular interaction, the potential energy surface (PES) of the system exhibits a large number of local minima with (usually) high energetic barriers between the metastable conformations. The common approach for molecular geometry optimization employs in general a very efficient local minimization strategy like conjugated gradients (CG) or a Broyden-Fletcher (BFGS) method; however, this approach leads straight to the next local minimum structure in which the optimization process becomes trapped.
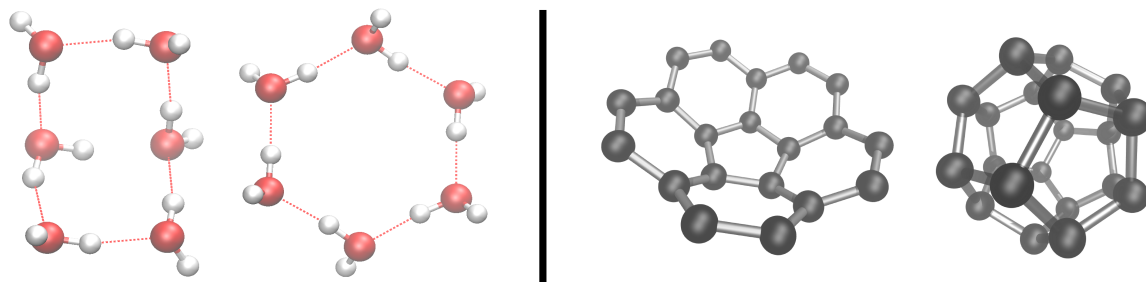
35

Figure 6: Two examples of molecular clusters: six rigid water molecules (left) in the booklet structure and the energetically more favorable hexagonal structure; 20 carbon atoms (right) showing the open bowl and the cage structure.
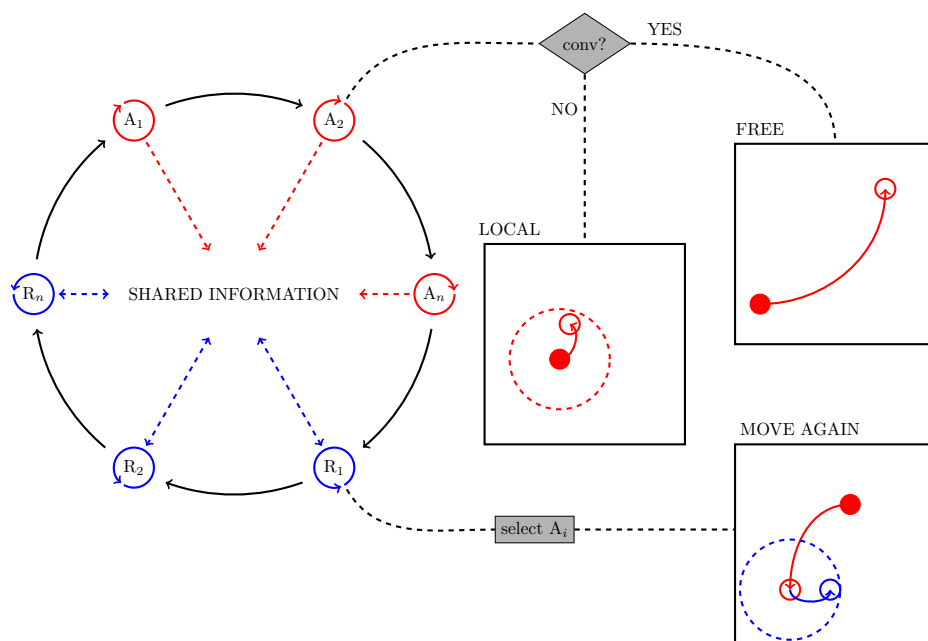

Figure 7: Schematic description of the artificical bee colony algorithm.

More elaborated global optimization techniques, e.g., basin hopping[87–91] (BH), minima hopping[92–96] (MH), or (gradient) tabu search,[97–100] employ combinations of local minimization algorithms and escaping strategies to leave local minima; such can be short molecular dynamics runs or steered moves in direction of smooth ascend of the PES. Additionally, genetic algorithms[101–109] (GA) combining gradient-based local minimization and a global search pattern have proven to be very efficient. While there are several different global optimization approaches available, many researchers agree that there is up to date no "best" technique and every algorithm has its particular merits and frailties.

In Reference [P4], I have presented a version of the ABC algorithm (see Figure 7) that has been modified for the optimization of molecular cluster structures without employing gradient or symmetry information from the underlying interaction potential. The performance of the algorithm has been studied using highly relevant classical intermolecular potentials, namely the distance-based Morse[4] and Lennard-Jones[3] potentials (rare

gases) and TIP5P[7] (rigid water molecules); the resulting global minima structures were then compared with reference structures from the Cambridge Cluster Database.[110] The results showed that the modified ABC algorithm is able to reproduce the a priori known global minima for conceptually different interaction potentials with a single, generalized setting and without knowledge of any symmetries or gradient information of the PES.

3.4   Proton conduction in fuel cell membranes

Hydrogen has a high potential as energy carrier in the field of renewable and clean energy. The conversion of chemical energy into electrical energy can be performed in a fuel cell (FC). Such a fuel cell uses the released energy from a chemical reaction and transforms it into electric energy. The most common setup is the proton exchange fuel cell (PEMFC) which employs the highly exothermic redoxreaction of hydrogen and oxygen to water:

$$H_2 \quad \rightarrow \quad 2H^+ + 2e^- \tag{101}$$

$$\frac{1}{2}O_2 + 2H^+ + 2e^- \quad \rightarrow \quad H_2O \tag{102}$$

This type of fuel cell consists of three parts: a catalyst at the andode side (hydrogen is split up into protons and electrons), another catalyst at the cathode side (where the oxygen is added), and a proton conducting membrane that separates the two sides.

In general, fuel cells have a very low environmental impact due to the simple by-product (water) and frugal fuel (hydrogen). Unfortunately, state-of-the-art membrane materials like Nafion® also have a low operating efficiency and therefore a very limited applicability. The efficiency depends on the catalytic dissociation of hydrogen and oxygen; hence, it depends on the operation temperature and the amount of catalyst which is usually platinum-based. As a consequence, the search for high-temperature membrane or separator materials is a field of intense research.
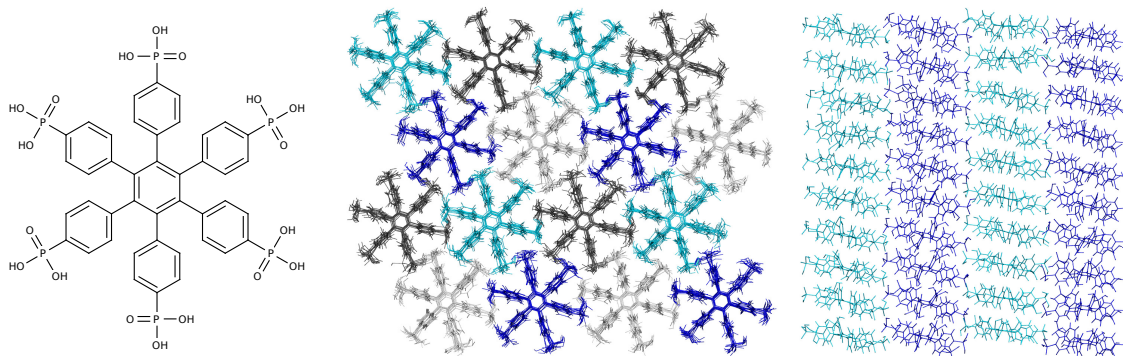

Figure 8: Molecular structure of hexakis(p-phosphonatophenyl)benzene (left); supramolecular structure of 160 hexakis(p-phosphonatophenyl)benzene molecules that appeared after 10 ns during a classical equilibration in the NPT ensemble: top view (middle) and side view (right).

In the progress of this search, experimentalists suggested to exploit the amphoteric properties of phosphonic acids[111,112] which are known to have one of the highest proton conductivities in their liquid state. A particular example that employs phosphonic acids is PVPA[51,113] (see Section 3.1).
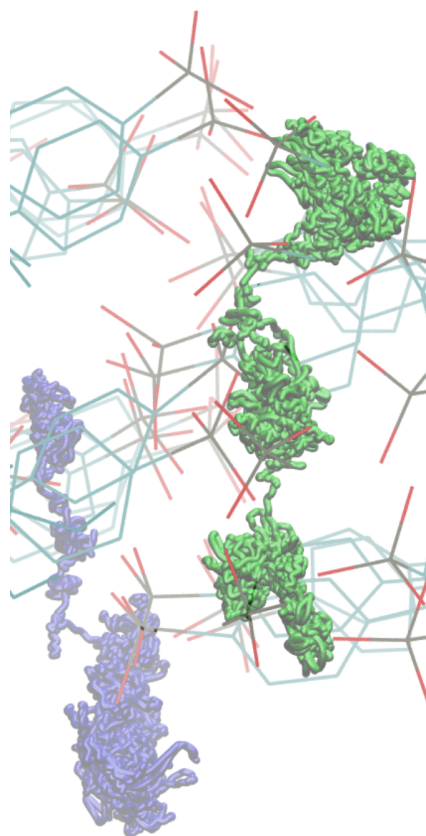
This final part of my thesis addresses an organic compound hexakis(p-phosphonatophenyl)benzene (p-6 PA-HPB), a disk-shaped, self-organizing material functionalized with phosponic acids, and also a promising candidate material for high-temperature and low-humidity membranes; the molecular structure is sketched in Figure 8 (left). In particular, I use large-scale atomistic molecular dynamics simulations on the level of density functional theory to identify the local packing motifs, the hydrogen bond network, and the proton diffusion.

The initial molecular superstructure for the *ab initio* MD is a representative fragment from a preliminary classical constant pressure MD simulation which, in turn, is based on 2D X-ray scattering experiments.[114,115] The classical equilibration yielded, in good agreement with the experimental results, a columnar arrangement on a hexagonal lattice with a dense but nonetheless very flexible hydrogen bond network between the phosphonic acid groups, see Figure 8. Note that the small tilt of the conjugated cores of the individual disks is a direct result of the equilibration molecular dynamics simulation.

The *ab initio* simulation showed a strong intermolecular hydrogen bond network: each phosphonic acid group is typically bonded to two of four possible groups from the two directly neigbouring stacks. An analysis of the hydrogen bond autocorrelation (see Equation (97) in Section 3.1) indicated two distinct components, a fast (200 fs) and a slow process (3–12 ps), in the dynamics of the hydrogen bond network which correspond to the reversible switching of a hydrogen bond between neighboring acceptor oxygens from different groups and the rotational motion of the phosphonic acids.

The most interesting observation in these simulations was the formation of quasi-one-dimension channels in the interstice between adjacent supramolecular stacks. The tracking of far traveling protons in the unbiased *ab initio* MD simulations showed that the diffusion is most pronounced in these channels; this situation is depicted for the trajectories of two protons in Figure 9 (blue and green).

Figure 9: Formation of quasi-one-dimensional nanochannels in p-6 PA-HPB: trajectories of far travelling protons along the columnar axis.

4 Conclusion

Ion conduction in condensed matter in general is a phenomenon with a multitude of facets. In this thesis, I have addressed several of these aspects with focus on proton conduction in fuel cell membranes. Fuel cells play an important role in the quest for clean and renewable energy. The technical development of efficiently operating fuel cells profits from the understanding of the conduction mechanism of the involved membrane material. For this aim, I have performed large-scale atomistic simulations to elucidate the proton conduction mechanism in hexakis(*p*-phosphonatophenyl)benzene (*p*-6 PA-HPB). This organic compound is a promising material for fuel cell membranes.

Hexakis(*p*-phosphonatophenyl)benzene is a disk-shaped molecule that is functionalized with phosphonic acids, and it tends to self-organize in supramolecular stacks in a hexagonal pattern. The computational modeling shows the formation of a dense and dynamically fluctuating intermolecular hydrogen bond network. Hydrogen bonds are one of the most common and fundamental driving forces for supramolecular structure formation. In *p*-6 PA-HPB, the hydrogen bond network connects the individual phosphonic acid groups and provides pathways for proton transfer events. The structural investigation of the computed supramolecular assembly yields that the typical phosphonic acid group is hydrogen-bonded to two of the four possible neighboring groups from adjacent stacks.

The strong point of the computational modeling lies in the atomistic resolution: the motion of individual protons in the dynamically fluctuating hydrogen bond network is directly observable. My simulations show that the hydrogen bond network forms quasi-one-dimensional channels in the interstice region between adjacent columnar stacks; the orientation of the channels is parallel to the columnar axis. Furthermore, the simulations show that the proton diffusion is most pronounced in these channels.

The computational modeling of proton conduction in *p*-6 PA-HPB is a case in point for large-scale atomistic simulations. The appropriate modeling of such large and complex chemical systems is a delicate and intricate task; the simulation under realistic environmental conditions is particularly challenging. The implementation of such large-scale simulations is supported by a range of suitable large-scale methods. The fusion of force fields with electronic structure methods is a particularly useful ansatz. The hybrid quantum-classical (QM/MM) method allows to model a small fragment of a large molecular system on the quantum level, while the remaining molecular environment is modeled on the classical level.

In the methodological part of this thesis, I have developed a numerical scheme to increase the accuracy of the QM/MM method. In detail, I use suitably optimized effective core potentials to solve the link atom problem that emerges during the QM/MM repartitioning at the quantum-classical boundary. In the design of these capping potentials, I consider especially the calculation of spectroscopic parameters from first-principles. Spectroscopic observables are a very important tool to probe and to characterize molecular structure with high precision. The evaluation of NMR chemical shifts and structural parameters shows that the optimized capping potentials outperform the commonly used hydrogen link atom approach.

A second methodological subproject addresses the numerical prediction of molecu-

lar structure, an evergreen problem in computational chemical physics but also a fundamental challenge. The determination of the global minimum structure is particularly difficult, despite the apparent simplicity of the task. For this aim, I have developed a stochastic, swarm intelligence-based algorithm to the global optimization of molecular geometry, and I have applied this algorithm to the optimization of molecular cluster structures with several highly relevant classical interaction potentials. The results show that this optimization algorithm is able to locate the global minimum on different potential energy surfaces.

5 Literature

[1] R. Feynman, *Phys. Rev.*, 1939, **56**, 340–343.

[2] J. N. Israelachvili, *Intermolecular and Surface Forces*, Academic Press, 3rd edn, 2011.

[3] J. E. Jones, *Proc. R. Soc. A-Math. Phys. Eng. Sci.*, 1924, **106**, 463–477.

[4] P. Morse, *Phys. Rev.*, 1929, **34**, 57–64.

[5] W. L. Jorgensen, J. Chandrasekhar, J. D. Madura, R. W. Impey and M. L. Klein, *J. Chem. Phys.*, 1983, **79**, 926–935.

[6] D. J. Wales and M. P. Hodges, *Chem. Phys. Lett.*, 1998, **286**, 65–72.

[7] M. W. Mahoney and W. L. Jorgensen, *J. Chem. Phys.*, 2000, **112**, 8910–8922.

[8] S. Habershon, T. E. Markland and D. E. Manolopoulos, *J. Chem. Phys.*, 2009, **131**, 024501.

[9] B. R. Brooks, R. E. Bruccoleri, B. D. Olafson, D. J. States, S. Swaminathan and M. Karplus, *J. Comp. Chem.*, 1983, **4**, 187–217.

[10] B. R. Brooks, C. L. Brooks, A. D. Mackerell, L. Nilsson, R. J. Petrella, B. Roux, Y. Won, G. Archontis, C. Bartels, S. Boresch, A. Caflisch, L. Caves, Q. Cui, A. R. Dinner, M. Feig, S. Fischer, J. Gao, M. Hodoscek, W. Im, K. Kuczera, T. Lazaridis, J. Ma, V. Ovchinnikov, E. Paci, R. W. Pastor, C. B. Post, J. Z. Pu, M. Schaefer, B. Tidor, R. M. Venable, H. L. Woodcock, X. Wu, W. Yang, D. M. York and M. Karplus, *J. Comp. Chem.*, 2009, **30**, 1545–1614.

[11] W. L. Jorgensen and J. Tirado-Rives, *J. Am. Chem. Soc.*, 1988, **110**, 1657–1666.

[12] W. D. Cornell, P. Cieplak, C. I. Bayly, I. R. Gould, K. M. Merz, D. M. Ferguson, D. C. Spellmeyer, T. Fox, J. W. Caldwell and P. A. Kollman, *J. Am. Chem. Soc.*, 1995, **117**, 5179–5197.

[13] Y. Duan, C. Wu, S. Chowdhury, M. C. Lee, G. Xiong, W. Zhang, R. Yang, P. Cieplak, R. Luo, T. Lee, J. Caldwell, J. Wang and P. Kollman, *J. Comp. Chem.*, 2003, **24**, 1999–2012.

[14] D. R. Hartree, *Math. Proc. Camb. Philos. Soc.*, 1928, **24**, 89–110.

[15] M. Born and R. Oppenheimer, *Ann. Phys.-Berlin*, 1927, **389**, 457–484.

[16] M. Born and V. Fock, *Z. Phys.*, 1928, **51**, 165–180.

[17] R. O. Jones and O. Gunnarsson, *Rev. Mod. Phys.*, 1989, **61**, 689–746.

[18] A. Szabo and N. S. Ostlund, *Modern Quantum Chemistry: Introduction to Advanced Electronic Structure Theory*, Courier Dover Publications, 1996.

[19] W. Ritz, *J. Reine Angew. Math.*, 1909, **1909**, 1–61.

[20] T. Koopmans, *Physica*, 1934, **1**, 104–113.

[21] J. Slater, *Phys. Rev.*, 1929, **34**, 1293–1322.

[22] V. Fock, *Z. Phys.*, 1930, **61**, 126–148.

[23] J. Slater, *Phys. Rev.*, 1930, **35**, 210–211.

[24] C. Roothaan, *Rev. Mod. Phys.*, 1951, **23**, 69–89.

[25] G. G. Hall, *Proc. R. Soc. A-Math. Phys. Eng. Sci.*, 1951, **205**, 541–552.

[26] R. M. Martin, *Electronic structure: basic theory and practical methods*, Cambridge

University Press, New York, 2010.

[27] P. Hohenberg and W. Kohn, *Phys. Rev.*, 1964, **136**, B864–B871.

[28] J. K. Percus, *Int. J. Quantum Chem.*, 1978, **13**, 89–124.

[29] M. Levy, *Proc. Natl. Acad. Sci. USA*, 1979, **76**, 6062–6065.

[30] W. Kohn and L. J. Sham, *Phys. Rev.*, 1965, **140**, A1133–A1138.

[31] A. D. Becke, *Phys. Rev. A*, 1988, **38**, 3098–3100.

[32] C. Lee, W. Yang and R. G. Parr, *Phys. Rev. B*, 1988, **37**, 785–789.

[33] D. Hamann, M. Schlüter and C. Chiang, *Phys. Rev. Lett.*, 1979, **43**, 1494–1497.

[34] S. Goedecker, M. Teter and J. Hutter, *Phys. Rev. B*, 1996, **54**, 1703–1710.

[35] C. Hartwigsen, S. Goedecker and J. Hutter, *Phys. Rev. B*, 1998, **58**, 3641–3662.

[36] J. VandeVondele and J. Hutter, *J. Chem. Phys.*, 2003, **118**, 4365–4369.

[37] J. Kolafa, *J. Comp. Chem.*, 2004, **25**, 335–342.

[38] M. Krack, *Theor. Chem. Acc.*, 2005, **114**, 145–152.

[39] J. VandeVondele, M. Krack, F. Mohamed, M. Parrinello, T. Chassaing and J. Hutter, *Comp. Phys. Commun.*, 2005, **167**, 103–128.

[40] G. Lippert, J. Hutter and M. Parrinello, *Mol. Phys.*, 1997, **92**, 477–487.

[41] M. E. Tuckerman, *Statistical Mechanics: Theory and Molecular Simulation*, Oxford University Press Inc., New York, 2010.

[42] L. Verlet, *Phys. Rev.*, 1967, **159**, 98–103.

[43] W. C. Swope, H. C. Andersen, P. H. Berens and K. R. Wilson, *J. Chem. Phys.*, 1982, **76**, 637–649.

[44] H. C. Andersen, *J. Chem. Phys.*, 1980, **72**, 2384–2393.

[45] H. J. C. Berendsen, J. P. M. Postma, W. F. van Gunsteren, A. DiNola and J. R. Haak, *J. Chem. Phys.*, 1984, **81**, 3684–3690.

[46] S. Nosé, *J. Chem. Phys.*, 1984, **81**, 511–519.

[47] W. Hoover, *Phys. Rev. A*, 1985, **31**, 1695–1697.

[48] G. Bussi, D. Donadio and M. Parrinello, *J. Chem. Phys.*, 2007, **126**, 014101.

[49] S. Grimme, *J. Comp. Chem.*, 2006, **27**, 1787–1799.

[50] J. Schmidt, A. Hoffmann, H. W. Spiess and D. Sebastiani, *J. Phys. Chem. B*, 2006, **110**, 23204–23210.

[51] G. A. Ludueña, T. D. Kühne and D. Sebastiani, *Chem. Mater.*, 2011, **23**, 1424–1429.

[52] H. M. Senn and W. Thiel, *Angew. Chem. Int. Ed. Engl.*, 2009, **48**, 1198–229.

[53] U. C. Singh and P. A. Kollman, *J. Comp. Chem.*, 1986, **7**, 718.

[54] R. R. Birge and C.-F. Zhang, *J. Chem. Phys.*, 1990, **92**, 7178–7195.

[55] X. Assfeld and J.-L. Rivail, *Chem. Phys. Lett.*, 1996, **263**, 100–106.

[56] C. R. Jacob and L. Visscher, *J. Chem. Phys.*, 2006, **125**, 194104.

[57] J. Gao, P. Amara, C. Alhambra and M. J. Field, *J. Phys. Chem. A*, 1998, **102**, 4714–4721.

[58] J. Pu, J. Gao and D. G. Truhlar, *J. Phys. Chem. A*, 2004, **108**, 632–650.

[59] J. Jung, C. H. Choi, Y. Sugita and S. Ten-no, *J. Chem. Phys.*, 2007, **127**, 204102.

[60] N. Jardilliera and A. Goursot, *Chem. Phys. Lett.*, 2008, **454**, 65–69.

[61] A. Mallik, D. E. Taylor, K. Runge and J. W. Dufty, *Int. J. Quantum Chem.*, 2004, **100**, 1019–1025.

[62] G. A. DiLabio, R. A. Wolkow and E. R. Johnson, *J. Chem. Phys.*, 2005, **122**, 44708.

[63] G. A. DiLabio, M. M. Hurley and P. A. Christiansen, *J. Chem. Phys.*, 2002, **116**, 9578–9584.

[64] C. Y. Xiao and Y. K. Zhang, *J. Chem. Phys.*, 2007, **127**, 124102.

[65] O. A. von Lilienfeld, I. Tavernelli, U. Röthlisberger and D. Sebastiani, *Phys. Rev. Lett.*, 2004, **93**, 153004(4).

[66] O. A. von Lilienfeld, I. Tavernelli, U. Röthlisberger and D. Sebastiani, *J. Chem. Phys.*, 2005, **122**, 14113.

[67] S. Komin and D. Sebastiani, *J. Chem. Theory Comput.*, 2009, **5**, 1490–1498.

[68] D. Karaboga and B. Basturk, *J. Glob. Optim.*, 2007, **39**, 459–471.

[69] D. Karaboga and B. Basturk, *Appl. Soft Comput.*, 2008, **8**, 687–697.

[70] D. Karaboga and B. Akay, *Appl. Math. Comput.*, 2009, **214**, 108–132.

[71] CPMD-3.13.2, *http://www.cpmd.org, Copyright IBM Corp 1990-2008 and MPI-FKF Stuttgart 1997-2008*, 2008.

[72] U. F. Röhrig, L. Guidoni, A. Laio, I. Frank and U. Röthlisberger, *J. Am. Chem. Soc.*, 2004, **126**, 15328–15329.

[73] U. F. Röhrig, L. Guidoni and U. Röthlisberger, *ChemPhysChem*, 2005, **6**, 1836–1847.

[74] J. A. Gascon, E. M. Sproviero, V. S. Batista and J. A. Gascón, *J. Chem. Theory Comput.*, 2005, **1**, 674–685.

[75] J. A. Gascon, E. M. Sproviero and V. S. Batista, *Acc. Chem. Res.*, 2006, **39**, 184–193.

[76] S. Sekharan, M. Sugihara and V. Buss, *Angew. Chem. Int. Ed. Engl.*, 2007, **46**, 269–271.

[77] U. F. Röhrig and D. Sebastiani, *J. Phys. Chem. B*, 2008, **112**, 1267–1274.

[78] H. Elgabarty, P. Schmieder and D. Sebastiani, *Chem. Sci.*, 2013, **4**, 755.

[79] R. Venkata Rao and P. J. Pawar, *Appl. Soft Comput.*, 2010, **10**, 445–456.

[80] I. M. S. de Oliveira and R. Schirru, *Ann. Nucl. Energy*, 2011, **38**, 1039–1045.

[81] S. Samanta and S. Chakraborty, *Eng. Appl. Artif. Intell.*, 2011, **24**, 946–957.

[82] M. Sonmez, *Appl. Soft Comput.*, 2011, **11**, 2406–2418.

[83] A. Singh, *Appl. Soft Comput.*, 2009, **9**, 625–631.

[84] S. Sundar and A. Singh, *Inf. Sci.*, 2010, **180**, 3182–3191.

[85] T.-J. Hsieh, H.-F. Hsiao and W.-C. Yeh, *Appl. Soft Comput.*, 2011, **11**, 2510–2525.

[86] R. Zhang and C. Wu, *Entropy*, 2011, **13**, 1708–1729.

[87] D. J. Wales and J. P. K. Doye, *J. Phys. Chem. A*, 1997, **101**, 5111–5116.

[88] J. P. K. Doye, D. J. Wales and M. A. Miller, *J. Chem. Phys.*, 1998, **109**, 8143.

[89] J. P. K. Doye, M. A. Miller and D. J. Wales, *J. Chem. Phys.*, 1999, **110**, 6896–6906.

[90] R. Leary and J. Doye, *Phys. Rev. E*, 1999, **60**, R6320–R6322.

[91] D. J. Wales and H. A. Scheraga, *Science*, 1999, **285**, 1368–1372.

[92] S. Goedecker, *J. Chem. Phys.*, 2004, **120**, 9911–9917.

[93] S. Goedecker, W. Hellmann and T. J. Lenosky, *Phys. Rev. Lett.*, 2005, **95**, 055501.

[94] S. Roy, S. Goedecker and V. Hellmann, *Phys. Rev. E*, 2008, **77**, 056707(5).

[95] K. Bao, S. Goedecker, K. Koga, F. Lançon and A. Neelov, *Phys. Rev. B*, 2009, **79**, 041405.

[96] S. E. Schönborn, S. Goedecker, S. Roy and A. R. Oganov, *J. Chem. Phys.*, 2009, **130**, 144108.

[97] S. Stepanenko and B. Engels, *J. Comp. Chem.*, 2007, **28**, 601–611.

[98] S. Stepanenko and B. Engels, *J. Comp. Chem.*, 2008, **29**, 768–780.

[99] S. Stepanenko and B. Engels, *J. Phys. Chem. A*, 2009, **113**, 11699–11705.

[100] C. Grebner, J. Becker, S. Stepanenko and B. Engels, *J. Comp. Chem.*, 2011, **32**, 2245–2253.

[101] D. M. Deaven and K. Ho, *Phys. Rev. Lett.*, 1995, **75**, 288–291.

[102] R. C. Glen and A. W. R. Payne, *J. Comput.-Aided Mol. Des.*, 1995, **9**, 181–202.

[103] G. Böhm, *Biophys. Chem.*, 1996, **59**, 1–32.

[104] C. Roberts, R. L. Johnston and N. T. Wilson, *Theor. Chem. Acc.*, 2000, **104**, 123–130.

[105] L. D. Lloyd, R. L. Johnston, C. Roberts and T. V. Mortimer-Jones, *ChemPhysChem*, 2002, **3**, 408–415.

[106] J.-O. Joswig and M. Springborg, *Phys. Rev. B*, 2003, **68**, 085408.

[107] M. Springborg, Y. Dong, V. G. Grigoryan, V. Tevekeliyska, D. Alamanova, E. Kasabova, S. Roy, J.-O. Joswig and A. M. Asaduzzaman, *Z. Phys. Chem.*, 2008, **222**, 387–405.

[108] V. A. Froltsov and K. Reuter, *Chem. Phys. Lett.*, 2009, **473**, 363–366.

[109] Z. E. Brain and M. A. Addicoat, *J. Chem. Phys.*, 2011, **135**, 174106.

[110] D. J. Wales, J. P. K. Doye, A. Dullweber, M. P. Hodges, F. Y. Naumkin, F. Calvo, J. Hernández-Rojas and T. F. Middleton, *The Cambridge Cluster Database, http://www-wales.ch.cam.ac.uk/CCD.html*, 2012.

[111] A. Kaltbeitzel, S. Schauff, H. Steininger, B. Bingöl, G. Brunklaus, W. H. Meyer and H. W. Spiess, *Solid State Ionics*, 2007, **178**, 469–474.

[112] H. Steininger, M. Schuster, K.-D. Kreuer, A. Kaltbeitzel, B. Bingöl, W. H. Meyer, S. Schauff, G. Brunklaus, J. Maier and H. W. Spiess, *Phys. Chem. Chem. Phys.*, 2007, **9**, 1764–1773.

[113] F. Jiang, A. Kaltbeitzel, B. Fassbender, G. Brunklaus, H. Pu, W. H. Meyer, H. W. Spiess and G. Wegner, *Macromol. Chem. Phys.*, 2008, **209**, 2494–2503.

[114] L. Jiménez-García, A. Kaltbeitzel, W. Pisula, J. S. Gutmann, M. Klapper and K. Müllen, *Angew. Chem. Int. Ed. Engl.*, 2009, **48**, 9951–9953.

[115] L. Jiménez-García, A. Kaltbeitzel, V. Enkelmann, J. S. Gutmann, M. Klapper and K. Müllen, *Adv. Funct. Mater.*, 2011, **21**, 2216–2224.

[116] C. Schiffmann and D. Sebastiani, *Phys. Status Solidi B*, 2012, **249**, 368–375.

[117] C. Schiffmann and D. Sebastiani, *J. Chem. Theory Comput.*, 2011, **7**, 1307–1315.

[118] A. C. Ihrig, C. Schiffmann and D. Sebastiani, *J. Chem. Phys.*, 2011, **135**, 214107.

[119] C. Wehmeyer, G. F. von Rudorff, S. Wolf, G. Kabbe, D. Schärf, T. D. Kühne and D. Sebastiani, *J. Chem. Phys.*, 2012, **137**, 194110.

[120] C. Wehmeyer, M. Schrader, D. Andrienko and D. Sebastiani, *J. Phys. Chem. C*, 2013, **117**, 12366–12372.

A Abstract/Kurzzusammenfassung

Abstract

The simulation of large and complex molecular systems is a very challenging task, especially under realistic conditions. A case in point is the phenomenon of proton conduction in fuel cell membranes which is the main topic addressed in this work. The computational modeling of this transport phenomenon is still far from being a routine problem, despite the fast development of computational infrastructure.

The general phenomenon of ion conduction in condensed matter consists of a multitude of facets. In this thesis, I address several aspects of this phenomenon for the specific case of the proton transport in hexakis(p-phosphonatophenyl)benzene, an organic compound that is a promising material for high-temperature fuel cell membranes.

I have performed large-scale atomistic simulations with electronic structure methods to elucidate the proton conduction mechanism in this material. The simulations show that this compound self-organizes in supramolecular columnar stacks with a tight intermolecular/interstack hydrogen bond network, which is in good agreement with experimental results. In particular, the simulations show the direct motion of individual protons in the dynamically fluctuating hydrogen bond network.

Interestingly, the hydrogen bond network forms quasi-one-dimensional channels in the interstice of adjacent supramolecular stacks and parallel to the columnar axis. The observed motion of the protons shows that the diffusion is most pronounced in these channels.

The applied part of my work is a case in point for large-scale simulations under realistic conditions. Such large-scale simulations, however, also require large-scale methods. The second and more methodologically oriented part of my thesis addresses the development of such large-scale methods, specifically, for quantum-classical calculations.

Hybrid quantum-classical (QM/MM) methods combine the ability of classical methods to treat large molecular systems with the advantage of quantum methods to model chemical processes within smaller fragments of the system. I have developed an approach to increase the accuracy of QM/MM calculations with a particular emphasis on spectroscopic parameters; this approach aims at extending the applicability of first-principles spectroscopy calculations to large-scale systems.

The second development subproject targets molecular structure prediction by means of numerical calculations. This is one of the evergreen problems in chemical physics but also one of the most difficult challenges. Specifically the determination of the global minimum structure is a field of intense research. For this aim, I have developed a stochastic, swarm intelligence-based optimization algorithm to the problem of global geometry optimization.

Kurzzusammenfassung

Die Simulation von großskaligen und komplexen molekularen Systemen ist eine große Herausforderung, insbesondere, wenn die Simulation unter realistischen Bedingungen durchgeführt werden soll. Das zentrale Thema dieser Dissertation ist die Protonenleitung in Brennstoffzellenmembranen und ein typisches Beispiel für solch eine Simulation. Die numerische Modellierung dieses Transportphänomens ist allerdings ausgesprochen aufwendig, trotz der rasanten Leistungsfähigkeitssteigerung modernen Computer.

Das allgemeine Phänomen der Ionenleitung in kondensierter Materie hat viele Facetten. Im Rahmen dieser Dissertation untersuche ich einige dieser Aspekte für den speziellen Fall von Protonenleitung in Hexakis(p-phosphonatophenyl)benzene, einer organischen Verbindung mit großem Potential für die Anwendung in Brennstoffzellenmembranen.

In meiner Arbeit habe ich großskalige, atomistische Simulationen auf Basis der Elektronenstrukturtheorie durchgeführt, um den Leitungsmechanismus in diesem Material zu untersuchen. Die Simulationen zeigen, dass sich dieses Material selbst in supramolekularen Stapeln anordnet und ein dichtes intermolekulares Netzwerk aus Wasserstoffbrücken ausbildet; diese Resultate stimmen gut mit experimentellen Beobachtungen überein. Inbesondere erlauben die Simulationen, die Bewegung der einzelnen Protonen im dynamisch fluktuierenden Wasserstoffbrückennetzwerk direkt zu beobachten.

Interessanterweise bildet das Wasserstoffbrückennetzwerk quasi-eindimensionale Kanäle im Zwischenraum benachbarter Stapel, die parallel zu den Stapelachsen angeordnet sind. Die Analyse der direkten Protonenbewegung zeigt, dass die Protonendiffusion innerhalb dieser Kanäle besonders ausgeprägt ist.

Dieses anwendungsorientierte Projekt meiner Arbeit ist ein typisches Beispiel für großskalige Simulationen unter realistischen Umgebungsbedingungen. Solch großskalige Simulationen stützen sich allerdings auch auf großskalige Simulationemethoden, deren Entwicklung den zweiten, methodisch orientierten Teil dieser Dissertation ausmachen:

Hybrid-quantenmechanisch/klassische (QM/MM) Simulationsmethoden erlauben es, die Vorteile klassischer und quantenmechanischer Methoden zu kombinieren. Dabei wird ein großskaliges System klassisch modelliert und nur ein Fragment auf Basis der Elektronenstrukturtheorie behandelt. Hierfür habe ich ein Verfahren zur Verbesserung der Genauigkeit dieser Methode entwickelt, die insbesondere die Qualität von spektroskopischen Berechnungen erhöht. Dieses Teilprojekt hat zum Ziel, die Anwendbarkeit von Spektroskopieberechnungen auf großskalige Systeme auzudehnen.

Das zweite Teilprojekt betrifft die Vorhersage molekularer Struktur mittels numerischer Rechnungen. Dies stellt eine der zentralen Fragestellungen im Feld der chemischen Physik dar und ist gleichzeitig eine der größten Herausforderungen. Insbesondere die Bestimmung des globalen Minimums ist ein vielbeachtetes Feld. Für dieses Problem habe ich einen stochastischen Algorithmus aus dem Feld der Schwarmintelligenz adaptiert und daraus einen globalen Optimierer für molekulare Geometrien entwickelt.

B Publications

Below is an explicit listing of the scientific publications that constitute this cumulative dissertation with detailed descriptions of the respective authors' contributions;* the reprints of these articles can be found on the following pages.

[P1] C. Schiffmann and D. Sebastiani:
Hydrogen bond networks: Structure and dynamics via first-principles spectroscopy;
Phys. Status Solidi B **249**, 368–375 (2012)

DOI: 10.1002/pssb.201100556
URL: http://doi.wiley.com/10.1002/pssb.201100556

In this feature article, I discuss the connection between first principles calculations and spectroscopic parameters for the determination of structure and dynamics of hydrogen bond networks. A specific feature of this work is the characterization of hydrogen bond network dynamics with auto-correlation techniques. This paper corresponds to Section 3.1 (page 31).

[P2] C. Schiffmann and D. Sebastiani:
Artificial Bee Colony Optimization of Capping Potentials for Hybrid Quantum Mechanical/Molecular Mechanical Calculations;
J. Chem. Theory Comput. **7**, 1307–1315 (2011)

DOI: 10.1021/ct1007108
URL: http://pubs.acs.org/doi/abs/10.1021/ct1007108

This research article represents my own work as a PhD student under supervision of my adviser D. Sebastiani on the optimization of capping potentials using the artificial bee colony algorithm. This paper corresponds to Section 3.2 (page 33).

[P3] A. C. Ihrig, C. Schiffmann, and D. Sebastiani:
Specific quantum mechanical/molecular mechanical capping-potentials for biomolecular functional groups;
J. Chem. Phys. **135**, 214107 (2011)

DOI: 10.1063/1.3664300
URL: http://link.aip.org/link/JCPSA6/v135/i21/p214107

For this research article, A. C. Ihrig was working as a Bachelor student under my supervision. We applied the approach from Ref. 117 to the optimization of capping potentials for specific biomolecular groups. This paper also belongs to Section 3.2 (page 33).

---

*Please note that the candidate's name changed from *Schiffmann* to *Wehmeyer* in April 2012; to emphasize, the candidate's name is underlined in the listing of the authors.

[P4] C. Wehmeyer, G. F. von Rudorff, S. Wolf, G. Kabbe, D. Schärf, T. D. Kühne, and D. Sebastiani:

Foraging on the potential energy surface: A swarm intelligence-based optimizer for molecular geometry;

J. Chem. Phys. **137**, 194110 (2012)

DOI: 10.1063/1.4766821
URL: http://link.aip.org/link/doi/10.1063/1.4766821

This research article represents my own work as a PhD student under supervision of my adviser D. Sebastiani on the optimization of molecular cluster structures using the artificial bee colony algorithm. G. F. von Rudorff, S. Wolf, and G. Kabbe worked as Bachlelor/Master students under my supervision and contributed to several aspects of the method development.
Our collaborators D. Schärf and T. D. Kühne (Johannes-Gutenberg Universität Mainz) are experts in the area of crystal structure determination and provided methodological improvements of the optimization scheme. This paper corresponds to Section 3.3 (page 35).

[P5] C. Wehmeyer, M. Schrader, D. Andrienko, and D. Sebastiani:

Water-Free Proton Conduction in Hexakis(p-Phosphonatophenyl)benzene Nanochannels;

J. Phys. Chem. C **117**, 12366–12372 (2013)

DOI: 10.1021/jp4035024
URL: http://pubs.acs.org/doi/abs/10.1021/jp4035024

In this collaboration, M. Schrader and D. Andrienko (Max-Planck-Institut für Polymerforschung, Mainz) contributed classical MD simulations of hexakis(p-phosphonatophenyl)benzene; I performed *ab initio* MD simulations of the proton transport mechanisms based on their superstructures. This paper corresponds to Section 3.4 (page 37).

Hydrogen bond networks: Structure and dynamics via first-principles spectroscopy

Feature Article

Christoph Schiffmann and Daniel Sebastiani*

Department of Physics, Dahlem Center for Complex Quantum Systems, Free University Berlin, Arnimallee 14, 14195 Berlin, Germany

* Corresponding author: e-mail daniel.sebastiani@fu-berlin.de, Phone: +49-30-83853037, Fax: +49-30-83851355

Different hydrogen bonding networks, same principle: hydrogen bonds are the most common fundamental structural driving forces, which determine structural and dynamical properties of numerous functional materials. First-principles calculations of spectroscopic parameters can help to understand local geometric motifs, but also more complex processes such as hydrogen bond lifetimes and ion transport processes in condensed phases. In this feature article, we review the relevance of structure–spectroscopy-relationships, we discuss recent *ab initio* calculations eludicating the structure of supramolecular assemblies, and highlight the importance of incorporating atomic and molecular mobility by means of molecular dynamics (MD) simulations.
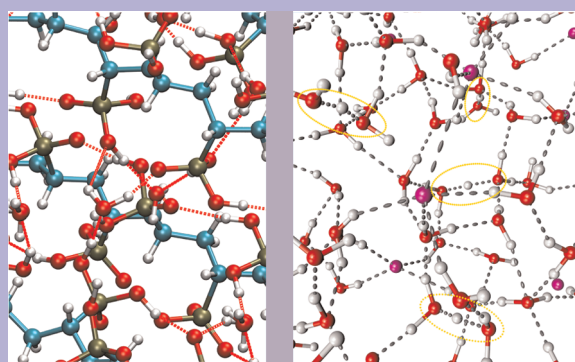
Complex hydrogen bonding networks: vinyl-phosphonic acid polymers (left) and aqueous hydrochloric acid (right).

1 Sensitivity of spectroscopic signatures to structure Any simulation of a molecular system is based on the computed potential energy surface (PES). This surface, however, is not directly experimentally accessible. One of the first actual observables in a numerical calculation is the atomic structure, be it at equilibrium or as an ensemble average. As a consequence, approximations and errors in the calculation of the PES propagate immediately to structural parameters. Even a highly corrugated landscape is full of local energy minima, at which the atomic forces vanish; hence, the PES is locally quadratic in all coordinates at those points. This in turn results in a strong effect of small perturbative forces on computed geometries near equilibrium.

It turns out that many spectroscopic observables exhibit a very different behavior close to the equilibrium geometry: small structural variations can lead to considerable changes in (experimental as well as computed) spectra. As an example from nuclear magnetic resonance spectroscopy (NMR), the ^{1}H NMR chemical shift calculated for the H-bonding proton in an imidazole dimer is shown in Fig. 1 (top). The slope of δ^H at equilibrium (indicated by the dashed line) is about 8 ppm/Å; assuming a conservative estimate for the theoretical/experimental resolution of 0.1 ppm, this corresponds to a spectroscopic distance resolution of almost 0.01 Å [1]. In comparison to this, the energetic resolution of a standard *ab initio* calculation (assuming a systematic error of 1 kcal/mol and a typical H-bond strength) is roughly 0.1 Å. It is not feasible to reliably compute the energy differences due to small geometric changes more accurately than this, except by means of very resource-intensive quantum-chemical reference methods. Hence, the variation of the NMR chemical shift considerably magnifies alterations of
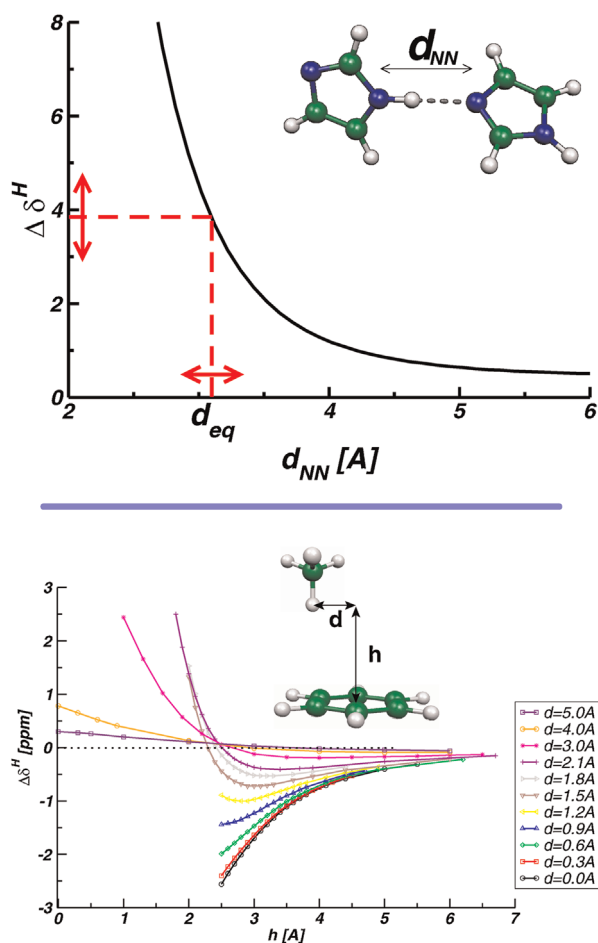
Phys. Status Solidi B **249**, No. 2 (2012)

369

Feature

Article

Figure 1 (online color at: www.pss-b.com) Top: The dependence of ^{1}H NMR chemical shift on the hydrogen bond geometry (here: on the inter-nitrogen distance d_{NN}) of a hydrogen-bonded imidazole dimer. Bottom: The dependence of the ^{1}H NMR chemical shift of a methane proton on the molecular position (here: lateral and vertical distances d and h) relative to a benzene molecule.

the underlying geometry. An even stronger amplification can be observed for weak van-der-Waals-complexes such as the methane–benzene dimer (shown in Fig. 1, bottom). Here, the relative orientation of a methane molecule to a neighboring benzene leads to significant changes in the ^{1}H NMR chemical shifts.

When performing calculations of spectroscopic observables within density functional theory (DFT), the question arises how much the computed observables depend on the computational setup, e.g., on the choice of the basis set, xc-functional, and other computational parameters. Calculations of ^{1}H NMR chemical shifts in liquid water (under full periodic boundary conditions) reveal only a small direct impact of the chosen functional on the computed shifts. However, a more important indirect effect is observed via the dependence of the underlying molecular dynamics (MD) trajectories on the xc-functional and the accuracy of the effective core potential [2].

This illustrates the high sensitivity of spectroscopic parameters to molecular structure, combined with a strong robustness towards the computational setup – provided that the underlying structural data is generated with adequate rigor. In particular, this includes the accurate inclusion of non-covalent interactions within the PES. The most prominent example of such non-covalent effects are hydrogen bonds; however, also van-der-Waals interactions play an important role in the process of structure formation for supramolecular systems [3, 4]. Unfortunately, the energetics of this type of molecular interaction is not efficiently described by mean-field theories such as DFT [5–13]. Specifically in the case of liquid water, constant-pressure first-principles MD simulations at the level of DFT yield a density considerably below the experimental one, combined with a tendency to overstructure the liquid. In turn, the semiemperical incorporation of the van der Waals interaction leads to the correct density of this complex fluid [14], which is very important for the accurate description of compound systems with internal interfaces [6, 8, 9, 15, 16].

Another physical phenomenon that is difficult to model accurately is the quantum nature of light nuclei (in particular protons). The classical treatment of nuclei (as point charges) is the standard approach within the framework of DFT and usually sufficient for many applications; however, it does not take into account any nuclear quantum effects. A case in point are hydrogen/deuterium isotope effects, which often leave a characteristic fingerprint in spectroscopic observables such as NMR chemical shifts [17]. The effect can be observed experimentally and has recently attracted interest in both the fields of materials science [18–20] and biophysical chemistry [21–23].

Several techniques are known to incorporate the quantum nature of nuclei within first-principles calculations, in particular the path integral approach. It relies on the isomorphism between the quantum description of a system and the corresponding statistical ensemble of coupled classical systems [24–30]; its application to liquid water and ice revealed a distinctive impact of the protons' quantum behavior on structure and dynamics of the underlying HBN [31–36]. An upcoming alternative description of quantum effects is the use of thermostats which mimic the increased delocalization of the quantum particle via random forces; this technique is known as a colored-noise-thermostat [37–41].

2 Complex hydrogen bond networks in condensed phases Many condensed-phase systems (both solids and liquids) exhibit a strong hydrogen bond network (HBN), which contributes significantly to the structural driving forces responsible for supramolecular packing. In solids, this packing structure is static, which leads to very pronounced signatures in spectroscopic parameters.

A particular example are "bulk" NMR chemical shifts, which describe the change in an NMR resonance of a molecule due to crystallization. First-principles calculations

of bulk NMR chemical shifts can identify accurately the individual spectroscopic signatures of packing effects. This effect was systematically studied recently for a representative set of amino acids [42]; their characteristic hydrogen bonding patterns in the condensed phase are illustrated in Fig. 2 [42].

Matters complicate for systems which exhibit a greater deal of disorder and a distribution of conformations rather than a homogeneous morphology, such as polymers. Naturally, a first-principles approach cannot take into account the total structural complexity of a polymer, i.e., loops and density variations. However, on local length-scales, the microscopic picture of polymer conformations can be represented surprisingly accurately.

In this context, proton conducting polymers have recently attracted increasing interest in view of potential applications in fuel cells [46–51]. A combined study of NMR MAS experiments and numerical simulations on poly[vinyl

Figure 3 (online color at: www.pss-b.com) Poly-vinyl-phosphonic acid (PVPA) and its local hydrogen bonding network [44, 45]. There are both inter- and intra-chain hydrogen bonds between phosphonic acid groups, as well as intercalated water molecules which can bridge small interstitial gaps of the network.

phosphonic acid] (PVPA, see Fig. 3), which is a promising candidate from the aforementioned field, revealed the correlation between spectra and morphological details, in particular chemical defects within the polymer. It could be shown that the so-called "condensation defects," which tend to be traps for H^+ conduction, have a unique ^{31}P NMR signal that allows a quantitative estimate of their density [52]. In addition, the computed distribution of hydrogen bond orientations could be compared against experiment by means of variable-temperature NMR spectroscopy [45].

Turning to the field of liquids, the question of ion solvation and its structural consequences for the aqueous HBN persists. A case in point are acidic solutions, for instance hydrochloric acid, HCl(aq). A snapshot from a Car–Parrinello MD simulation of this acid is shown in Fig. 4. The first-principles calculation of NMR chemical shifts reveals that the hydrogen bonding strength is modified only little in the vicinity of the Cl^- anions. In contrast to this, the solvated protons have a dramatic effect on the NMR chemical shifts [53].

In such complex liquids, the interaction strength between cations and anions in protic and aprotic ionic liquids can be related to low frequency vibrational bands, which, in turn, can be measured by far FTIR spectroscopy. Hybrid functional calculations within the framework of DFT show that these interactions are described by characteristic ratios between Coulomb forces and hydrogen bonds [56].

In complex disordered systems, it is often interesting to probe the specific chemical environment of a given functional group or a molecular fragment. In this case, electron spin resonance (ESR or EPR) is a viable alternative to NMR spectroscopy. While NMR probes all nuclei of a given type on equal footing, electron paramagnetic resonance (EPR) probes the spin of an unpaired electron. Thus, EPR requires the presence of a radical, but, as a consequence

Figure 2 (online color at: www.pss-b.com) A set of amino acids (top to bottom: histidine, alanine/adenine, tyrosine) with their characteristic hydrogen bonding motifs. The ^1H MAS NMR spectra on the top show the corresponding bulk NMR chemical shifts (bottom: isolated, center: computed crystal, top: experimental). The bottom right plot shows the nucleus independent chemical shift map [43] of tyrosine.
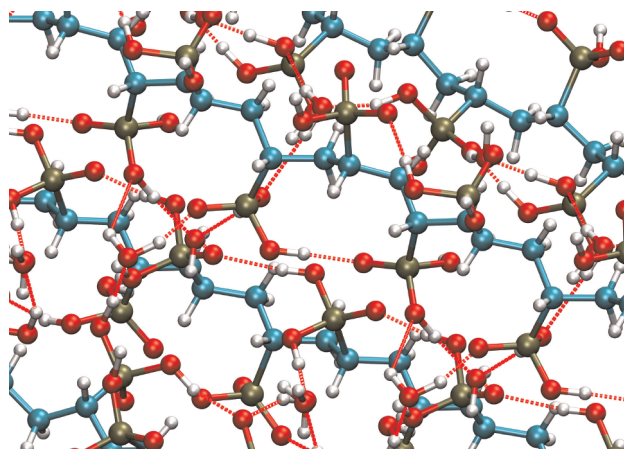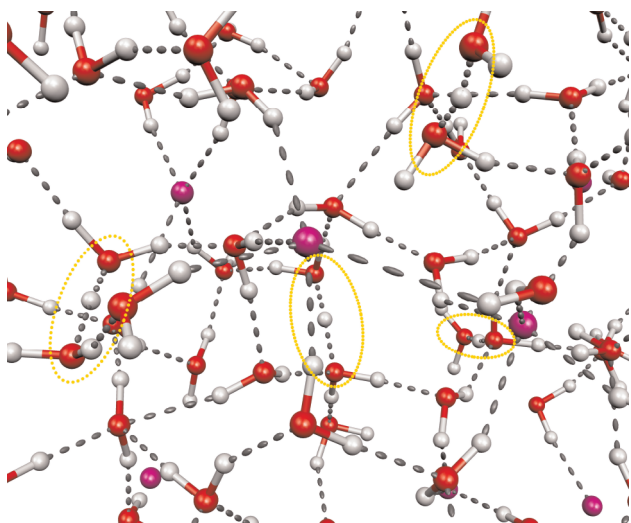
Phys. Status Solidi B **249**, No. 2 (2012)

Feature
Article

371

Figure 4 (online color at: www.pss-b.com) Aqueous solution of HCl [53, 54], with Cl⁻ ions (pink color) and solvated protons (hydronium and Zundel ions, marked in yellow). Hydrogen bonds, defined via a purely geometric criterion [55] (dotted lines), are also sketched for illustration.

of the hyperfine coupling between the unpaired spin with surrounding nuclear spins, EPR probes the very local chemical environment around the radical. A spin probe which is commonly used as counterion for polyelectrolytes is the paramagnetic nitrosodisulfonate anion $ON(SO_3)_2$, also known as Fremy's salt. When placed in a water–methanol mixture, combined classical and first principles modeling reveals that the hydrogen bonding pattern is surprisingly selective: the sulfonate groups are almost exclusivly solvated by water molecules, while the nitroxy group is dominantly surrounded by methanol. This selective hydrogen bonding situation is confirmed by theoretical as well as experimental EPR spectroscopy [57].

One of the intrinsic limitations of first-principles MD simulations is the restricted size of the simulation box. While this finite-size problem is known to have only very little influence on structural properties of liquid water, it was recently shown in a large-scale Car–Parrinello MD simulation that dynamical aspects are influenced in a considerably stronger manner [58, 59]. With present-day numerical resources, it is not possible to converge first-principles simulations in the system size dimension; only extrapolation schemes are able to reach the limit of effectively infinite systems. A potential route out of this dilemma are multi-scale simulation methods, in particular if a smooth transition of particles between the simulation levels is implemented. A recent development in this field are adaptive multi-scale methods [60]. Presently, they cover only force-field based calculations, but there exists an interesting prospect of an extension towards *ab initio* methods.

When it comes to modeling surfaces and interfaces, numerous studies deal with hard surfaces with individual adsorbing water molecules [61, 62] and with extended mono-

or multilayers of adsorbed water [63–68]. In contrast to such hard confinements, the interface between liquid water and vacuum (or water vapor) is very soft. This geometric flexibility makes a straightforward simulation more challenging, and only a few very recent projects aim at a consistent first-principles simulation of structural features of these water–vapor interfaces [69]. Nevertheless, this very challenging new field represents a rich area with very promising physical and chemical questions to address. The first results indicate that the structure of water at this interface tends to that of bulk liquid water within less than four monolayers [70].

3 Picosecond dynamics of hydrogen bond networks While the determination of structural features at the molecular and supramolecular level is of paramount importance for many areas in physics and chemistry, it represents only "half" the actual reality. At least of equal importance are dynamical characteristics of molecular processes, since dynamical aspects (kinetics) determine whether a given structure is actually accessible for a system or not. Hence, the first-principles based simulation of MD has emerged as one of the striking justifications for the utility of computational approaches to physics and chemistry. Again, the combination with computational spectroscopy creates a bridge towards real systems, which are characterized by spectroscopic experiments.

One of the most common spectroscopic parameters from atomistic MD simulations are molecular and supramolecular vibrations, which lead to changes in molecular dipoles and thus to the absorption of light. The frequency of these vibrations is located in the infrared domain, i.e., from about 100 up to $3500 \, cm^{-1}$. The exact frequency of a given vibrational mode depends strongly on the chemical environment. A case in point are hydrogen bonds, which tend to make the vibrational energy curve more anharmonic and thus result in a red-shift of the absorption mode. In this way, the HBN structure and its fluctuations are coupled to direct observables.

A prominent example is the tetrahedral HBN of liquid water and ice. It yields distinct peaks in the far IR spectrum, in which a particular anisotropic translational peak (at $200 \, cm^{-1}$) has recently gained specific interest. This peak had turned out to be difficult to interpret in earlier studies, both experimentally and computationally [71]; recently, it could be shown that it reflects a coupling of a given water molecule to its tetrahedral solvation cage [72–74].

The IR spectrum represents the oscillations of chemical bonds, to which hydrogen bonds have an influence via the anharmonicity that they induce. In turn, a direct measure of the dynamics of the HBN is possible by looking at nuclear spin relaxation processes, in particular the spin-lattice relaxation time T_1. For nuclear spins with $I \geq 1$, this relaxation dynamics is mainly determined by nuclear quadrupole interactions to the electric field gradient which is experienced by the spin. The latter is readily (and accurately) available in a first-principles MD simulation,
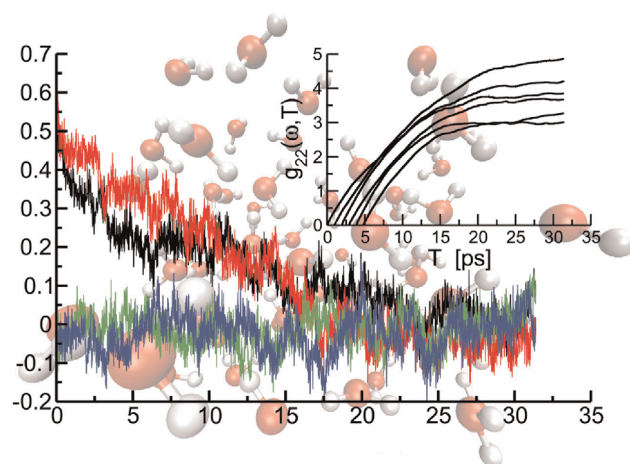
Figure 5 (online color at: www.pss-b.com) Decay of the dominant components of the electric field gradient autocorrelation function of ^{17}O in liquid water (red/black: real parts; green/blue: imaginary parts) [75]. The inlet shows the corresponding spectral densities for different starting points in the trajectory.

and the resulting NMR relaxation times for deuterated liquid water have been found to be in good agreement with experimental values [75]. It could also be shown that the correlation functions, which are relevant for this spin-lattice relaxation, decay smoothly within less than 30 ps (see Fig. 5), which corresponds well to the timescales accessible to *ab initio* MD simulations.

This result was obtained for pure water, but it encourages the interpretation of more complex aqueous environments [59, 61–63, 67, 70]. It should be noted, that similarly good results have been obtained earlier based on force-field MD simulations of binary mixtures [76].

A challenging extension of the computational spectroscopic characterization of HBNs is the application to structurally more complex systems. A first step is the MD simulations of HBNs around amino acids in dilute aqueous solution. In this kind of systems, it could be shown that hydrophilic hydrogen bond donors slow down the time scale of fluctuations in the HBN [77].

The internal dynamics of HBNs is also crucial for functional polymers such as the proton conducting PVPA (see Fig. 3) that has already been mentioned above. In this system, the phosphonic acid groups are spatially fixed to the polymer backbone, which reduces the flexibility of the topology of the HBN. In order to analyze the intrinsic timescales of the hydrogen bonds, we can define a HBN correlation function $\eta(t)$ via:

$$\eta(t) = \left\langle \sum_k \tilde{\delta}_{H_k(t+t_0), H_k(t_0)} \right\rangle_{t_0}, \qquad (1)$$

where $\tilde{\delta}_{H_k(t+t_0), H_k(t_0)} = 1$ if the acidic proton k is at both times hydrogen-bonded to the same oxygen, and 0 otherwise [44]. Hence, $\eta(t)$ is the average number of H-bonds of the
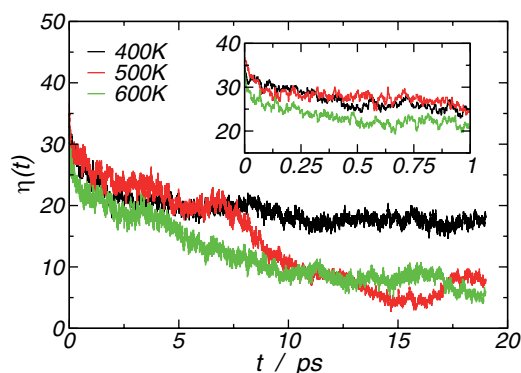

Figure 6 (online color at: www.pss-b.com) The hydrogen bond correlation function $\eta(t)$ according to Eq. (1) characterizes the evolution of the local hydrogen bond network. Here, $\eta(t)$ is depicted for wet PVPA [44, 45] at different temperatures. The initial decay during the first picosecond is magnified in the inset.

original network (at time t_0) that are still conserved after a simulation time t.

Figure 6 shows the hydrogen bond correlation $\eta(t)$ for a specific PVPA model at different temperatures. While the decay is clearly faster at higher temperatures, there is no qualitative difference within the range of $T = 400–600$ K. In all cases, a plateau is reached after 10–20 ps, which illustrates the very special character of the HBN due to the confinement created by the polymer superstructure [44].

4 Methodological improvements in hybrid quantum–classical (QM/MM) schemes In the previous sections, we have illustrated the high range of applicability of large-scale *ab initio* MD simulations and computational spectroscopy. Unfortunately, there are limits both in simulation time and in system size; the latter is typically reached at about 500–1000 independent atoms in a unit cell. Biochemical macromolecules, however, cross this boundary easily and thus cannot be treated fully on the level of DFT. Instead, one has to restrict the quantum mechanical modeling to specific subunits and cover the remaining part with conventional molecular modeling methods (hybrid QM/MM) [78–80]. The field of mixed QM/MM simulations is very large and merits a review of its own; several good overview papers can be found in literature [81–88].

Besides the accuracy of the respective QM and MM approaches, the quality of a QM/MM calculation depends in particular on the realization of the quantum-classical interface. Each covalent bond that crosses this boundary is cleaved and has to be saturated on the quantum side. Several techniques are known for this purpose; the most common are hydrogen atoms, frozen orbitals [89], generalized hybrid orbitals [90], or suitably optimized capping potentials [91, 92]. The quality of the saturation determines the strength and reach of the bond-cleavage-induced perturbation of the electronic structure inside the QM region.

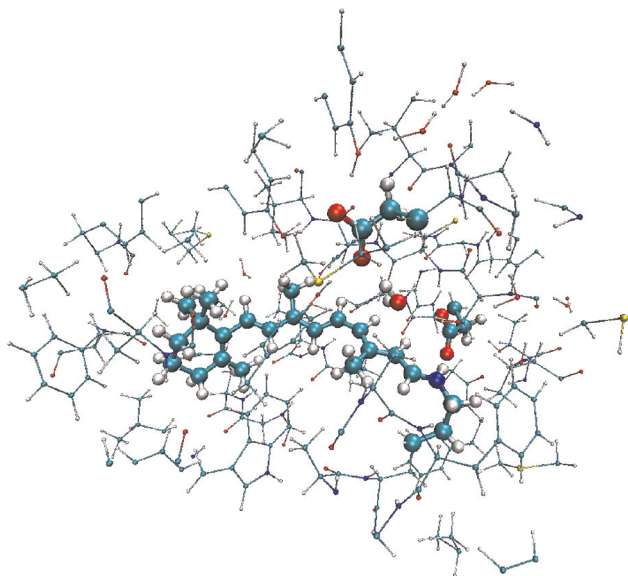The termination of the QM region is particularly important for spectroscopic calculations, which are

Phys. Status Solidi B **249**, No. 2 (2012)

373

Feature
Article

Figure 7 (online color at: www.pss-b.com) The chromophore of bacteriorhodopsin with its immediate environment (the binding pocket). A typical hybrid QM/MM setup consists in treating the chromophore and several of the glutamate bases by quantum methods, and the rest of the protein with force fields [93].

extremely sensitive to changes in the electronic structure. Furthermore, there are often charged functional groups close to the QM/MM transition that have to be treated with even more care [23, 93–97]. A case in point is the rhodopsin protein (see Fig. 7), which has several aspartate and glutamate bases in the direct vicinity of its chromophore which are known to influence the absorption wavelength. The photoisomerization initiates a chain of complex reorientation processes in the protein, which eventually lead to the release of a proton at the outer hull. The specific protonation state of the acidic groups in the direct environment of the chromophore are still a matter of debate; recent results from computational spectroscopy have illustrated the importance of a more accurate modeling [98].

To increase the level of accuracy in QM/MM calculations, we have recently developed a numerical scheme for optimization of analytical capping potentials. We characterize the bond-cleavage-induced perturbations by means of a suitable penalty functional and minimize these perturbations by varying the shape of this potential using an optimization algorithm based on swarm intelligence. This approach provided a capping potential for homoatomic C–C bond cleavage situations with considerably improved spectroscopic results, compared to the common hydrogen capping; and although the accuracy that can be achieved with capping potentials does not reach that of frozen density embedding schemes, the central advantage of the capping potential approach lies in its simplicity [92].

5 Conclusion This set of examples summarized in this article demostrates the predictive quality of computational

spectroscopy in combination with large-scale first-principle MD simulations for the quantitative characterization of complex HBNs in supramolecular assemblies.

References

[1] M. Schulz-Dobrick, T. Metzroth, H. W. Spiess, J. Gauss, and I. Schnell, Chem. Phys. Chem. **6**, 315–327 (2005).
[2] D. Banyai, T. Murakhtina, and D. Sebastiani, Magn. Reson. Chem. **48**, S56–S60 (2010).
[3] M. R. Hansen, S. Sekharan, R. Graf, and D. Sebastiani, J. Am. Chem. Soc. **131**, 5251–5256 (2009).
[4] J. M. Lehn, Rep. Prog. Phys. **67**, 249–265 (2004).
[5] B. I. Lundqvist, Y. Andersson, H. Shao, S. Chan, and D. C. Langreth, Int. J. Quantum Chem. **56**, 247–255 (1995).
[6] S. D. Chakarova and E. Schröder, J. Chem. Phys. **122**, 054102 (2005).
[7] D. C. Langreth, M. Dion, H. Rydberg, E. Schröder, P. Hyldgaard, and B. I. Lundqvist, Int. J. Quantum Chem. **101**, 599–610 (2005).
[8] Y. Zhao, O. Tishchenko, and D. Truhlar, J. Phys. Chem. B **109**, 19046–19051 (2005).
[9] Y. Zhao and D. Truhlar, J. Phys. Chem. A **109**, 5656–5667 (2005).
[10] E. Johnson, R. Wolkow, and G. DiLabio, Chem. Phys. Lett. **394**, 334–338 (2004).
[11] O. A. von Lilienfeld, I. Tavernelli, U. Rothlisberger, and D. Sebastiani, Phys. Rev. Lett. **93**, 153004 (2004).
[12] S. Grimme, J. Comput. Chem. **27**(15), 1787–1799 (2006).
[13] Y. Zhao and D. G. Truhlar, J. Chem. Theory Comput. **1**, 415–432 (2005).
[14] J. Schmidt, J. VandeVondele, I. F. Kuo, D. Sebastiani, J. Siepmann, J. Hutter, and C. J. Mundy, J. Phys. Chem. B **113**, 11959–11964 (2009).
[15] J. C. Rasaiah, S. Garde, and G. Hummer, Annu. Rev. Phys. Chem. **59**, 713–740 (2008).
[16] M. Vogel, Eur. Phys. J. Spec. Top. **189**, 47–64 (2010).
[17] M. D. Fenn and E. Spinner, J. Phys. Chem. **88**, 3993–3997 (1984).
[18] P. M. Tolstoy, P. Schah-Mohammedi, S. N. Smirnov, N. S. Golubev, G. S. Denisov, and H. H. Limbach, J. Am. Chem. Soc. **126**, 5621–5634 (2004).
[19] S. Sharif, G. Denisov, M. Toney, and H. Limbach, J. Am. Chem. Soc. **128**, 3375–3387 (2006).
[20] V. Srinivasan and D. Sebastiani, J. Phys. Chem. C **115**, 12631–12635 (2011).
[21] S. Presse and R. Silbey, J. Chem. Phys. **124**, 164504 (2006).
[22] J. H. Scott, D. M. O'Brien, D. Emerson, H. Sun, G. D. McDonald, A. Salgado, and M. L. Fogel, Astrobiology **6**, 867–880 (2006).
[23] P. Vidossich, S. Piana, A. Miani, and P. Carloni, J. Am. Chem. Soc. **128**, 7215–7221 (2006).
[24] D. Ceperley, Rev. Mod. Phys. **67**, 279–355 (1995).
[25] M. Sprik, M. L. Klein, and D. Chandler, Phys. Rev. B **31**, 4234–4244 (1985).
[26] G. A. Voth, Adv. Chem. Phys. **93**, 135–218 (1996).

[27] M. Tuckerman, D. Marx, M. Klein, and M. Parrinello, J. Chem. Phys. **104**, 5579–5588 (1996).

[28] J. Morrone, V. Srinivasan, D. Sebastiani, and R. Car, J. Chem. Phys. **126**, 234504 (2007).

[29] L. Lin, J. A. Morrone, R. Car, and M. Parrinello, Phys. Rev. Lett. **105**(11), 110602 (2010).

[30] S. L. Raugei and M. L. Klein, Chem. Phys. Chem. **5**, 1569–1576 (2004).

[31] M. Tuckerman, D. Marx, M. L. Klein, and M. Parrinello, Science **275**, 817–820 (1997).

[32] J. A. Morrone and R. Car, Phys. Rev. Lett. **101**, 017801 (2008).

[33] J. A. Morrone, L. Lin, and R. Car, J. Chem. Phys. **130**(20), 204511 (2009).

[34] L. Lin, J. A. Morrone, R. Car, and M. Parrinello, Phys. Rev. B **83**(22), 220302 (2011).

[35] T. D. Hone, P. J. Rossky, and G. A. Voth, J. Chem. Phys. **124**, 154103 (2006).

[36] F. Paesani, W. Zhang, D. A. Case, T. E. Cheatham, and G. A. Voth, J. Chem. Phys. **125**, 184507 (2006).

[37] M. Ceriotti, G. Bussi, and M. Parrinello, Phys. Rev. Lett. **102**, 020601 (2009).

[38] M. Ceriotti, G. Bussi, and M. Parrinello, Phys. Rev. Lett. **103**, 030603 (2009).

[39] M. Ceriotti, M. Parrinello, T. E. Markland, and D. E. Manolopoulos, J. Chem. Phys. **133**, 124104 (2010).

[40] M. Ceriotti, G. Bussi, and M. Parrinello, J. Chem. Theory Comput. **6**, 1170–1180 (2010).

[41] M. Ceriotti, G. Miceli, A. Pietropaolo, D. Colognesi, A. Nale, M. Catti, M. Bernasconi, and M. Parrinello, Phys. Rev. B **82**(17), 174306 (2010).

[42] J. Schmidt, A. Hoffmann, H. W. Spiess, and D. Sebastiani, J. Phys. Chem. B **110**, 23204–23210 (2006).

[43] D. Sebastiani, Chem. Phys. Chem. **7**, 164–175 (2006).

[44] G. A. Ludueña, T. D. Kühne, and D. Sebastiani, Chem. Mater. **23**, 1424–1429 (2011).

[45] Y. J. Lee, T. Murakhtina, D. Sebastiani, and H. Spiess, J. Am. Chem. Soc. **129**, 12406–12407 (2007).

[46] F. Jiang, A. Kaltbeitzel, B. Fassbender, G. Brunklaus, H. Pu, W. H. Meyer, H. W. Spiess, and G. Wegner, Macromol. Chem. Phys. **209**, 2494–2503 (2008).

[47] Z. Jiang, X. Zheng, H. Wu, and F. Pan, J. Power Sources **185**, 85–94 (2008).

[48] F. Pan, H. Jia, Z. Jiang, and X. Zheng, J. Membr. Sci. **325**, 727–734 (2008).

[49] A. Aslan and A. Bozkurt, J. Power Sources **191**, 442–447 (2009).

[50] A. Aslan, S. U. Celik, and A. Bozkurt, Solid State Ion. **180**, 1240–1245 (2009).

[51] R. Perrin, M. Elomaa, and P. Jannasch, Macromolecules **42**, 5146–5154 (2009).

[52] Y. J. Lee, B. Bingöl, T. Murakhtina, D. Sebastiani, W. Meyer, G. Wegner, and H. Spiess, J. Phys. Chem. B **111**, 9711–9721 (2007).

[53] T. Murakhtina, J. Heuft, J. E. Meijer, and D. Sebastiani, Chem. Phys. Chem. **7**, 2578–2584 (2006).

[54] J. M. Heuft and E. J. Meijer, Phys. Chem. Chem. Phys. **8**, 3116–3123 (2006).

[55] R. Kumar, J. R. Schmidt, and J. L. Skinner, J. Chem. Phys. **126**, 204107 (2007).

[56] K. Fumino, A. Wulf, and R. Ludwig, Phys. Chem. Chem. Phys. **11**(39), 8790–8794 (2009).

[57] J. Heller, H. Elgabarty, B. Zhuang, D. Sebastiani, and D. Hinderberger, J. Phys. Chem. B **114**, 7429–7438 (2010).

[58] T. D. Kühne, M. Krack, F. Mohamed, and M. Parrinello, Phys. Rev. Lett. **6**(98), 066401 (2007).

[59] T. D. Kühne, M. Krack, and M. Parrinello, J. Chem. Theory Comput. **5**, 235–241 (2009).

[60] S. Matysiak, C. Clementi, M. Praprotnik, K. Kremer, and L. D. Site, J. Chem. Phys. **128**, 024503 (2008).

[61] T. Murakhtina, L. Delle Site, and D. Sebastiani, Chem. Phys. Chem. **7**, 1215–1219 (2006).

[62] D. Sebastiani and L. Delle Site, J. Chem. Theory Comput. **1**, 78–82 (2005).

[63] M. L. Grecea, E. H. G. Backus, B. Riedmüller, A. Eichler, A. W. Kleyn, and M. Bonn, J. Phys. Chem. B **108**, 12575–12582 (2004).

[64] S. Meng, L. F. Xu, E. G. Wang, and S. Gao, Phys. Rev. Lett. **89**, 176104 (2002).

[65] D. Menzel, Science **295**, 58–59 (2002).

[66] A. Michaelides, A. Alavi, and D. A. King, Phys. Rev. B **69**, 113404 (2004).

[67] A. Michaelides, V. A. Ranea, P. L. de Andres, and D. A. King, Phys. Rev. Lett. **90**, 216102 (2003).

[68] V. Termath, F. Haase, J. Sauer, J. Hutter, and M. Parrinello, J. Am. Chem. Soc. **120**, 8512–8516 (1998).

[69] I. F. W. Kuo and C. J. Mundy, Science **303**, 658–660 (2004).

[70] T. D. Kühne, T. A. Pascal, E. Kaxiras, and Y. Jung, J. Phys. Chem. Lett. **2**(2), 105–113 (2011).

[71] K. Laasonen, M. Sprik, M. Parrinello, and R. Car, J. Chem. Phys. **99**, 9080–9089 (1993).

[72] R. Iftimie and M. E. Tuckerman, J. Chem. Phys. **122**, 214508 (2005).

[73] M. Sharma, R. Resta, and R. Car, Phys. Rev. Lett. **95**, 187401 (2005).

[74] H. J. Bakker and J. L. Skinner, Chem. Rev. **110**, 1498–1517 (2010).

[75] J. Schmidt, J. Hutter, H. W. Spiess, and D. Sebastiani, Chem. Phys. Chem. **9**, 2313–2316 (2008).

[76] B. Kirchner, D. J. Searles, A. J. Dyson, P. S. Vogt, and H. Huber, J. Am. Chem. Soc. **122**, 5379–5383 (2000).

[77] D. Laage, G. Stirnemann, and J. T. Hynes, J. Phys. Chem. B **113**(8), 2428–2435 (2009).

[78] M. J. Field, P. A. Bash, and M. Karplus, J. Comput. Chem. **11**, 700–733 (1990).

[79] Q. Cui and M. Karplus, J. Chem. Phys. **112**, 1133 (2000).

[80] H. M. Senn and W. Thiel, Top. Curr. Chem. **268**, 173–1290 (2007).

[81] V. Barone, A. Bencini, M. Cossi, A. Di Matteo, M. Mattesini, and F. Totti, J. Am. Chem. Soc. **120**(28), 7069–7078 (1998).

[82] G. Brancato, N. Rega, and V. Barone, J. Chem. Phys. **128**, 144501 (2008).

[83] Q. Cui, M. Elstner, E. Kaxiras, T. Frauenheim, and M. Karplus, J. Phys. Chem. B **105**(2), 569–585 (2001).

[84] U. Rothlisberger, P. Carloni, K. Doclo, and M. Parrinello, J. Biol. Inorg. Chem. **5**(2), 236–250 (2000).

[85] K. Spiegel, U. Rothlisberger, and P. Carloni, J. Phys. Chem. B **108**(8), 2699–2707 (2004).

[86] D. Riccardi, P. Schaefer, Y. Yang, H. Yu, N. Ghosh, X. Prat-Resina, P. Konig, G. Li, D. Xu, H. Guo, M. Elstner, and Q. Cui, J. Phys. Chem. B **110**(13), 6458–6469 (2006).

[87] A. Laio, J. VandeVondele, and U. Roethlisberger, J. Chem. Phys. **116**, 6941–6947 (2002).

Phys. Status Solidi B **249**, No. 2 (2012)

375

[88] M. E. Moret, I. Tavernelli, and U. Rothlisberger, J. Phys. Chem. B **113**(22), 7737–7744 (2009).

[89] X. Assfeld and J. L. Rivail, Chem. Phys. Lett. **263**, 100–106 (1996).

[90] J. Pu, J. Gao, and D. G. Truhlar, J. Phys. Chem. A **108**, 632–650 (2004).

[91] S. Komin and D. Sebastiani, J. Chem. Theory Comput. **5**, 1490–1498 (2009).

[92] C. Schiffmann and D. Sebastiani, J. Chem. Theory Comput. **7**, 1307–1315 (2011).

[93] U. Rohrig, L. Guidoni, A. Laio, I. Frank, and U. Rothlisberger, J. Am. Chem. Soc. **126**, 15328–15329 (2004).

[94] U. Rohrig, L. Guidoni, and U. Rothlisberger, Chem. Phys. Chem. **6**, 1836–1847 (2005).

[95] U. F. Röhrig, I. Frank, J. Hutter, A. Laio, J. VandeVondele, and U. Rothlisberger, Chem. Phys. Chem. **4**, 1177–1182 (2003).

[96] M. A. Mroginski, F. Mark, W. Thiel, and P. Hildebrandt, Biophys. J. **93**(6), 1885–1894 (2007).

[97] M. A. Mroginski, S. Kaminski, and P. Hildebrandt, Chem. Phys. Chem. **11**(6), 1265–1274 (2010).

[98] U. F. Rohrig and D. Sebastiani, J. Phys. Chem. B **112**, 1267–1274 (2008).

Artificial Bee Colony Optimization of Capping Potentials for Hybrid Quantum Mechanical/Molecular Mechanical Calculations

Christoph Schiffmann and Daniel Sebastiani*

Physics Department, Freie Universität Berlin, Arnimallee 14, 14195 Berlin, Germany

Ⓢ *Supporting Information*

ABSTRACT: We present an algorithmic extension of a numerical optimization scheme for analytic capping potentials for use in mixed quantum—classical (quantum mechanical/molecular mechanical, QM/MM) ab initio calculations. Our goal is to minimize bond-cleavage-induced perturbations in the electronic structure, measured by means of a suitable penalty functional. The optimization algorithm—a variant of the artificial bee colony (ABC) algorithm, which relies on swarm intelligence—couples deterministic (downhill gradient) and stochastic elements to avoid local minimum trapping. The ABC algorithm outperforms the conventional downhill gradient approach, if the penalty hypersurface exhibits wiggles that prevent a straight minimization pathway. We characterize the optimized capping potentials by computing NMR chemical shifts. This approach will increase the accuracy of QM/MM calculations of complex biomolecules.

1. INTRODUCTION

Accurate simulation of structural and dynamical phenomena of complex biomolecular systems by means of first-principles molecular dynamics simulation techniques is still a challenge for modern physics and chemistry. Despite enormous progress in recent decades, predictive modeling of the interplay of intramolecular and intermolecular interactions is still far from being a routine problem. For determination of structural data in biophysics and biochemistry, the combination of spectroscopic experiments with advanced theoretical predictions and computer simulations is becoming increasingly popular, because this combination often yields a predictive power above the sum of the individual approaches.[1−9] Nevertheless, the first-principles prediction of noncovalent packing effects and the ab initio prediction of experimentally observable spectra is not possible for regular biosystems because of their inherent complexity and, last but not least, their sheer size. Thus, one has to resort either to the modeling of elementary subunits[10−14] or alternatively to hybrid quantum-mechanical + mechanical modeling (QM/MM) approaches.[15−31] One of the difficulties of such a hybrid approach is the interface region between the two different regions. If one of the atoms is located in the quantum (QM) region and the other in the classical (MM) part, then a chemical bond is "broken" as a consequence. This situation is sketched in Figure 1. Similar problems arise when MM atoms are located near a QM region, because the QM and MM descriptions are not genuinely compatible. Thus, a suitable interface has to be used, which can mutually couple the two schemes in a realistic way.

There are several well-established methods to tackle the bond saturation problem, in particular hydrogen[32] or fluorine[33] atoms, precomputed (frozen) atomic orbitals,[34,35] generalized hybrid orbitals,[36−38] quantum capping potentials,[39−42] or designed heptavalent capping potentials.[43] Complementary, effective fragment potentials[44,45] and field-adapted adjustable density matrix assembler[46−48] approach the repartiotioning problem itself. Our approach is conceptually simpler than most of the former ones; we aim at designing a fictitious capping atom to saturate the QM subsystem, which is realized by a regular atomic pseudopotential.

Specifically, we want to improve a method that has been developed recently[49] in view of more complex bond-cleavage situations. This approach is based on analytical effective core potentials (pseudopotentials) of Goedecker—Teter—Hutter (GTH) type,[50,51] in line with previous QM/MM studies.[14,23,52] Our goal is to optimize the pseudopotential parameters in such a way that the change of electronic density in the quantum part of a QM/MM calculation is minimal with respect to a "full-QM" calculation.

In this way, we also ensure that structural parameters and spectroscopic properties in the direct neighborhood of a QM/MM bond cleavage are modeled with a high degree of reliability.

To achieve this aim, we define a penalty functional that quantifies the deviation of the electronic density in a molecular fragment from the corresponding density in the complete molecule, while simultaneously penalizing changes in the equilibrium bond distance and frequency. The penalty functional is minimized iteratively by varying the coefficients of the capping potential placed at the bond-cleavage site.

However, a straightforward mimization approach like steepest descent[53,54] or a simplex method[55] carries the risk of getting stuck in local minima. To avoid this pitfall, we aim for global optimization including stochastic elements by means of a swarm intelligence-based algorithm. In recent years, biology-inspired algorithms[56,57] turned out to be more effective than conventional algorithms.[58]

In this work, we employ a variation of the artificial bee colony algorithm[59−61] (ABC), which mimicks the foraging behavior of honeybees for function minimization. We are especially interested in proving the usablility for optimizations within electronic structure calculations and studying the performance of the algorithm. The optimized capping potentials are intended to

Figure 1. General QM/MM repartitioning principle in which the C—R2 bond crosses the QM/MM border and is cleaved. The CH_2 group is replaced by a capping potential associated with a fictitious particle D, saturating the C—R1 bond and hence terminating the QM region.

saturate the quantum region in hybrid QM/MM calculations. In most cases, this saturation affects a single C—C bond and can therefore be done by means of a hydrogenoid atom; however, the properties of this hydrogenoid atom should resemble as much as possible the characteristics of the carbon atom that has been "cut" out from the quantum calculation. Hence, we need a fictitious atom that is monovalent but behaves like a (four-valent) carbon atom in terms of bond distance, potential energy curve(s), and electronic structure.

We further characterize the perturbative effect of bond cleavage by means of NMR chemical shifts, which are known to be particularly sensitive to both intramolecular electronic structure and intermolecular effects such as hydrogen bonding.[62−66] Hence, we can not only gauge the direct perturbing effect of the cleaved bond on the electronic structure of the remaining part of a molecule but also quantitatively describe how strongly its response properties are tainted by the QM/MM bond cleavage.

2. OPTIMIZATION APPROACH

In QM/MM calculations, the dummy atom has to saturate the last covalent bond in the quantum region of the molecule, that is, the bond that is cleaved by QM/MM repartitioning. The true character of the bond, however, cannot be easily reproduced by a simple terminal atom. It is therefore necessary to tune the dummy's properties in a way that the resulting deviation in the quantum region's electronic structure is minimal. To do so, one has to find a capping potential that equips the dummy with the desired properties.

2.1. Definition of Penalty Functional. Our optimization scheme aims to find a capping potential V_{cap} that gives rise to an electronic density in the quantum region ($\rho[V_{cap}]$) that deviates only in a minimal manner from the reference electron density (ρ^{ref}), that is, the density when the whole molecule is quantum-mechanically treated. Further, we want to preserve the equilibrium bond length and vibrational properties of the bond that is cleaved to allow for an easy coupling of the first classical MM atom and to avoid the need for additional geometric constraints (see Komin and Sebastiani[49] and von Lilienfeld-Toal et al.[67] for a more detailed description).

Therefore, we define a functional that penalizes deviations of these properties from their target values obtained in a full-QM calculation:

$$\mathscr{P}[V_{cap}] = \omega_\rho \sum_{j=1}^{N_{geo}} \int_\Omega d^3r \, |\rho_j^{ref}(\mathbf{r}) - \rho_j[V_{cap}](\mathbf{r})|^2 + \omega_f \sum_{j=1}^{N_{geo}} |\mathbf{F}_j^{ref}$$

$$- \mathbf{F}_j[V_{cap}]|^2 + \omega_e \sum_{j=2}^{N_{geo}} |(E_j^{ref} - E_1^{ref}) - (E_j[V_{cap}] - E_1[V_{cap}])|^2$$

$$(1)$$

The integration volume Ω is restricted to an area where penalization is meaningful, that is, the union of spheres around all QM atoms except the dummy with radii r_{cov}^{spc}, where r_{cov}^{spc} is the covalent radius of the atom species (spc). $\mathbf{F}$ denotes the force acting on the dummy (with respect to its uncapped counterpart) and E is the total energy. ω_ρ, ω_f, and ω_e are weighting factors that ensure an adequate relative importance between density, force, and energy penalization. Finally, the penalty is evaluated for $N_{geo} = 3$ molecular geometries, which correspond to variations of the cleaving bond length.

We note at this point that we have replaced a multielectron group (e.g., methyl) with a fictitious monovalent atom, which changes the total number of electrons in the system. Hence, the integration of a direct density difference can never vanish completely, unless the affected regions are entirely excluded from the integration. This also leads to the effect that the penalty functional will in general never reach zero during a capping potential optimization.

2.2. GTH Pseudopotentials. We assume that an optimal capping potential can be expressed as an analytical GTH potential:[50,51]

$$V_{cap}(\mathbf{r},\mathbf{r}') = V_{loc}(\mathbf{r}) + \sum_{l=0}^{l_{max}} V_l(\mathbf{r},\mathbf{r}') \quad (2)$$

consisting of a local component V_{loc}, eq 3, and 0−3 (l_{max}) nonlocal components V_l, eq 4, with the form

$$V_{loc}(r) = \frac{-Z_{ion}}{r} \operatorname{erf}\left(\frac{r}{\sqrt{2}r_{loc}}\right)$$

$$+ \exp\left[-\frac{1}{2}\left(\frac{r}{r_{loc}}\right)^2\right] \sum_{j=1}^{4} C_j \left(\frac{r}{r_{loc}}\right)^{2(j-1)} \quad (3)$$

$$V_l(\mathbf{r},\mathbf{r}') = \sum_{i=1}^{3} \sum_{j=1}^{3} \sum_{m=-l}^{+l} Y_{l,m}\left(\frac{\mathbf{r}}{r}\right) p_i^l(r) h_{i,j}^l p_j^l(r') Y_{l,m}\left(\frac{\mathbf{r}'}{r'}\right) \quad (4)$$

$$p_i^l(r) = \frac{\sqrt{2}r^{l+2(i-1)}\exp\left(-\frac{r^2}{2r_l^2}\right)}{r_l^{l+(4i-1)/2}\sqrt{\Gamma\left(l+\frac{4i-1}{2}\right)}} \quad (5)$$

Z_{ion} is a valence charge, $Y_{l,m}$ are spherical harmonics, and $h_{i,j}^l$ are scalars that define the energetic weighting of projectors $p_{i/j}^l$, eq 5, in each angular momentum channel l.

A potential of this type is fully defined via the set of N_σ parameters:

$$\{r_{loc}, C_1, C_2, C_3, C_4, r_0, h_{1,1}^0, h_{2,2}^0, h_{3,3}^0, r_1, h_{1,1}^1, ..., r_2, h_{1,1}^2, ...\} \quad (6)$$

In the following, we use $\{\sigma\}$ as simplified notation for this set.

From physical considerations, we impose an allowed interval for each parameter. Thus, the optimization takes place in an N_σ dimensional orthorhombic manifold in $\mathbb{R}^{N_\sigma}$.

2.3. Artificial Bee Colony (ABC). The actual optimization algorithm is taken from the field of swarm intelligence and as such is inspired by nature itself. It mimics the foraging behavior of honeybees to sample a scalar function defined on an N_σ-dimensional unit cube (U_σ) in an efficient manner. We use a set of linear transformations to rescale and shift the allowed parameter space into the unit cube.

We define a *population* as a set of N_{pop} agents, each representing a configuration $\{\sigma\}_a \in U_\sigma$ and the corresponding penalty
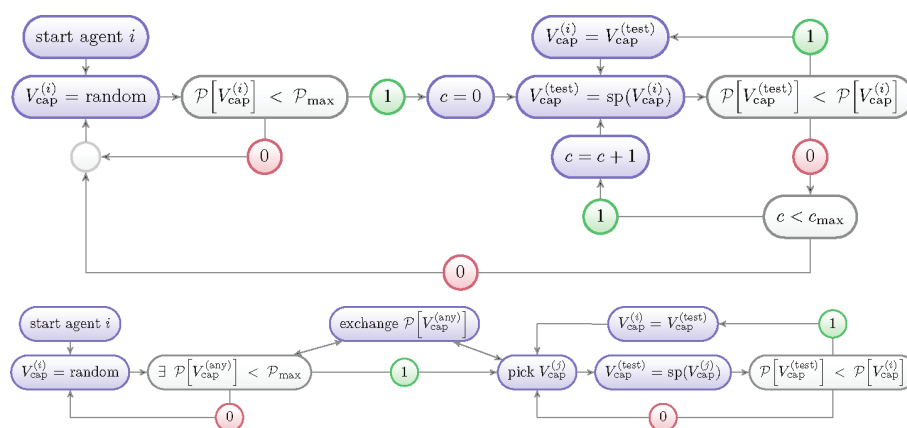
1308

dx.doi.org/10.1021/ct1007108 |J. Chem. Theory Comput. 2011, 7, 1307–1315

Figure 2. Employee-type (top) and onlooker-type (bottom) agents.

$\mathscr{P}[\{\sigma\}_a]$. This artificial bee colony (ABC) algorithm distiguishes three types of agents which, like honeybees in nature, fulfill simple but different tasks:

- Scout-type agents have the biggest exploration tendency of the three types. A scout chooses in every cycle a random point $\{\sigma\}$ from uniform distribution in U_σ and moves unconditionally to that spot (global sampling).
- Employee-type agents have an additional local sampling component. An employee type starts like a scout but examines in each cycle a random spot $\{\sigma\}'$ from a uniform distribution in a sphere of radius r_s around its present position $\{\sigma\}$. The agent moves only if $\mathscr{P}[\{\sigma\}'] < \mathscr{P}[\{\sigma\}]$. Furthermore, if the agent cannot move for N_a successive cycles, it *abandons* its present position and restarts the search again from a fully random spot in U_σ.
- Onlooker-type agents act, from the point of view of the entire agent population, as feedback and amplify the exploitation of promising areas in U_σ that have been found by other agents. Equipped with knowledge of all agents' positions and penalties, an onlooker type randomly choses another agent's parameter set $\{\sigma\}$, inversely weighted by the penalties. Then it chooses a spot $\{\sigma\}'$ from a uniform distribution in a sphere of radius r_s around $\{\sigma\}$ and moves if $\mathscr{P}[\{\sigma\}']$ is smaller than its original penalty. Thus, this type depends on the other agents' results and ensures that good parameter regions are not lost during an employee-type resetting.

A more detailed description of employee- and onlooker-type agents and their "interactions" is given in the flowcharts in Figure 2.

Optimization starts with *initialization* of the population. In this phase, every agent, regardless of its type, is randomly placed in U_σ. Afterward, the ABC algorithm performs N_{cycle} *cycles*, each a sequence of three steps:

1. Send the employee- and onlooker-type agents to their destinations and evaluate the penalties.
2. Place the scout-type agents and the employee-type agents that abandoned their positions randomly in U_σ.
3. Store the pseudopotential parameter set $\{\sigma\}$ with the lowest penalty in the present population.

Thus, the interaction of the three types of agents, determined by the ABC algorithm, successivly searches for the global minimum $\mathscr{P}[\{\sigma\}_{min}]$ of the penalty functional.

The pseudocode of the ABC algorithm is given in Chart 1.

2.4. Evolution and Convergence of Optimization. We define a combined index for the evolution of all agents:

$$\tau := i \cdot N_{pop} \qquad (7)$$

where $0 \leq i \leq N_{cycle}$ denotes the current optimization cycle. Thus, τ corresponds to the computational cost under the assumption that determination of the penalty $\mathscr{P}[\{\sigma\}]$ has a fixed computational cost for all choices of $\{\sigma\}$. As this assumption cannot be enforced formally, we limit the number of self-consistent-field (SCF) iterations during the wave function optimization for each penalty evaluation to 30. With this combined index we can describe the evolution of the ensemble of agents during one optimization run via

$$\mathscr{P}(\tau = 0) := \min_{j=1,\ldots,N_{pop}} \{\mathscr{P}[\{\sigma\}_{j,i=0}]\}$$

$$\mathscr{P}(\tau > 0) := \min\left(\mathscr{P}(\tau - N_{pop}), \min_{j=1,\ldots,N_{pop}} \{\mathscr{P}[\{\sigma\}_{j,i\neq0}]\}\right) \qquad (8)$$

where $\{\sigma\}_{j,i}$ are the pseudopotential parameters of agent j in the ith optmization cycle (the case $i = 0$ denotes the initialization phase). Hence, (τ) and $\{\sigma\}(\tau)$ refer to the minimal penalty after an optimization time τ and the corresponding pseudopotential parameter set.

To account for the stochastic nature of the optimization process, we run N_{trial} independent optimizations for each set of control parameters (i.e., the number of employee- and onlooker-type agents as well as the radius of the neighborhood sphere r_s). This enables us to describe the convergence behavior in statistical terms. We distinguish between different optimization runs by a new superscript $1 \leq k \leq N_{trial}$:

$$\mathscr{P}_{min}(\tau) = \min_{k=1,\ldots,N_{trial}} \{\mathscr{P}^k(\tau)\} \qquad (9)$$

$$\mathscr{P}_{max}(\tau) = \max_{k=1,\ldots,N_{trial}} \{\mathscr{P}^k(\tau)\} \qquad (10)$$

Equations 9 and 10 describe a window in which all $\mathscr{P}^k(\tau)$ are located for a fixed setting of control parameters (best- and worst-case scenarios).

2.5. Computational Details. We perform all calculations within density functional theory[68−70] using the BLYP[71,72] exchange—correlation functional, as implemented in the CPMD package.[73,74]

1309

dx.doi.org/10.1021/ct1007108 |*J. Chem. Theory Comput.* 2011, 7, 1307–1315

Chart 1. Pseudocode of the ABC Algorithm

```
initialize population randomly
for i = 1...N_cycles do
        run employee types
        run onlooker types
        run scout types
        abandon solutions
        update best solution
done
```
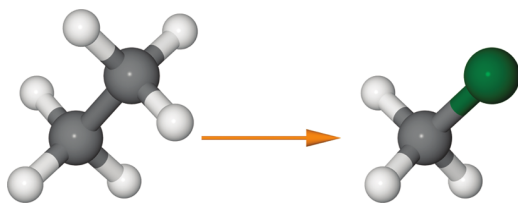

Figure 3. Ethane (C_2H_6) as test system for benchmarking. One methyl group is replaced by a capping potential (green particle), which saturates the remaining methyl group.

We use standard norm-conserving pseudopotentials[50,51] and an energy cutoff of 70 Ry for the plane-wave expansion of the Kohn−Sham orbitals.

Calculation of spectroscopic parameters, for example, NMR chemical shifts, is done within density functional perturbation theory as implemented in the linear response package of CPMD.[75−77]

3. RESULTS

3.1. Stochastic Optimization of Capping Potentials. We have applied the ABC algorithm to the optimization of GTH-type capping potentials V_{cap} for hybrid QM/MM calculations within DFT. In particular, we have examined the influence of control parameters of the ABC algorithm (i.e., the number of employee and onlooker type agents and the radius of the neighborhood sphere r_s) on the optimization process. For this purpose, we benchmarked a series of capping potential optimizations for an isolated ethane molecule (C_2H_6) in which one methyl group is replaced by a capping potential, with respect to a dummy particle D, as shown in Figure 3.

We begin the presentation of our optimization benchmarks with the effect of number of employee- (E) and onlooker- (O) type agents on evolution of the ensemble of agents for different population sizes. For the initial benchmarks, a fixed value of $r_s = 0.2$ is used. N_a is set to 10 and the penalty weights are $\omega_\rho = 1$, $\omega_f = 0.01$, and $\omega_e = 2$ (arbitrary units). We initialize the first agent in each optimization run with the standard carbon GTH pseudopotential. To allow for a higher level of flexibility of the capping potential, we add an angular momentum channel ($l = 1$) with one projector, which leads to a 7-dimensional parameter space.

Figures 4−6 show penalty minimization over an optimization time $0 \leq \tau \leq 800$ for $N_{pop} = 4$, 12, and 20, respectively. Each figure shows the penalty evolution window as described by eqs 9 and 10 for different population setups $E + O = N_{pop}$. The number of trial runs is $N_{trial} = 5$ for each choice of E/O. An employee-type agent abandons its position after $N_a = 10$ unsuccessful cycles.

We observe in Figure 4 ($N_{pop} = 4$) a fast decrease of the lower penalty boundary $\mathscr{P}_{min}(\tau)$ during $\tau \leq 100$ for all E/O combinations.
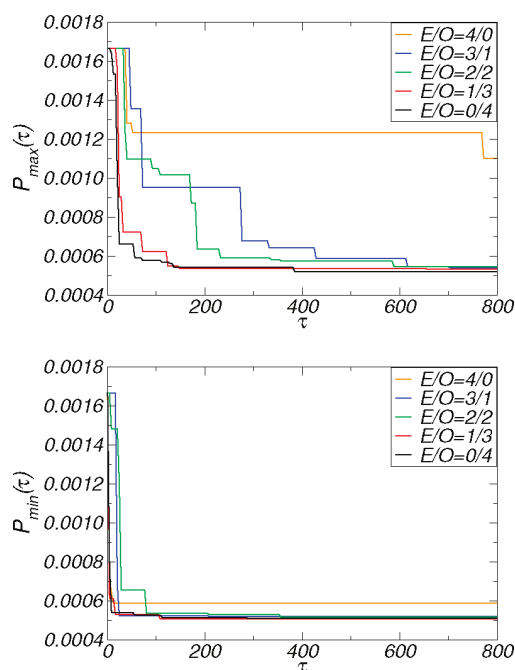

Figure 4. Population size/setup benchmarks: upper penalty boundary $\mathscr{P}_{max}(\tau)$ and lower penalty boundary $\mathscr{P}_{min}(\tau)$ with $E + O = 4$, $r_s = 0.2$, and $N_{trial} = 5$.

This boundary remains practically unchanged for the remaining optimization. On the other hand, the upper penalty boundary $\mathscr{P}_{max}(\tau)$ shows a decay comparable to that of the lower penalty boundary but only for combinations with no or few employee-type agents. For equal numbers of employee/onlooker-type agents or a higher amout of employee types, the upper penalty boundary decreases on a much slower time scale with practically no convergence in the all-employee-type case ($E = N_{pop}$).

Very similar behavior of the lower penalty boundary is observed for $N_{pop} = 12$ (Figure 5). The decrease of the upper penalty boundary is similar for combinations from 0 to 6 employee-type agents, and significantly slower for higher numbers of E. The decrease of $\mathscr{P}_{max}(\tau)$ happens on a slightly longer time scale compared to the optimization benchmarks with $N_{pop} = 4$.

This trend remains valid for $N_{pop} = 20$ (Figure 6). The decrease of the penalty window (i.e., the interval $[\mathscr{P}_{min}(\tau), \mathscr{P}_{max}(\tau)]$) is significantly slower compared to smaller populations.

As an extreme case of employee/onlooker combinations, we show in Figure 7 the upper and lower penalty boundaries for a series of $N_{trial} = 5$ optimization runs with a population consisting of only one agent of employee type and $N_a > N_{cycle}$ The lower penalty boundary reaches its minimum after an optimization time of $\tau \approx 230$. The upper penalty boundary needs nearly $\tau \approx 800$ to approach the value of the lower boundary.

The second control parameter of the optimization algorithm is the size of the neighborhood sphere r_s. Again, we run a series of independent optimizations with a fixed population setup of 3 employee and 9 onlooker types, with $N_a = 10$, $\omega_\sigma = 1$, $\omega_f = 0.01$, and $\omega_e = 2$. We show in Figure 8 the upper penalty boundary $\mathscr{P}_{max}(\tau)$ and lower penalty boundary $\mathscr{P}_{min}(\tau)$ for different radii r_s, with $N_{trial} = 5$ runs each.

We observe a steady (but slow) minimization behavior for small radii $r_s \leq 0.01$. Intermediate radii ($r_s = 0.1$ and 0.2) lead to a fast decrease of the penalty window ($[\mathscr{P}_{min}(\tau), \mathscr{P}_{max}(\tau)]$).
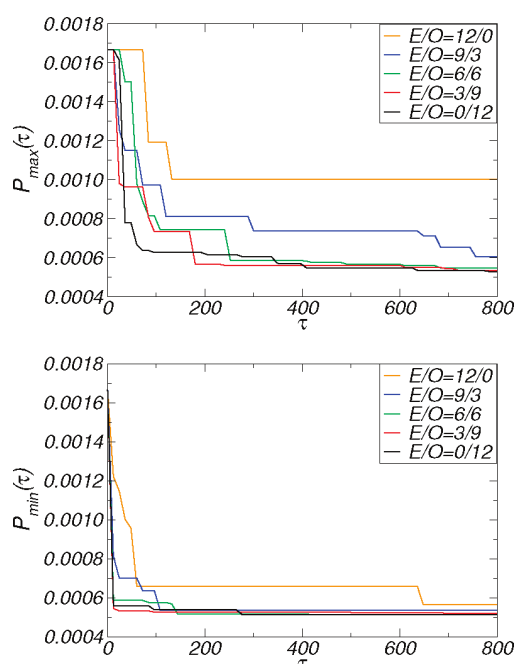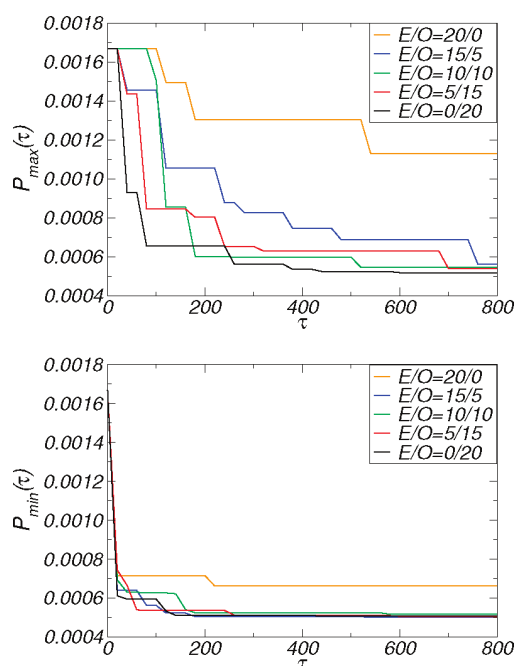
Figure 5. Population size/setup benchmarks: upper penalty boundary $\mathscr{P}_{\max}(\tau)$ and lower penalty boundary $\mathscr{P}_{\min}(\tau)$ with $E + O = 12$, $r_s = 0.2$, and $N_{\mathrm{trial}} = 5$.

Figure 6. Population size/setup benchmarks: upper penalty boundary $\mathscr{P}_{\max}(\tau)$ and lower penalty boundary $\mathscr{P}_{\min}(\tau)$ with $E + O = 20$, $r_s = 0.2$, and $N_{\mathrm{trial}} = 5$.

Bigger radii lead to a comparable decrease in the lower penalty boundary. The upper penalty boundary, however, decreases quite slowly and unsteadily.

The optimizations presented so far have all used the conventional carbon GTH pseudopotential as starting point. While this appears adequate for the particular situation of homolytic C−C
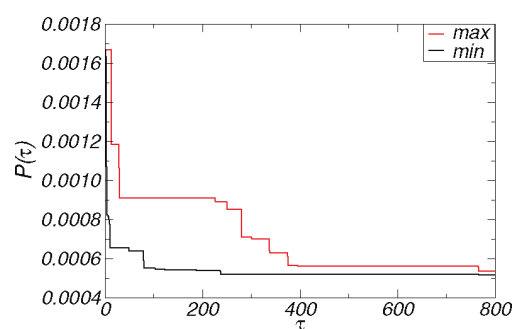

Figure 7. Single employee-type agent: lower penalty boundary $\mathscr{P}_{\min}(\tau)$ and upper penalty boundary $\mathscr{P}_{\max}(\tau)$ with $E = N_{\mathrm{pop}} = 1$, $r_s = 0.2$, and $N_{\mathrm{trial}} = 5$.
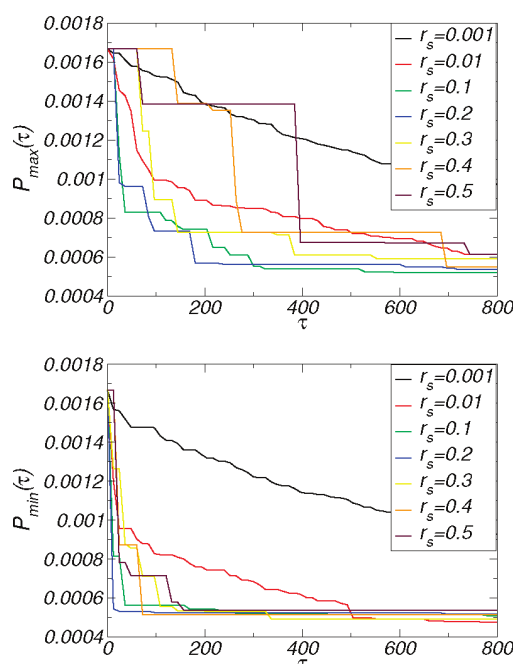

Figure 8. Sphere radius r_s benchmarks: upper penalty boundary $\mathscr{P}_{\max}(\tau)$ and lower penalty boundary $\mathscr{P}_{\min}(\tau)$ with $N_{\mathrm{pop}} = 12$, $E/O = 3/9$, and $N_{\mathrm{trial}} = 5$.

bond capping, we aim at designing capping potentials for more complex settings. In order to test the performance of our ABC algorithm in more difficult circumstances, we repeat the optimization of our C−C capping potential from a starting point with randomized capping parameters.

For a population of $E + O = 12$, $N_a = 10$, $r_s = 0.2$, $\omega_\rho = 1$, $\omega_f = 0.01$, and $\omega_e = 2$, we perform $N_{\mathrm{trial}} = 5$ independent optimizations with varying combinations for E/O. The evolution for this unfavorable initialization of agents is shown in Figure 9.

The behavior of the lower penalty boundary is nearly identical for small to intermediate numbers of employee types. It decreases more slowly for a higher amount of employee types. The upper penalty boundary shows a similar pattern for all E/O combinations, but an equal amount of employee and onlooker types shows the best performance in an early stage of the optimization.

Regarding the combination of employee and onlooker agents, it turns out that the optimal ratio depends strongly on whether the present set of agents is "in direct view" of the final minimum,
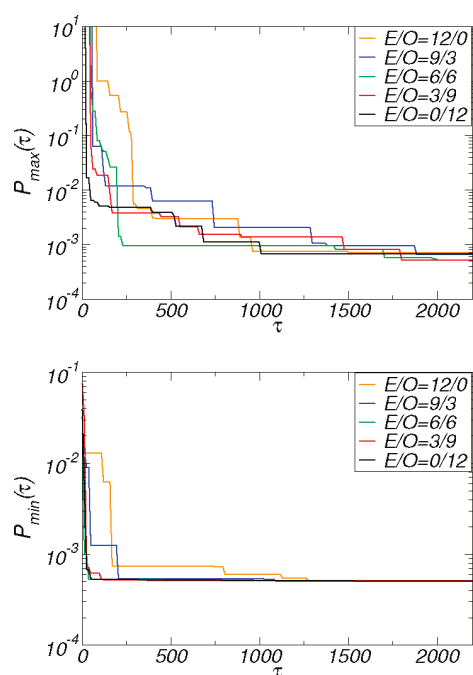
1311

dx.doi.org/10.1021/ct1007108 |*J. Chem. Theory Comput.* 2011, 7, 1307–1315

Figure 9. Population setup benchmarks: upper penalty boundary $\mathscr{P}_{max}$ (τ) and lower penalty boundary $\mathscr{P}_{min}(\tau)$ with $E + O = 12$, $r_s = 0.2$, and $N_{trial} = 5$ with fully random initialization.

Figure 10. Distribution $n(\Delta\delta)$ of the isotropic NMR chemical shift $\Delta\delta$ of carbon atoms in hexane with V_{cap} bound to C_1 for an ensemble of 75 capping potentials obtained from independent optimizations: (top) hexane geometry; (bottom) optimized geometry for V_{cap}.

that is, in its proximity and without additional barriers on the way. For a good starting point of the optimization, for example, the feedback process inherent to onlooker agents leads to a speedup of the optimization, and zero agents of employee type are best. On the other hand, a nonoptimal starting point (as obtained via the randomized initialization) requires a certain number of agents with explorative character, that is, employee (or scout) type agents. Hence, it might eventually be useful to switch the distribution of employee versus onlooker types during the progress of the optimization. Investigation of this effect, however, exceeds the scope of the present paper.

As for the sphere radius r_s, we find that a small value leads to a slow "speed" of the agents in parameter space. A large value, on the other hand, allows for large moves. However, the plateaus in the evolution of $\mathscr{P}_{max}$ (Figure 8) for $r_s \geq 0.4$ illustrate that a large neighborhood area leads to a high rejection rate for the proposed moves of the agents. We find that an intermediate choice of $0.1 \leq r_s \leq 0.2$ leads to the fastest decay of the penalty window, due to a trade-off between the "speed" of the agents in parameter space and their rejection rate. We believe that this behavior indicates a rich structure of the penalty surface, even for this simple case of homolytic C−C bond capping.

3.2. Initial Benchmark of Optimized Capping Potentials. To examine the quality of optimized capping potentials obtained during our benchmarks, we compute electronic linear response properties for a linear alkane molecule (hexane) in which the terminal methyl group is replaced by a capping potential. In particular, we compute spectroscopic properties that involve both the occupied and excited manifold of electronic orbitals. These parameters measure the performance of our capping potential beyond the scope that is accessible by the penalty functional (eq 1) because the latter is based only on the ground-state density.
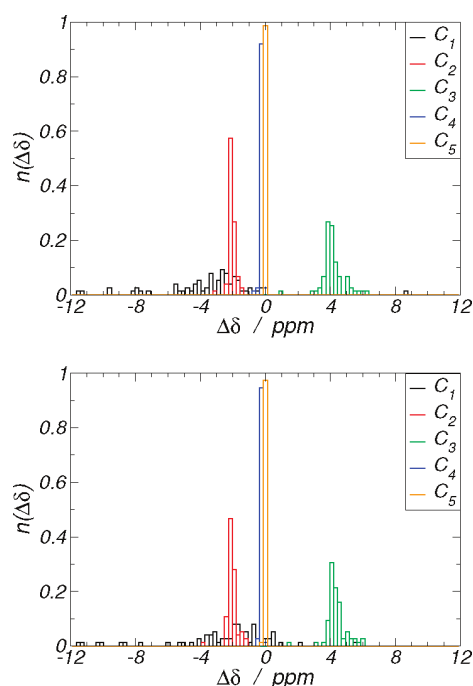
We have chosen ^{13}C NMR chemical shifts δ for the characterization of our capping potentials. These chemical shifts are the result of a complex interplay of occupied and excited electronic states. Nevertheless, they are relatively short-sighted, which means that a perturbation in the electronic spectrum reaches no further than a few covalent bonds. Hence, they allow us to monitor the range in which the QM/MM-induced bond cleavage perturbs the electronic subsystem.

Specifically, we compute the distribution of deviations of the trace of the nuclear shielding tensor $\sigma_{\alpha\beta}$ for a capped molecule with respect to a full calculation:

$$\Delta\delta = \mathrm{Tr}(\sigma_{\alpha\beta}[\text{full-QM}] - \sigma_{\alpha\beta}[\text{QM/MM}]) \qquad (11)$$

This is done (1) in the optimized geometry of the full hexane molecule and (2) in a geometry that has been optimized by use of V_{cap}. In both cases, we obtain an ensemble of chemical shift values from the ensemble of independent optimization runs.

Figure 10 shows the distribution of $\Delta\delta$ of carbon atoms C_i, where C_1 is the direct neighbor of V_{cap}. For both geometries, we observe a similar picture: $\Delta\delta$ of the direct neighbor of V_{cap} has a broad distribution with a clustering between −3 and −2 ppm. The distribution for next two carbon atoms (C_2 and C_3) have distinct peaks at −2 and 4 ppm, respectively. As for the last two carbons, we find only minor deviations, far below 1 ppm, from the reference NMR signature.

3.3. Application to Octane. While the main focus in this article is on the algorithmic performance of the ABC algorithm in the QM/MM context, we have nevertheless applied the ABC/ capping potential algorithm to C−C bond cleavage in a larger molecule, specifically octane. Here, a butane fragment has been replaced by a capping potential; see Figure 11.
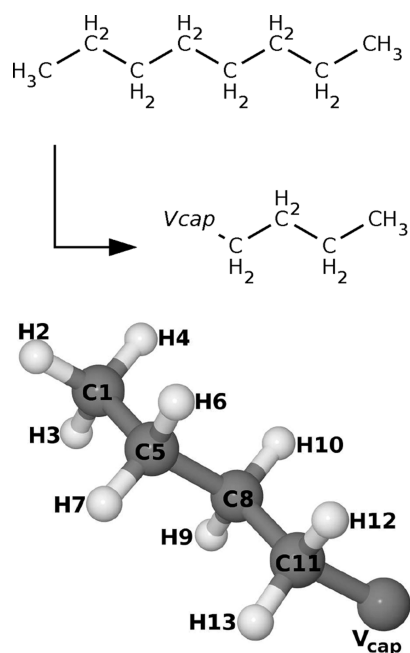
Figure 11. Reference system octane and its capped counterpart: (top) bond-capping scheme and (bottom) atom numbering.

Table 1. GTH Parameters for Regular Carbon and Optimized C−C Capping Potential V_{cap}

	r_{loc}	C_1	C_2	r_0	$h_{1,1}^0$	r_1	$h_{1,1}^1$
regular C	0.3376	−9.1285	1.4251	0.3025	9.6507		
V_{cap}	0.2101	−13.1925	3.4867	0.2416	6.2451	0.3125	9.7340
ref 49	0.7221	9.9086	−2.5466	0.5120	−3.5081	1.4664	0.2316

The optimization is performed over 500 cycles with $E = 4$ and $O = 6$, a neigborhood sphere radius of $r_s = 0.1$, and an integration volume for the density difference consisting of spheres of size $1.5\times$ covalent radius around each atom except V_{cap}. The penalty weighting factors are $\omega_\rho = \omega_f = \omega_e = 1$. See Table 1 for the initial guess (regular carbon) and optimized capping potential parameters (V_{cap}).

All geometric parameters (shown in Table 2) of the capped octane molecule are in excellent agreement with the full octane reference. This agreement holds for our new optimized potential as well as for a previous version,[49] and to some degree even for the simpler hydrogen and fluorine cappings. While the hydrogen termination looks like an accurate way of capping when the H−C bond distance is ignored, it has a strong effect on the properties of the subsequent C−C bond. This is shown in the potential energy curve (Figure 12) of the C_8−C_{11} bond: when hydrogen capping is applied, the equilibrium distance is shortened by about 0.1 Å and its frequency is considerably blue-shifted.

When the NMR chemical shift deviations (shown in Table 3) are examined, a more heterogeneous picture arises. The conventional H- and F-based cappings are only in very rough agreement with the reference system, while both capping potentials yield satisfactory results. When the latter two are compared, it turns out that in our presently optimized capping potential (V_{cap}), the first (C_{11}) and third (C_5) carbon atoms exhibit somewhat larger deviations than the potential from ref 49, while the intermediate carbon (C_8) and most of the hydrogens show better agreement. It is not clear at present what is the specific reason for these

Table 2. Optimized Bond Lengths, Angles, and Dihedrals of the Octane Reference Molecule and Its Capped Counterpart

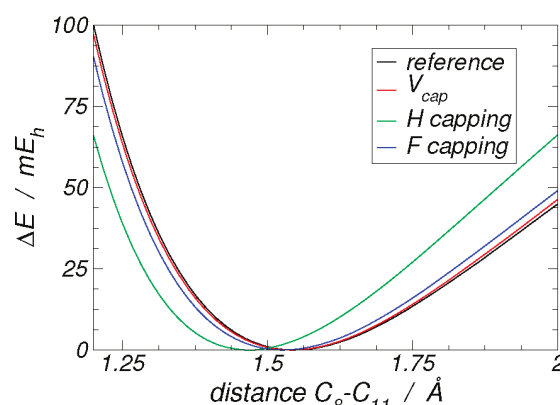|	reference	V_{cap}	hydrogen	fluorine	ref 49
C_1−C_5 (Å)	1.54	1.55	1.55	1.54	1.55
C_5−C_8 (Å)	1.55	1.55	1.55	1.55	1.55
C_8−C_{11} (Å)	1.55	1.54	1.55	1.53	1.55
C_{11}−V_{cap} (Å)	1.55	1.62	1.10	1.47	1.55
C_1−C_5−C_8 (deg)	113.4	113.5	113.6	113.1	113.7
C_5−C_8−C_{11} (deg)	113.6	113.5	113.6	111.7	113.4
C_8−C_{11}−V_{cap} (deg)	114.0	113.7	111.3	110.2	116.2
C_1−C_5−C_8−C_{11} (deg)	−179.3	−179.9	179.8	−179.6	−177.2
C_5−C_8−C_{11}−V_{cap} (deg)	−179.5	−178.2	−179.3	179.6	179.7

Figure 12. Potential energy curve of the C_8−C_{11} bond.

Table 3. ^1H and ^{13}C NMR Chemical Shift Changes of the Capped Octane Molecule with Respect to Its Octane Reference, $\Delta\delta = \sigma^{cap} - \sigma^{ref}$

$\Delta\delta$	chemical shift change (ppm)			
	V_{cap}	hydrogen	fluorine	ref 49
C_1	0.16	−0.08	0.56	0.56
H_2	0.03	0.01	−0.02	0.02
H_3	0.04	0.01	−0.06	0.03
H_4	0.04	0.02	−0.05	0.02
C_5	−5.03	−1.56	6.77	−1.12
H_6	0.12	0.07	0.14	0.14
H_7	0.13	0.07	0.15	0.22
C_8	−0.02	5.52	0.81	−0.32
H_9	−0.40	−0.07	−0.47	−0.34
H_{10}	−0.41	−0.06	−0.48	−0.41
C_{11}	12.08	18.01	−52.08	−2.44
H_{12}	−0.23	0.37	−3.49	−0.18
H_{13}	−0.24	0.36	−3.47	−0.15

deviations in terms of the capping parameters (given numerically in Table 1). It is obvious, however, that the two capping potentials have very different characteristics in terms of the range of their local and nonlocal parts; in particular, the radius of the local part (r_{loc}) differs by a factor of more than 3, as does r_1.

Nevertheless, this result clearly illustrates that the ABC algorithm with its stochastic elements has the very important ability

to discover new regions of parameter space, which a downhill algorithm (e.g., conjugate gradients) would never explore. In order to obtain better capping potentials in terms of spectroscopic parameters, the optimization can now be adjusted by means of weighting factors and the exact definition of penalty integration volume. However, this is beyond the scope of the present work and will be highlighted in a forthcoming article.

4. CONCLUSION

In this work, we have presented an algorithmic extension of a numerical optimization scheme for capping potentials that can be used for mixed quantum–classical (QM/MM) ab initio calculations. The new algorithm mixes deterministic (downhill gradient) techniques with stochastic (Monte Carlo-like) moves, which are applied to an analytic potential such that the electronic structure in the quantum region is preserved as well as possible with respect to a reference (full-QM) calculation. Deviations from the ideal electronic (and geometric) structure are characterized by a suitably designed penalty functional, which represents the target quantity that is minimized with respect to the parameters of the capping potential.

Our algorithm is a variant of the artificial bee colony (ABC) approach, which has certain analogies to the foraging behavior of honeybees in nature. From a computational view, it bears similarities to the ideas used in parallel tempering schemes. The stochastic elements that are incorporated into the ABC optimization avoid trapping in local minima of the penalty functional hypersurface. For the benchmark molecule (ethane) used in this work, this surface is still relatively smooth; however, as soon as more complex molecules are targeted, the stochastic components of the ABC algorithm are very important due to the presence of numerous wiggles in this surface. This could be shown by using a randomized starting point for the capping potential optimization. For such more complex situations, several control parameters of the ABC scheme can be adjusted in order to improve the convergence behavior.

The properties of the resulting capping potentials have been characterized in terms of the deviations of carbon NMR chemical shift values with respect to a reference calculation. For our homolytic cleavage of a C^{sp3}–C^{sp3} bond, the properties resemble those of the optimized capping potentials that were obtained previously by the deterministic simplex minimization approach.[49] In turn, our new algorithm has found a considerably different set of values of the capping parameters, mainly because of the use of a slightly different set of weighting parameters within the penalty functional. This illustrates that the penalty surface has indeed a rich substructure, even in a very simple case such as the homolytic capping of ethane.

We believe that the new ABC optimization scheme will help generating better capping potentials for more complex situations in which special care is necessary. In particular, we are presently applying the algorithm to heterolytic bond cleavage (i.e., C–N and C–O bonds), as well as the capping of highly polar and charged groups (i.e., COOH and COO$^-$), which are of crucial importance for most biophysical QM/MM simulations.

ASSOCIATED CONTENT

⬤ Supporting Information. Additional text and one figure describing complementary benchmark optimization. This material is available free of charge via the Internet at http://pubs.acs.org.

AUTHOR INFORMATION

Corresponding Author
*E-mail: daniel.sebastiani@fu-berlin.de.

ACKNOWLEDGMENT

REFERENCES

(1) Gascon, J. A.; Sproviero, E. M.; Batista, V. S. *J. Chem. Theory Comput.* **2005**, *1*, 674–685.

(2) Kongsted, J.; Nielsen, C. B.; Mikkelsen, K. V.; Christiansen, O.; Ruud, K. *J. Chem. Phys.* **2007**, *126*, No. 034510.

(3) Sebastiani, D. *Nachr. Chem.* **2009**, *57*, 305.

(4) Schmidt, J.; Hoffmann, A.; Spiess, H. W.; Sebastiani, D. *J. Phys. Chem. B* **2006**, *110*, 23204–23210.

(5) Schmidt, J.; Hutter, J.; Spiess, H. W.; Sebastiani, D. *ChemPhysChem* **2008**, *9*, 2313–2316.

(6) Heller, J.; Elgabarty, H.; Zhuang, B.; Sebastiani, D.; Hinderberger, D. *J. Phys. Chem. B* **2010**, *114*, 7429–7438.

(7) Banyai, D. R.; Murakhtina, T.; Sebastiani, D. *Magn. Reson. Chem.* **2010**, *48*, S56–S60.

(8) Ludueña, G. A.; Wegner, M.; Bjålie, L.; Sebastiani, D. *ChemPhysChem* **2010**, *11*, 2353–2360.

(9) Hansen, M. R.; Sekharan, S.; Graf, R.; Sebastiani, D. *J. Am. Chem. Soc.* **2009**, 5251–5256.

(10) Gervais, C.; Dupree, R.; Pike, K. J.; Bonhomme, C.; Profeta, M.; Pickard, C. J.; Mauri, F. *J. Phys. Chem. A* **2005**, *109*, 6960–6969.

(11) Yates, J. R.; Dobbins, S. E.; Pickard, C. J.; Mauri, F.; Ghi, P. Y.; Harris, R. K. *Phys. Chem. Chem. Phys.* **2005**, *7*, 1402–1407.

(12) Yates, J. R.; Pham, T. N.; Pickard, C. J.; Mauri, F.; Amado, A. M.; Gil, A. M.; Brown, S. P. *J. Am. Chem. Soc.* **2005**, *127*, 10216–10220.

(13) Murakhtina, T.; Delle Site, L.; Sebastiani, D. *ChemPhysChem* **2006**, *7*, 1215–1219.

(14) Rohrig, U.; Guidoni, L.; Laio, A.; Frank, I.; Rothlisberger, U. *J. Am. Chem. Soc.* **2004**, *126*, 15328–15329.

(15) Deng, R. Z.; Martyna, G. J.; Klein, M. L. *Phys. Rev. Lett.* **1993**, *71*, 267.

(16) Stanton, R. V.; Little, L. R.; Merz, K. M. *J. Phys. Chem.* **1996**, *99*, 11266.

(17) Eichinger, M.; Tavan, P.; Hutter, J.; Parrinello, M. *J. Chem. Phys.* **1999**, *21*, 10452.

(18) Lyne, P.; Hodosceck, M.; Karplus, M. *J. Phys. Chem. A* **1999**, *103*, 3462–3471.

(19) Field, M. J.; Bash, P. A.; Karplus, M. *J. Comput. Chem.* **1990**, *11*, 700–733.

(20) Zhang, Y.; Lee, T.-S.; Yang, W. *J. Phys. Chem.* **1999**, *110*, 46–54.

(21) Brancato, G.; Rega, N.; Barone, V. *J. Chem. Phys.* **2008**, *128*, 144501.

(22) Cui, Q. *J. Chem. Phys.* **2002**, *117*, 4720–4728.

(23) Laio, A.; VandeVondele, J.; Roethlisberger, U. *J. Chem. Phys.* **2002**, *116*, 6941–6947.

(24) Cui, Q.; Karplus, M. *J. Chem. Phys.* **2000**, *112*, 1133.

(25) Laio, A.; VandeVondele, J.; Rothlisberger, U. *J. Phys. Chem. B* **2002**, *106*, 7300–7307.

(26) Bühl, M.; Grigoleit, S.; Kabrede, H.; Mauschick, F. T. *Chem.—Eur. J.* **2006**, *12*, 477–488.

(27) Senn, H. M.; Thiel, W. *Top. Curr. Chem.* **2007**, *268*, 173–290.

(28) Kastner, J.; Thiel, S.; Senn, H. M.; Sherwood, P.; Thiel, W. *J. Chem. Theory Comput.* **2007**, *3*, 1064–1072.

(29) Geerke, D. P.; Thiel, S.; Thiel, W.; van Gunsteren, W. F. *Phys. Chem. Chem. Phys.* **2008**, *10*, 297–302.

(30) Benighaus, T.; Thiel, W. *J. Chem. Theory Comput.* **2008**, *4*, 1600–1609.

(31) Komin, S.; Gossens, C.; Tavernelli, I.; Röthlisberger, U.; Sebastiani, D. *J. Phys. Chem. B* **2007**, *111*, 5225–5232.

(32) Singh, U. C.; Kollman, P. A. *J. Comput. Chem.* **1986**, *7*, 718.

(33) Birge, R. R.; Zhang, C.-F. *J. Chem. Phys.* **1990**, *92*, 7178–7195.

(34) Assfeld, X.; Rivail, J.-L. *Chem. Phys. Lett.* **1996**, *263*, 100–106.

(35) Jacob, C. R.; Visscher, L. *J. Chem. Phys.* **2006**, *125*, No. 194104.

(36) Gao, J.; Amara, P.; Alhambra, C.; Field, M. J. *J. Phys. Chem. A* **1998**, *102*, 4714–4721.

(37) Pu, J.; Gao, J.; Truhlar, D. G. *J. Phys. Chem. A* **2004**, *108*, 632–650.

(38) Jung, J.; Choi, C. H.; Sugita, Y.; Ten-no, S. *J. Chem. Phys.* **2007**, *127*, No. 204102.

(39) Jardilliera, N.; Goursot, A. *Chem. Phys. Lett.* **2008**, *454*, 65–69.

(40) Mallik, A.; Taylor, D. E.; Runge, K.; Dufty, J. W. *Int. J. Quantum Chem.* **2004**, *100*, 1019–1025.

(41) DiLabio, G. A.; Wolkow, R. A.; Johnson, E. R. *J. Chem. Phys.* **2005**, *122*, No. 044708.

(42) DiLabio, G. A.; Hurley, M. M.; Christiansen, P. A. *J. Chem. Phys.* **2002**, *116*, 9578–9584.

(43) Xiao, C. Y.; Zhang, Y. K. *J. Chem. Phys.* **2007**, *127*, No. 124102.

(44) Poteau, R.; Ortega, I.; Alary, F.; Solis, A. R.; Barthelat, J.-C.; Daudey, J.-P. *J. Phys. Chem. A* **2001**, *105*, 198–205.

(45) Poteau, R.; Alary, F.; Makarim, H. A. E.; Heully, J.-L.; Barthelat, J.-C.; Daudey, J.-P. *J. Phys. Chem. A* **2001**, *105*, 206–214.

(46) Exner, T. E.; Mezey, P. G. *J. Comput. Chem.* **2003**, *24*, 1980–1986.

(47) Exner, T. E.; Mezey, P. G. *Phys. Chem. Chem. Phys.* **2005**, *24*, 4061–4069.

(48) Eckard, S.; Exner, T. E. *Z. Phys. Chem.* **2006**, *220*, 927–944.

(49) Komin, S.; Sebastiani, D. *J. Chem. Theory Comput.* **2009**, *5*, 1490–1498.

(50) Goedecker, S.; Teter, M.; Hutter, J. *Phys. Rev. B* **1996**, *54*, 1703.

(51) Hartwigsen, C.; Goedecker, S.; Hutter, J. *Phys. Rev. B* **1998**, *58*, 3641.

(52) Rohrig, U. F.; Sebastiani, D. *J. Phys. Chem. B* **2008**, *112*, 1267–1274.

(53) Debye, P. *Math. Ann.* **1909**, *67*, 535–558.

(54) Hestenes, M. R.; Stiefel, E. *J. Res. Natl. Bur. Stand. (U.S.)* **1952**, *49*, 409–436.

(55) Nelder, J. A.; Mead, R. *Comput. J.* **1965**, *7*, 308–313.

(56) Holland, J. H. *Adaptation in natural and artificial systems*; University of Michigan: Ann Arbor, MI, 1975.

(57) Wang, Q. H. *Biol. Cybern.* **1987**, *57*, 95–101.

(58) Yang, X. S. *Lect. Notes Comput. Sci.* **2005**, *3562*, 317–323.

(59) Karaboga, D.; Basturk, B. *J. Global Opt.* **2007**, *39*, 459–471.

(60) Karaboga, D.; Basturk, B. *Appl. Soft Comput.* **2008**, *8*, 687–697.

(61) Karaboga, D.; Akay, B. *Artif. Intell. Rev.* **2009**, *31*, 61–85.

(62) Brown, S. P.; Spiess, H. W. *Chem. Rev.* **2001**, *101*, 4125.

(63) Spiess, H. W. *Macromol. Chem. Phys.* **2003**, *204*, 340–346.

(64) Schulz-Dobrick, M.; Metzroth, T.; Spiess, H. W.; Gauss, J.; Schnell, I. *ChemPhysChem* **2005**, *6*, 315–327.

(65) Ochsenfeld, C.; Brown, S. P.; Schnell, I.; Gauss, J.; Spiess, H. W. *J. Am. Chem. Soc.* **2001**, *123*, 2597–2606.

(66) Bühl, M.; Kabrede, H.; Diss, R.; Wipff, G. *J. Am. Chem. Soc.* **2006**, *128*, 6357–6368.

(67) von Lilienfeld-Toal, A.; Tavernelli, I.; Rothlisberger, U.; Sebastiani, D. *J. Chem. Phys.* **2005**, *122*, No. 014113.

(68) Hohenberg, P.; Kohn, W. *Phys. Rev.* **1964**, *136*, B864.

(69) Kohn, W.; Sham, L. J. *Phys. Rev.* **1965**, *140*, A1133.

(70) Jones, R. O.; Gunnarsson, O. *Rev. Mod. Phys.* **1989**, *61*, 689–746.

(71) Becke, A. D. *Phys. Rev. A* **1988**, *38*, 3098.

(72) Lee, C.; Yang, W.; Parr, R. G. *Phys. Rev. B* **1988**, *37*, 785–789.

(73) Hutter, J.; Curioni, A. *ChemPhysChem* **2005**, *6*, 1788–1793.

(74) Hutter, J. et al. Computer code CPMD, version 3.12.0, Copyright IBM Corp. and MPI-FKF Stuttgart 1990−2007, http://www.cpmd.org.

(75) Putrino, A.; Sebastiani, D.; Parrinello, M. *J. Chem. Phys.* **2000**, *113*, 7102–7109.

(76) Sebastiani, D.; Parrinello, M. *J. Phys. Chem. A* **2001**, *105*, 1951.

(77) Sebastiani, D.; Goward, G.; Schnell, I.; Spiess, H. W. *J. Mol. Struct. (THEOCHEM)* **2003**, *625*, 283–288.

B.2 Specific quantum mechanical/molecular mechanical capping-potentials for biomolecular functional groups

Dieser Artikel ist in der Online-Version nicht enthalten.

Dieser Artikel ist in der Online-Version nicht enthalten.

Dieser Artikel ist in der Online-Version nicht enthalten.

Dieser Artikel ist in der Online-Version nicht enthalten.

Dieser Artikel ist in der Online-Version nicht enthalten.

Dieser Artikel ist in der Online-Version nicht enthalten.

Dieser Artikel ist in der Online-Version nicht enthalten.

B.3 Foraging on the potential energy surface: A swarm intelligence-based optimizer for molecular geometry

C. Wehmeyer, G. F. von Rudorff, S. Wolf, G. Kabbe, D. Schärf, T. D. Kühne, and D. Sebastiani:

Dieser Artikel ist in der Online-Version nicht enthalten.

Dieser Artikel ist in der Online-Version nicht enthalten.

Dieser Artikel ist in der Online-Version nicht enthalten.

Dieser Artikel ist in der Online-Version nicht enthalten.

Dieser Artikel ist in der Online-Version nicht enthalten.

Article

Water-Free Proton Conduction in Hexakis(p-Phosphonatophenyl)benzene Nanochannels

Christoph Wehmeyer,[†,‡] Manuel Schrader,[§] Denis Andrienko,[§] and Daniel Sebastiani*[,‡]

[†]Dahlem Center for Complex Quantum Systems, Freie Universität Berlin, Arnimeallee 14, 14195 Berlin, Germany
[‡]Institute of Chemistry, Martin-Luther-Universität Halle-Wittenberg, von-Danckelmann-Platz 4, 06120 Halle, Germany
[§]Max Planck Institute for Polymer Research, Ackermannweg 10, 55128 Mainz, Germany

Ⓢ Supporting Information

ABSTRACT: We elucidate the proton conduction mechanism in self-assembling stacks of phosphonic-acid-functionalized molecules (hexakis(p-phosphonatophenyl)benzene) at different temperatures (400−600 K) and at zero humidity conditions. We employ first-principles molecular dynamics simulations in combination with large-scale force-field simulations, forming a specific arrangement of the molecules in the columnar stacks. This arrangement leaves space for quasi-one-dimensional hydrogen bond nanowires along which protons are transported. We observe spontaneous autodissociation of the phosphonic acid groups, leading to proton displacements of up to 10 Å along the nanowires. Our simulations show that there is a fast (200 fs) and a slow (3−12 ps) component in the dynamics of the hydrogen bond network, corresponding to orientation fluctuations of the hydrogen bonds and persistent long-range proton transport, respectively. Our results support the hypothesis that significant proton conduction is possible in this compound at fully dehydrated conditions and at high temperatures. In such circumstances, the material may outperform the common Nafion polymer as membrane materials for proton exchange fuel cells.
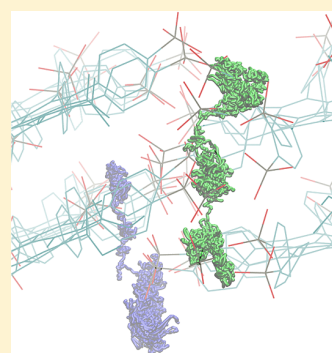
1. INTRODUCTION

Hydrogen has a potential to become an alternative energy carrier, radically changing our lifestyles and global economies.[1] As any energy carrier, hydrogen has to be produced, stored, and converted into (in this case) electrical energy. The conversion is normally performed in a hydrogen fuel cell, the core component of which is a proton exchange membrane. This membrane has to be chemically stable, durable, and proton conducting.[2] Nafion is a state-of-art material for such membranes.[3,4] Its remarkable proton conductivity relies on the formation of hydrophilic domains forming a network of water channels, where efficient proton transfer takes place, similar to pure water.[5] This, however, limits the membrane operation temperature by the boiling point of water, imposing costly requirements on catalysts and hydrogen purity.

To extend the operational temperature range, one can exchange water channels with proton-conductive liquids with a higher boiling point, e.g., imidazole derivatives,[6] or synthesize new polymeric materials with intrinsic proton conductivity,[7] for example, by using functionalized phosphonic acid groups.[8−11] The concentration of these groups should, however, be high enough to ensure efficient proton transport.[12−15] Finally, the spatial arrangement of these functional groups should form percolating pathways for protons moving through the membrane. Both issues can be addressed by using self-organizing supramolecular assemblies, such as recently proposed organic phosphonated molecules.[16−19] Some of them, such as tris(p-phosphonatophenyl)benzene (p-3 PA-HPB) and hexakis(p-phosphonatophenyl)benzene (p-6 PA-HPB, see Figure 1),

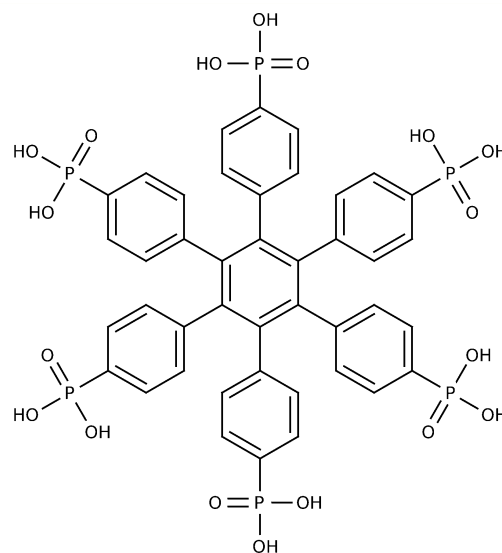

Figure 1. Molecular structure of p-6 PA-HPB.

form columnar structures with molecules stacked on top of each other (see Figure 2), as has been demonstrated by XRD measurements. While p-3 PA-HPB decomposes at 120 °C, p-6
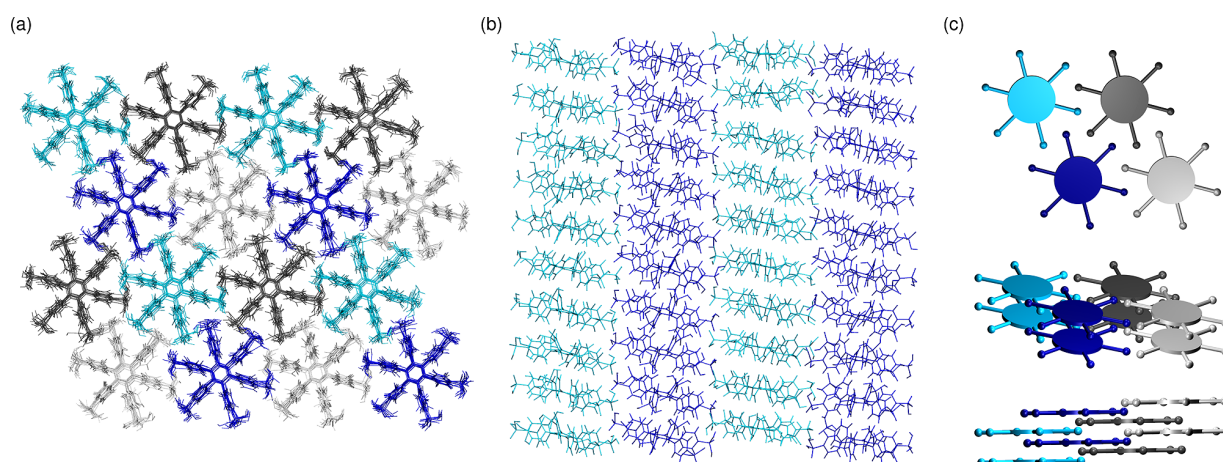
Figure 2. (a, b) Simulation snapshot of 4 × 4 columns arranged on a hexagonal lattice with ten *p*-6 PA-HPB molecules in each column. The snapshot is taken after 10 ns equilibration. (c) Schematic mutual arrangement of the *p*-6 PA-HPB molecules in the columnar stacks found after extensive equilibration of the supramolecular arrangement.

PA-HPB remains stable far beyond, and its proton conductivity exceeds that of Nafion at 160 °C; the conductivity of Nafion decreases rapidly due to loss of water in the water channels.[20−22]

In addition to the poor understanding of the microscopic mechanism of proton transfer and transport in such materials, the formulation of qualitative structure−property relations, that is, links between the chemical structure and the (macroscopic) value of proton conductivity, is a formidable task because of difficulties in characterizing experimentally and predicting theoretically their (mesoscopic) molecular ordering. In this work, we use a multiscale simulation approach in order to formulate such structure−property relations for *p*-6 PA-HPB, the chemical structure of which is shown in Figure 1.

Considerable efforts are reported in recent literature for the rational design of hydrogen-bonded molecular crystals based on this type of compound.[23] Although the vision behind this is the design of water-free proton conductors, it is established that really crystalline domains are not always optimal for proton conduction,[24,25] and that residual water molecules indeed play an important role in the conduction process.[26−29]

A complementary topic of high relevance is the determination of the impact of the pK_a value of the system[30] and its interaction with the topology of the hydrogen bond network.[31] In the case of self-assembled *p*-6 PA-HPB aggregates, the isotropic character of compounds such as Nafion is lost; instead, a preferred direction exists along the columnar stacks, in analogy to biomolecular systems such as one-dimensional ion-conducting channels in proteins.[32]

It has recently been suggested that even purely coordination-type compounds can support long-range proton transport if adequate proton acceptor/donor groups are included.[33] Similarly, suitably filled MOFs have been shown to be capable of proton conduction,[34] even under very low humidity conditions.[35]

In the present work, we investigate the structural packing motif of supramolecular assemblies of *p*-6 PA-HPB and the structural and dynamical properties of the emerging hydrogen bond network by means of classical and quantum mechanical molecular dynamics simulations. These simulations help to understand the microscopic proton conduction mechanism under dry conditions that has been measured experimentally.

2. RESULTS AND DISCUSSION

2.1. Molecular Dynamics Simulations. In order to better understand the packing motifs of *p*-6PA-HPB, we first performed classical molecular dynamics (MD) simulations of its columnar arrangement using an OPLS all-atom force-field.[36] The force-field parameters are available in the Supporting Information. The starting configuration was inspired by the interpretation of X-ray diffraction measurements:[18,19] 16 columns were arranged on a 4 × 4 hexagonal lattice, with ten *p*-6PA-HPB molecules in each column. After a 10 ns MD run in an *NPT* ensemble (T = 350 K, P = 1 atm) using the Berendsen barostat[37] and the canonical velocity rescaling thermostat,[38] the molecules in the columns rearrange as shown in Figure 2a,b.

Already a visual inspection of the hexagonal stacks indicates that the computationally observed supramolecular packing yields a highly optimized space-filling arrangement. The phosphonic acid groups are located in positions that allow a particularly high degree of intercolumnar hydrogen bonding. The stacking distance of roughly 6 Å does not, however, enable direct intracolumnar hydrogen bonding.

From an equilibrated supercell, we have devised a model of the supramolecular arrangement, which is shown in Figure 2c. The molecular stacks are arranged on a hexagonal lattice with neighboring columns shifted along the columnar axis (this increases the density of intercolumnar hydrogen bonds). Note that the conjugated cores of *p*-6 PA-HPB are slightly tilted with respect to the columnar axis. This small tilt is not accounted for in the model arrangement; that is, we assume that the columnar axes are perpendicular to the conjugated π-systems of the *p*-6 PA-HPB molecules.

We used a representative packing motif that has been extracted from the classical MD trajectory as starting point for our *ab initio* MD simulations. The latter were performed on the level of Kohn−Sham density functional theory[39−41] (DFT) using the electronic structure code CP2K[42−45] with a computational setup according to Table 1.

Our system consists of eight *p*-6 PA-HPB molecules in an orthorhombic, periodic box of volume V = 29.122 × 25.354 × 12.363 Å³. We have adopted zero humidity conditions; that is, no explicit water molecules are present in our setup. The simulations were carried out at temperatures T = 400, 500, and 600 K. Experimental evidence suggested that *p*-6 PA-HPB is chemically

Table 1. Computational Setup of the *ab Initio* Molecular Dynamics Simulations

functional	BLYP[46,47]
basis set	TZVP-GTH (GPW)[48,49]
pseudopotential	GTH[50,51]
AIMD time step	0.4 fs
dispersion correction	Grimme[52]
thermostat type	CSVR[38]
thermostat time constant	400 fs
AIMD equilibration time	10 ps
AIMD production time	30 ps

stable at intermediate temperatures, shows self-condensation of the acidic groups around 550 K, and shows decomposition of the hydrophobic core above 720 K.[18,19]

2.2. Radial Distribution Functions. We have computed radial distribution functions (RDFs) for hydrogen−oxygen and phosphorus−phosphorus at 400 K, 500 K, and 600 K; the RDFs were averaged over 30 ps each.

The RDF for hydrogen−oxygen (g_{HO}) is shown in Figure 3. The general shape is nearly identical for all temperatures. We
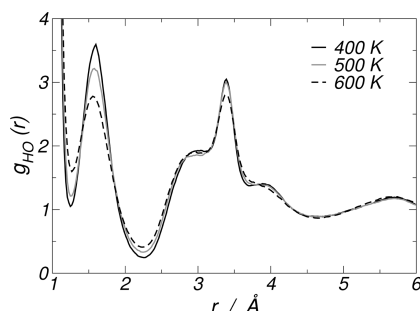
Figure 3. Radial distribution function $g_{HO}(r)$ for hydrogen−oxygen at 400 K (black/full), 500 K (gray/full), and 600 K (black/dashed).

observe that the amplitude of the hydrogen bonding peak at 1.5−1.7 Å is somewhat reduced (from 3.6 to 3.2 and 2.9) upon raising the temperature from 400 to 500 and 600 K. Further, we find an additional broad peak starting at an H−O distance of 2.9 Å, which ends in a more narrow peak between 3.2 and 3.7 Å. This peak is perfectly identical for all temperatures and has an amplitude of 3 for 400 and 500 K and a reduced amplitude of 2.9 at 600 K.

We computed the average number of oxygen atoms under the broad peak and the more narrow peak and found $n_{broad} = 7$ oxygens in the range 2.3−4.3 Å and $n_{narrow} = 2$ oxygens in the range 3.25−3.6 Å. These observations can be explained as follows: every hydrogen atom is part of one acidic group and has two more acidic groups from adjacent stacks in its close proximity, which adds up to nine oxygen atoms in this area. The hydrogen is covalently bonded to one oxygen of its own acidic group and forms a hydrogen bond with an oxygen of an adjacent acidic group; this explains why we find $n_{broad} = 7$ oxygens under the broad peak. Further, we found that the $n_{narrow} = 2$ oxygens under the narrow peak split up into one oxygen from the own acidic group of the hydrogen and one oxygen from the acidic group to which the hydrogen is connected via its hydrogen bond.

For the analysis of the structural relation between phosphorus atoms, we use a modified definition of the radial distribution function that takes into account the number of hydrogen bonds that connect the acidic groups. Figure 4a−c shows the RDFs for
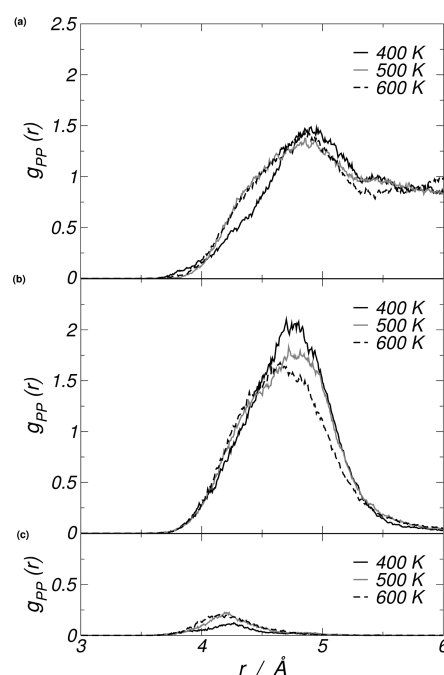
Figure 4. (a−c) Partial phosphorus−phosphorus radial distribution functions $g_{PP}(r)$ at 400 K (black/full), 500 K (gray/full), and 600 K (black/dashed) for phosphonic acids with no mutual hydrogen bond (a), those with one single hydrogen bond between them (b), and those with doubly hydrogen-bonded phosphonic acid pairs (c).

phosphorus−phosphorus at 400, 500, and 600 K. In particular in Figure 4, panel a shows the non-hydrogen-bonded contribution, panel b the single-bonded contribution, and panel c the double-bonded contribution to the total $g_{PP}(r)$. Further, we fit each curve with a single Gaussian,

$$f_g(r) = a \exp\left(-\frac{(r-\mu)^2}{2\sigma^2}\right) \tag{1}$$

to determine the amplitudes a, the centers of the peaks μ, and the standard deviations σ. With these parameters, we can compute the coordination numbers n of the individual features:

$$n = 4\pi \int_0^\infty dr \, r^2 f_g(r)\rho \tag{2}$$

where ρ is the average phosphorus density in our simulation box. The resulting parameters are shown in Table 2.

We find that each acidic group has four different groups with a distance of 4.8 ± 0.5 Å between their phosphorus atoms and shares hydrogen bonds with two of its neigbors. Occasionally,

Table 2. Centers and Standard Deviations, $\mu \pm \sigma$, of Gaussian Fits $f_g(r)$ of the $g_{PP}(r)$ According to Eq 1 and Coordination Numbers n Computed from Eq 2

	400 K	500 K	600 K
nonbonded [Å]	4.9 ± 0.4	4.8 ± 0.5	4.8 ± 0.4
single-bonded [Å]	4.7 ± 0.4	4.7 ± 0.4	4.7 ± 0.4
double-bonded [Å]	4.2 ± 0.2	4.2 ± 0.2	4.2 ± 0.2
nonbonded [1]	2.0	2.0	2.0
single-bonded [1]	2.6	2.5	2.2
double-bonded [1]	0.1	0.1	0.1
coordination [1]	4.7	4.6	4.3

two acidic groups share two hydrogen bonds, which coincides with a much shorter P−P distance of 4.2 ± 0.2 Å. The average coordination of the phosporus atoms is 4.7 at 400 K and decreases to 4.6 and 4.3 when the temperature is raised to 500 and 600 K. A frame-wise inspection of the MD trajectories yields that the hydrogen bonding occurs in 99.98% of all cases on the intermolecular level.

2.3. Hydrogen Bond Network. In order to analyze the characteristic time scales of the hydrogen bond network, we define a hydrogen bond correlation function via[27,29,53]

$$\eta_{hbn}(t) = \langle \sum_k \tilde{\delta}_{H_k^{hbn}(t+t_0), H_k^{hbn}(t_0)} \rangle_{t_0} \tag{3}$$

Here, $\tilde{\delta}_{H_k^{hbn}(t+t_0), H_k^{hbn}(t_0)} = 1$ if the acidic proton k forms at both times t and $t + t_0$ a hydrogen bond with the same pair of acceptor oxygens and 0 otherwise. To be counted as a hydrogen bond, the proton must be covalently bonded to the nearest of the oxygens ($r_{OH} < 1.3$ Å), the distance between the proton and the other oxygen must be $\tilde{r}_{OH} < 2.2$ Å, and the angle between the covalent O−H axis and the hydrogen-bonded H−O axis must be $\alpha < 60°$. Hence, the hydrogen bond correlation function $\eta_{hbn}(t)$ counts the number of hydrogen bonds at time t that have already existed at the initial time t_0. Figure 5 shows the hydrogen bond correlation function for different temperatures.
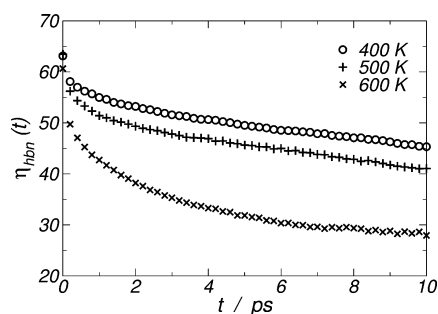

Figure 5. The hydrogen bond correlation function $\eta_{hbn}(t)$ according to eq 3 characterizes the evolution of the local hydrogen bond network.

We fit the bond correlation functions with a bimodal exponential decay and a constant term:

$$f_\eta(t) = a_0 + \sum_{i=1}^{2} a_i \, e^{-t/\tau_i} \tag{4}$$

The resulting parameters of this fit function are shown in Table 3.

We observe that the decay of the HBN is governed by two distinct time scales: the fast process on a time scale of roughly $\tau_{fast} \leq 0.3$ ps and the comparably slow process on a time scale of $\tau_{slow} \approx 3-12$ ps.

Table 3. Parameters for a Fit with Eq 4 of the Hydrogen Bond Correlation Function $\eta_{hbn}(t)$

parameter	400 K	500 K	600 K
a_2 (fast) [1]	6.5	10.5	11.9
τ_2 (fast) [ps]	0.2	0.3	0.1
a_1 (slow) [1]	15.7	20.0	21.0
τ_1 (slow) [ps]	8.5	11.7	3.0
a_0 (asymptotic) [1]	40.9	32.7	27.7

The fast process corresponds to the reversible forth-and-back switching of a hydrogen bond between two acceptor oxygens from neighboring acid groups. The slow process is caused by rotational motion of the individual phosphonic groups.

2.4. Proton Mobility. The motion of protons through the slab of p-6 PA-HPB molecules is intrinsically connected to the breaking and formation of covalent O−H bonds in the phosphonic acids. To estimate the amount of broken bonds over time, we defined a covalent bond correlation function similar to eq 3,

$$\eta_{cov}(t) = \langle \sum_k \tilde{\delta}_{H_k^{cov}(t+t_0), H_k^{cov}(t_0)} \rangle_{t_0} \tag{5}$$

where, $\tilde{\delta}_{H_k^{cov}(t+t_0), H_k^{cov}(t_0)} = 1$ if the acidic proton k is at both times covalently bonded to the same oxygen and 0 otherwise. To be counted as a covalent bonded pair, the O−H distance, r_{OH}, must be $r_{OH} < 1.3$ Å. Thus, $\eta_{cov}(t)$ is the average number of covalent O−H bonds in the original HBN (at time t_0) that are still conserved after simulation time t.

The covalent bond correlation function, $\eta_{cov}(t)$, is shown in Figure 6 (top). We observe that 5−10 O−H bonds are lost within 1 ps and that the decay reaches a plateau with a total loss of 15−30 covalent O−H bonds.
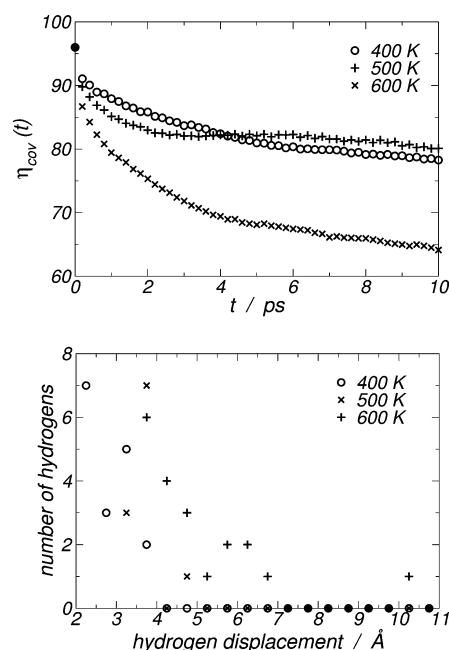

Figure 6. The covalent O−H bond correlation function, $\eta_{cov}(t)$, according to eq 5 (top) and the displacement of the acidic hydrogen atoms after $\Delta t = 30$ ps (bottom) at 400 K (●), 500 K (×), and 600 K (+).

To further gauge the mobility of the acidic protons, we computed the distribution of the total proton displacements after 30 ps, which is shown in Figure 6 (bottom). We observe that for all temperatures, most of the 96 acidic protons in the system did move less than 2 Å, which roughly corresponds to the distance of a transfer from one phosphonic acid group to one of its direct neighbors, followed by a local reorientation. In the simulation at $T = 400$ K, no proton diffuses further than 4 Å, and at $T = 500$ K, a single proton reaches a displacement of 5 Å. However, the MD simulation at $T = 600$ K yields six proton translations of about 6 Å
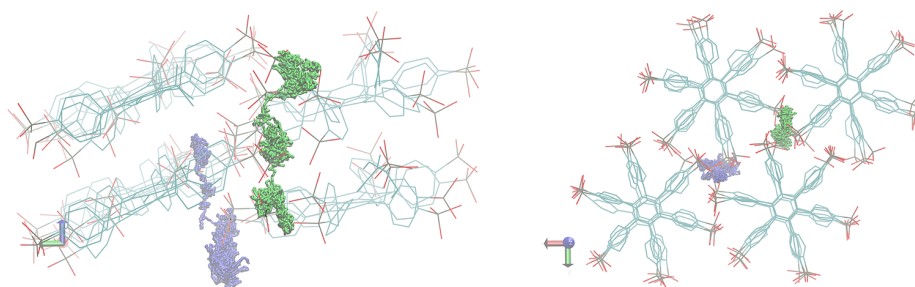
Figure 7. Pathways (green and blue) of two highly mobile protons parallel to the columnar axis. The path corresponds to a total travel time of 30 ps at 600 K. Superimposed molecular structures are taken from snapshots at 0 and 30 ps.

and one of 10 Å. While these numbers are certainly not converged in the statistical sense, they nevertheless illustrate the onset of fast long-range diffusion processes at increased temperatures.

It should be mentioned that this diffusive transport would correspond to a remarkably high current density on the order of 2 A/mm^2, roughly estimated from the average displacement of the protons that travel further than 5 Å and under the assumption that all protons move in the same direction.

We tracked the movement of those protons that autodissociate and diffuse over larger distances in the trajectory at 600 K. We observe that the protons travel within the interstice where three columns adjoin each other and that it is parallel to the columnar axis. This situation is sketched for two protons in Figure 7.

3. CONCLUSIONS

We have modeled the local packing structure of self-assembling disk-shaped hexakis(*p*-phosphonatophenyl)benzene molecules in a hexagonal pattern of supramolecular stacks in fully dehydrated conditions. The packing gives rise to a tight interstack hydrogen bond network. Our first-principles molecular dynamics simulations show that there is a specific region at the geometric centers of every triplet of stacks, which features quasi-one-dimensional proton conducting channels. Our simulations detect spontaneous autodissociation of the phosphonic acid groups, leading to a considerable charge carrier diffusion mainly parallel to the stacks. Remarkably, both the autodissociation and the proton diffusion are observed in the absence of any water molecule. This feeds hope that high-temperature low-humidity proton exchange membrane materials are getting in reach, which would significantly enhance the efficiency of the corresponding hydrogen fuel cell systems.

Our structural investigation shows that at all temperatures the typical phosphonic acid group is hydrogen-bonded to two of the four adjacent acid groups from two *different* stacks; intra-columnar hydrogen bonding was not observed. This represents clear evidence for a properly percolating hydrogen bond network in the *p*-6 PA-HPB stacks, which will support sustained long-range proton conduction.

The duration of our *ab initio* MD simulations is presently still too short to cover the time scale required for a quantitative determination of proton diffusion. Nevertheless, the trend in the maximum displacement (as reported in Figure 6, bottom) is obvious: the number of protons with displacements larger than 3 Å is seven (at $T = 400$ K), eleven (at $T = 500$ K), and more than twenty (at $T = 600$ K). In the latter case, around 20% of all acidic protons travel this far within our 30 ps simulation. This illustrates the high sensitivity of the proton mobility on temperature and confirms that compounds based on phosphonic acid groups

represent indeed a highly promising candidate for "dry" fuel cell membrane materials.

■ AUTHOR INFORMATION

Corresponding Author
*E-mail: daniel.sebastiani@chemie.uni-halle.de.
Notes
The authors declare no competing financial interest.

■ REFERENCES

(1) Crabtree, G. W.; Dresselhaus, M. S.; Buchanan, M. V. The Hydrogen Economy. *Phys. Today* **2004**, *57*, 39−44.
(2) Steele, B. C.; Heinzel, A. Materials for Fuel-Cell Technologies. *Nature* **2001**, *414*, 345−352.
(3) Paddison, S. J.; Paul, R. The Nature of Proton Transport in Fully Hydrated Nafion. *Phys. Chem. Chem. Phys.* **2002**, *4*, 1158−1163.
(4) Rozière, J.; Jones, D. J. Non-Fluorinated Polymer Materials for Proton Exchange Membrane Fuel Cells. *Annu. Rev. Mater. Res.* **2003**, *33*, 503−555.
(5) Tuckerman, M. E.; Marx, D.; Klein, M. L.; Parrinello, M. On the Quantum Nature of the Shared Proton in Hydrogen Bonds. *Science* **1997**, *275*, 817−820.
(6) Kreuer, K.-D.; Paddison, S. J.; Spohr, E.; Schuster, M. F. H. Transport in Proton Conductors for Fuel-Cell Applications: Simulations, Elementary Reactions, and Phenomenology. *Chem. Rev.* **2004**, *104*, 4637−4678.
(7) Roy, S.; Ataol, T. M.; Müller-Plathe, F. Molecular Dynamics Simulations of Heptyl Phosphonic Acid: A Potential Polymer Component for Fuel Cell Polymer Membrane. *J. Phys. Chem. B* **2008**, *112*, 7403−7409.
(8) Schuster, M.; Rager, T.; Noda, A.; Kreuer, K. D.; Maier, J. About the Choice of the Protogenic Group in PEM Separator Materials for Intermediate Temperature, Low Humidity Operation: A Critical Comparison of Sulfonic Acid, Phosphonic Acid and Imidazole Functionalized Model Compounds. *Fuel Cells* **2005**, *5*, 355−365.
(9) Joswig, J.-O.; Seifert, G. Aspects of the Proton Transfer in Liquid Phosphonic Acid. *J. Phys. Chem. B* **2009**, *113*, 8475−8480.

(10) Vilčiauskas, L.; Paddison, S. J.; Kreuer, K.-D. Ab Initio Modeling of Proton Transfer in Phosphoric Acid Clusters. *J. Phys. Chem. A* **2009**, *113*, 9193−9201.

(11) Vilčiauskas, L.; Tuckerman, M. E.; Bester, G.; Paddison, S. J.; Kreuer, K.-D. The Mechanism of Proton Conduction in Phosphoric Acid. *Nat. Chem.* **2012**, *4*, 461−466.

(12) Steininger, H.; Schuster, M.; Kreuer, K.-D.; Kaltbeitzel, A.; Bingöl, B.; Meyer, W. H.; Schauff, S.; Brunklaus, G.; Maier, J.; Spiess, H. W. Intermediate Temperature Proton Conductors for PEM Fuel Cells based on Phosphonic Acid as Protogenic Group: A Progress Report. *Phys. Chem. Chem. Phys.* **2007**, *9*, 1764−1773.

(13) Kreuer, K.-D.; Wohlfarth, A. Limits of Proton Conductivity. *Angew. Chem., Int. Ed.* **2012**, *51*, 10454−10456.

(14) Vuilleumier, R.; Borgis, D. Proton Conduction: Hopping along Hydrogen Bonds. *Nat. Chem.* **2012**, *4*, 432−433.

(15) Kobayashi, K.; Shirasaka, T.; Sato, A.; Horn, E.; Furukawa, N. Self-Assembly of a Radially Functionalized Hexagonal Molecule: Hexakis(4-hydroxyphenyl)benzene. *Angew. Chem., Int. Ed.* **1999**, *38*, 3483−3486.

(16) Jones, K. M. E.; Mahmoudkhani, A. H.; Chandler, B. D.; Shimizu, G. K. H. An Adamantane-based Tetraphosphonic Acid That Forms an Open Diamondoid Net via a Hydrogen-Bonded Phosphonic Acid-Water Cluster. *CrystEngComm* **2006**, *8*, 303−305.

(17) Beckmann, J.; Rüttinger, R.; Schwich, T. 1,3,5-Benzene-tri-p-Phenylphosphonic Acid. A New Building Block in Supramolecular Chemistry. *Cryst. Growth Des.* **2008**, *8*, 3271−3276.

(18) Jiménez-García, L.; Kaltbeitzel, A.; Pisula, W.; Gutmann, J. S.; Klapper, M.; Müllen, K. Phosphonated Hexaphenylbenzene: A Crystalline Proton Conductor. *Angew. Chem., Int. Ed.* **2009**, *48*, 9951−9953.

(19) Jiménez-García, L.; Kaltbeitzel, A.; Enkelmann, V.; Gutmann, J. S.; Klapper, M.; Müllen, K. Organic Proton-Conducting Molecules as Solid-State Separator Materials for Fuel Cell Applications. *Adv. Funct. Mater.* **2011**, *21*, 2216−2224.

(20) Ye, G.; Janzen, N.; Goward, G. R. Solid-State NMR Study of Two Classic Proton Conducting Polymers: Nafion and Sulfonated Poly-(ether ether ketone)s. *Macromolecules* **2006**, *39*, 3283−3290.

(21) Ye, G.; Hayden, C. A.; Goward, G. R. Proton Dynamics of Nafion and Nafion/SiO$_2$ Composites by Solid State NMR and Pulse Field Gradient NMR. *Macromolecules* **2007**, *40*, 1529−1537.

(22) Yu, T. H.; Sha, Y.; Liu, W.-G.; Merinov, B. V.; Shirvanian, P.; Goddard, W. A., III Mechanism for Degradation of Nafion in PEM Fuel Cells from Quantum Mechanics Calculations. *J. Am. Chem. Soc.* **2011**, *133*, 19857−19863.

(23) Maly, K. E.; Gagnon, E.; Maris, T.; Wuest, J. D. Engineering Hydrogen-Bonded Molecular Crystals built from Derivatives of Hexaphenylbenzene and Related Compounds. *J. Am. Chem. Soc.* **2007**, *129*, 4306−4322.

(24) Lee, Y. J.; Bingöl, B.; Murakhtina, T.; Sebastiani, D.; Meyer, W. H.; Wegner, G.; Spiess, H. W. High Resolution Solid State NMR Studies of Poly(Vinyl Phosphonicic Acid) Proton Conducting Polymer: Molecular Structure and Proton Dynamics. *J. Phys. Chem. B* **2007**, *111*, 9711−9721.

(25) Lee, Y. J.; Murakhtina, T.; Sebastiani, D.; Spiess, H. W. ^{2}H Solid State NMR of Mobile Protons: It is not always the Simple Way. *J. Am. Chem. Soc.* **2007**, *129*, 12406−12407.

(26) Siwick, B. J.; Bakker, H. J. On the Role of Water in Intermolecular Proton-Transfer Reactions. *J. Am. Chem. Soc.* **2007**, *129*, 13412−13420.

(27) Ludueña, G. A.; Kühne, T. D.; Sebastiani, D. Mixed Grotthuss and Vehicle Transport Mechanism in Proton Conducting Polymers from ab Initio Molecular Dynamics Simulations. *Chem. Mater.* **2011**, *23*, 1424−1429.

(28) Vilčiauskas, L.; Kreuer, K.-D. Comment on "Mixed Grotthuss and Vehicle Transport Mechanism in Proton Conducting Polymers from Ab initio Molecular Dynamics Simulations". *Chem. Mater.* **2011**, *23*, 3377−3378.

(29) Ludueña, G. A.; Kühne, T. D.; Sebastiani, D. Reply to Comment on "Mixed Grotthuss and Vehicle Transport Mechanism in Proton Conducting Polymers from Ab initio Molecular Dynamics Simulations". *Chem. Mater.* **2011**, *23*, 3379−3380.

(30) Shokri, A.; Abedin, A.; Fattahi, A.; Kass, S. R. Effect of Hydrogen Bonds on pK$_a$ Values: Importance of Networking. *J. Am. Chem. Soc.* **2012**, *134*, 10646−10650.

(31) Shokri, A.; Schmidt, J.; Wang, X.-B.; Kass, S. R. Hydrogen Bonded Arrays: The Power of Multiple Hydrogen Bonds. *J. Am. Chem. Soc.* **2012**, *134*, 2094−2099.

(32) Hu, F.; Schmidt-Rohr, K.; Hong, M. NMR Detection of pH-Dependent Histidine−Water Proton Exchange Reveals the Conduction Mechanism of a Transmembrane Proton Channel. *J. Am. Chem. Soc.* **2012**, *134*, 3703−3713.

(33) Umeyama, D.; Horike, S.; Inukai, M.; Itakura, T.; Kitagawa, S. Inherent Proton Conduction in a 2D Coordination Framework. *J. Am. Chem. Soc.* **2012**, *134*, 12780−12785.

(34) Pardo, E.; Train, C.; Gontard, G.; Boubekeur, K.; Fabelo, O.; Liu, H.; Dkhil, B.; Lloret, F.; Nakagawa, K.; Tokoro, H.; Ohkoshi, S.-i.; Verdaguer, M. High Proton Conduction in a Chiral Ferromagnetic Metal-Organic Quartz-like Framework. *J. Am. Chem. Soc.* **2011**, *133*, 15328−15331.

(35) Sadakiyo, M.; Okawa, H.; Shigematsu, A.; Ohba, M.; Yamada, T.; Kitagawa, H. Promotion of Low-Humidity Proton Conduction by Controlling Hydrophilicity in Layered Metal-Organic Frameworks. *J. Am. Chem. Soc.* **2012**, *134*, 5472−5475.

(36) Jorgensen, W. L.; Tirado-Rives, J. The OPLS [Optimized Potentials for Liquid Simulations] Potential Functions for Proteins, Energy Minimizations for Crystals of Cyclic Peptides and Crambin. *J. Am. Chem. Soc.* **1988**, *110*, 1657−1666.

(37) Berendsen, H. J. C.; Postma, J. P. M.; van Gunsteren, W. F.; DiNola, A.; Haak, J. R. Molecular Dynamics with Coupling to an External Bath. *J. Chem. Phys.* **1984**, *81*, 3684−3690.

(38) Bussi, G.; Donadio, D.; Parrinello, M. Canonical Sampling through Velocity Rescaling. *J. Chem. Phys.* **2007**, *126*, 014101.

(39) Hohenberg, P.; Kohn, W. Inhomogeneous Electron Gas. *Phys. Rev.* **1964**, *136*, B864−B871.

(40) Kohn, W.; Sham, L. J. Self-Consistent Equations Including Exchange and Correlation Effects. *Phys. Rev.* **1965**, *140*, A1133−A1138.

(41) Jones, R. O.; Gunnarsson, O. The Density Functional Formalism, Its Applications and Prospects. *Rev. Mod. Phys.* **1989**, *61*, 689−746.

(42) VandeVondele, J.; Hutter, J. An Efficient Orbital Transformation Method for Electronic Structure Calculations. *J. Chem. Phys.* **2003**, *118*, 4365−4369.

(43) Kolafa, J. Time-Reversible Always Stable Predictor-Corrector Method for Molecular Dynamics of Polarizable Molecules. *J. Comput. Chem.* **2004**, *25*, 335−342.

(44) Krack, M. Pseudopotentials for H to Kr Optimized for Gradient-Corrected Exchange-Correlation Functionals. *Theor. Chem. Acc.* **2005**, *114*, 145−152.

(45) VandeVondele, J.; Krack, M.; Mohamed, F.; Parrinello, M.; Chassaing, T.; Hutter, J. QUICKSTEP: Fast and Accurate Density Functional Calculations using a Mixed Gaussian and Plane Waves Approach. *Comput. Phys. Commun.* **2005**, *167*, 103−128.

(46) Becke, A. D. Density-Functional Exchange-Energy Approximation with Correct Asymptotic Behavior. *Phys. Rev. A* **1988**, *38*, 3098−3100.

(47) Lee, C.; Yang, W.; Parr, R. G. Development of the Colle-Salvetti Correlation-Energy Formula into a Functional of the Electron Density. *Phys. Rev. B* **1988**, *37*, 785−789.

(48) Lippert, G.; Hutter, J.; Parrinello, M. A Hybrid Gaussian and PlaneWave Density Functional Scheme. *Mol. Phys.* **1997**, *92*, 477−487.

(49) VandeVondele, J.; Hutter, J. Gaussian Basis Sets for Accurate Calculations on Molecular Systems in Gas and Condensed Phases. *J. Chem. Phys.* **2007**, *127*, 114105.

(50) Hartwigsen, C.; Goedecker, S.; Hutter, J. Relativistic Separable Dual-Space Gaussian Pseudopotentials from H to Rn. *Phys. Rev. B* **1998**, *58*, 3641−3662.

(51) Goedecker, S.; Teter, M.; Hutter, J. Separable Dual-Space Gaussian Pseudopotentials. *Phys. Rev. B* **1996**, *54*, 1703−1710.

(52) Grimme, S. Semiempirical GGA-type Density Functional constructed with a Long-Range Dispersion Correction. *J. Comput. Chem.* **2006**, *27*, 1787−1799.

Article

(53) Schiffmann, C.; Sebastiani, D. Hydrogen Bond Networks: Structure and Dynamics via First-Principles Spectroscopy. *Phys. Status Solidi B* **2012**, *249*, 368−375.

C Academic curriculum vitae

Der Lebenslauf ist in der Online-Version aus
Gründen des Datenschutzes nicht enthalten.

D Acknowledgements

The creation of this thesis and my work during the last years were supported by many people, and I want to express my gratitude to those who aided in making this time a great experience:

- Prof. D. Sebastiani for cordially accommodating me in his group and for being a great advisor in the truest sense.

- Prof. P. Brouwer for his willingness to review this thesis and for his guidance during its final stage.

- B. Dabisch and A. Pasanec for their patient administrative support.

- All my collaborators inside and outside of Berlin, in particular, A. Ihrig, S. Wolf, G. Kabbe, G. F. von Rudorff, D. Schärf, Jun.-Prof. T. D. Kühne, M. Schrader, and Dr. D. Andrienko; and of course all my colleagues from the Sebastiani group.

- My friends O. Leidinger and J. Reinecke for valuable comments on this work.

- My wife Wera for reading the whole thing several times and rigorously pointing out my bad grammar, and for her patience and support.